The hydrodynamics of two-dimensional oscillating flows over ripples: the effects of asymmetries in ripple shape and currents

by

Subasha Wickramarachchi

A thesis
presented to the University of Waterloo
in fulfillment of the
thesis requirement for the degree of
Doctor of Philosophy
in
Applied Mathematics

Waterloo, Ontario, Canada, 2017

Examining Committee Membership

The following served on the Examining Committee for this thesis. The decision of the Examining Committee is by majority vote.

External Examiner	Oliver B. Fringer
	Associate Professor
Supervisor	Kevin Lamb
	Professor
Internal Member	Marek Stastna
	Professor
Internal Member	Francis Poulin
	Associate Professor
Internal-external Member	Andrea Scott
	Assistant Professor

I hereby declare that I am the sole author of this thesis. This is a true copy of the thesis, including any required final revisions, as accepted by my examiners.

I understand that my thesis may be made electronically available to the public.

Abstract

The research presented in this thesis involved consideration of three increasingly asymmetric oscillatory flows over two ripple profiles, one of which is asymmetric and represents a small deviation from a symmetric ripple. The asymmetric flow forcings are chosen so as to have an identical excursion distance. For each of these cases, the vorticity, velocity, and shear stress fields are analyzed for the first 40 cycles. The Reynolds number is mostly limited to 1250, with a few cases also run at $Re = 5000$.

During the first three cycles, it can be observed that two vortices of opposite vorticity are generated during each cycle, one each during the forward and backward flows. These vortices pair up and trace a path that extends higher up as the asymmetry of the flow or ripple shape is amplified. This effect is a consequence of the increasing difference between the vorticities of the individual vortices in each vortex pair. After about three periods, the motion becomes more and more chaotic due to the interaction of the newly generated vortices with the older ones.

During the quasi-steady state, which occurs after about 25 cycles, the vortices generated remain close to the ripple and dissipate before reaching much higher for all cases except the all-symmetric case. For the asymmetric ripple and the asymmetric forcings, a consistent negative mean flow can be observed, which tends to attain a near-steady speed after about 35 cycles. During the quasi-steady state, vortex interactions with the ripple contribute a substantial amount of momentum flux to the system, as do the strong shear layers that can be seen to form at a short distance on either side of the ripple crest. The newly generated vortex pairs exhibit initial trajectories in the direction of the mean flow and are found to trace the transfer of momentum from near the ripple to area of mean current.

Acknowledgements

Table of Contents

List of Tables

List of Figures

Chapter 1

Introduction

Nature offers abundant examples of flows over ripple-like profiles, such as sand dunes and ripples in deserts, coastal areas, and rivers. Some of these structures, especially those formed on rocks and similar hard, solid materials, are created by fluid flows of wind or water that occur over many years. Those formed on sand-like materials that are granular, cohesive or non-cohesive, appear much more quickly. In laboratory experiments involving granular non-cohesive sediments (sand), equilibrium ripples corresponding to a given oscillatory flow forcings are found to form within 100 to 600 cycles (Doucette & O'Donoghue, 2006). Dunes can develop over several months due to unidirectional winds over sand that is granular and non-cohesive. They are formed by the wind-forced movement of the sand and by avalanching down the lee side due to the angle of repose associated with sand. Their typical shape is marked by a less steep side plus a steeper lee side, whose slope has an angle close to that of the angle of repose. The unidirectional flow causes the dunes to move in the direction of the wind.

Ripple-like bedforms can be created by purely unidirectional, purely oscillatory, or combined flows. In nature, the scales (ripple length and height) associated with ripples and flow forcings (Reynolds number and asymmetry) vary widely. From a classification perspective, dunes have longer length scales than ripples.

Ripples in nature are not often found to be geometrically symmetric due to the non-symmetric character of fluid flows. Symmetric ripples are formed by symmetric oscillatory currents, but non-symmetric ripples can be formed in many ways: by unidirectional currents, by non-symmetric oscillatory currents, and by a combination of oscillatory and unidirectional currents. The vast majority of ripples found in nature are three dimensional. The parameters that contribute to the formation of ripples are not limited to fluid

flow alone, but can also depend on other factors, including the properties of the sediments (cohesiveness, granularity, granule density, and the microscopic geometry of the granules, etc.), the sediment uptake created by the flow, and the sediment settlement resulting from the flow (Nielsen, 1981). Sediments trapped and transported by currents may travel great distances. Ripples found in nature migrate and change shape over time.

As a prelude to the presentation of the study conducted for this thesis, a simple specific example of a ripple formed in a wave tank can be considered. This example is typical of a vast number of wave tank experiments that have been performed in order to examine the formation of ripples. Two other methodologies are U-tube and "RippleKart" experiments for investigating the formation of ripples created by oscillatory flows (Admiraal et al. , 2006; Hay et al. , 2012). In U-tube experiments, however, some features, such as Stoke's drift associated with free surface progressive waves, cannot be replicated. In the simulations for the work presented in this thesis, the flow forcings are similar to those found in U-tube experiments, since oscillatory forcings are applied in a strictly horizontal direction. This simplified flow devoid of Stoke's drift is useful in investigating various streaming mechanisms in isolation. In reality, studies indicate that waveshape-related streaming modifies Stoke's drift, even reversing its direction as the relative water depth, kh, where k is the wavenumber associated with the free surface wave and h is the water depth, decreases (Kranenburg et al. , 2012).

Testik et al. (2006) conducted a wave-tank experiment using fine sand with mean grain diameter $D_{50} = 0.04$ cm and a wave orbital diameter $d \approx 40$ cm. The actual experimental wave-tank setup up is illustrated in Figure 1.1 (a). Waves are generated from sinusoidal oscillations created by a paddle, generating symmetric waves that propagate toward a sloping beach, becoming increasingly non-symmetric and eventually breaking as they approach the beach. The water depth near the paddle is approximately 1.0m. Phase-averaged velocities measured at a number of locations (sections) remote from the paddle are shown in Figure 1.1(b). The progressive wave, which is initially sinusoidal, can be observed to have become asymmetric at position 19 and still more asymmetric nearer the beach at position 27. The ripples formed close to these sections have stable shapes and the profile shown in Figure 1.1 (d). Over a time scale much longer than that of the flow oscillations, these ripples migrate in the direction of shoaling waves. In general, for two-dimensional ripples formed by fine sand ($\frac{d_{0,1/3}}{D_{50}} < 2000$, orbital ripples), as shown in Figure 1.1(d) by the best-fit line (green) to data points, experimental evidence indicates that $\lambda \approx 0.76 d_{0,1/3}$, where λ is the wavelength of the ripple and $d_{0,1/3}$ is the wave orbital diameter of the forcing based on the significant wave height, i.e., the mean wave height of the highest third of the waves (O'Donoghue & Clubb, 2001; Traykovski et al. , 1999; Wiberg & Harris, 1994). In this thesis, consideration is focused on the special case of fixed
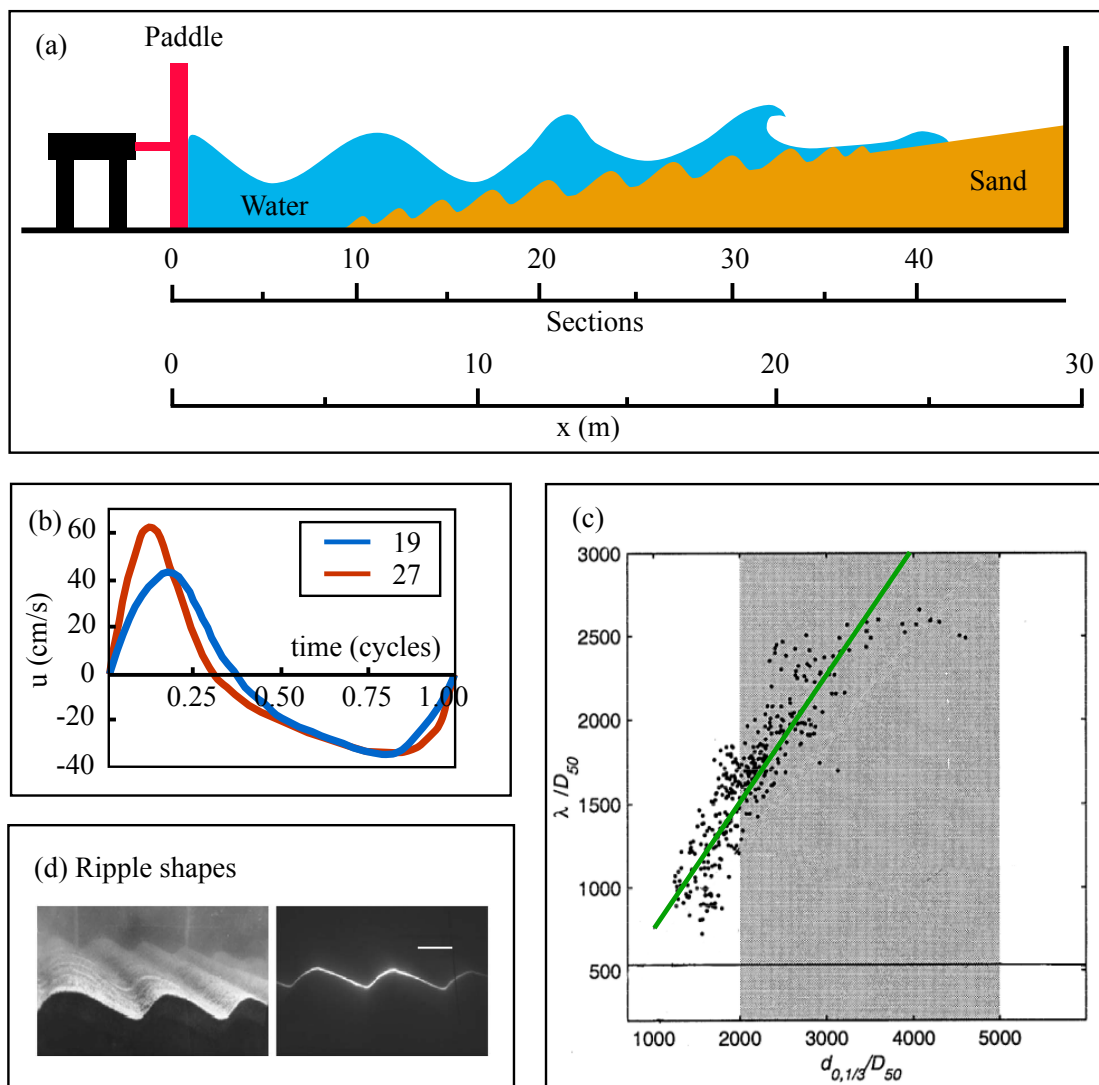
Figure 1.1: (a) Schematic setup of a typical wave tank, (b) velocity measured under shoaling waves, (c) ripples formed due to shoaling waves, and (d) relationship between wave orbital diameter and the ripple length (Testik *et al.*, 2006; Traykovski *et al.*, 1999).

3

two-dimensional symmetric and asymmetric ripples and the application of flow forcings whose shape resembles the oscillatory flows observed, for example, at positions 19 and 27. However, the Reynolds numbers used are much smaller than that associated with this wave-tank experiment.

Numerical studies of flow dynamics over ripple-like bed forms have been conducted for many decades. A semi-analytical approach was used by Longuet-Higgins (1981), who used conformal transformations to study two-dimensional (2D) sinusoidal flow over steep symmetric ripples that exhibit a corner at the crest. The drag coefficient determined in this study was in remarkable agreement with those established experimentally, and it was shown that a vortex pair is shed from the ripple crest during each half cycle. Blondeaux & Vittori (1991) studied the initial formation of vortices over 2D symmetric smooth ripples that result from sinusoidal flows at low Reynold numbers. They first used an orthogonal transformation to transform the ripple to a line in order to obtain a rectangular domain and then solved a system of equations comprised of the discrete Fourier-transformed (horizontal direction) vorticity equation expressed in terms of the stream function. The height of the rectangular domain was essentially limited to two-thirds of the ripple length. Their work confirmed some of the results obtained by Longuet-Higgins (1981) and led to further observations: (1) a vortex structure generated as a result of boundary layer separation at the ripple crest pairs up with a secondary vortex structure generated by the rolling up of the free shear layer at the ripple surface on the lee side of the ripple, and the resulting vortex pair moves away from the ripple bottom; (2) within a single cycle, the flow separation at the ripple crest creates two or more vortex structures that develop independently of each other; (3) older vortex structures may sometimes coalesce with the newly generated vortex structures. Scandura *et al.* (2000) carried out numerical experiments similar to those conducted by Blondeaux & Vittori (1991) but in three dimensions and with observations of flow characteristics after 10 cycles. For $Re = 2000$, it was observed that the basic 2D flow structures become wavy with respect to transverse perturbations as they leave the ripple crest. More recently, Blondeaux *et al.* (2004) utilized the same numerical method reported by Scandura *et al.* (2000) in order to study three-dimensional (3D) vorticity dynamics in sinusoidal flows over a symmetric rippled bed. The Reynolds numbers and ripple steepness values used were similar to those employed by Blondeaux & Vittori (1991). The flow characteristics were observed at the 15th cycle, at which point the flow attains a degree of quasi-periodicity. It was observed that flow dynamics are characterized by the presence of coherent ribs superimposed on the larger spanwise vortices generated at the ripple crest. Barr *et al.* (2004) investigated turbulent oscillatory flows over 3D symmetric sand ripples.

The effect of ripple steepness and asymmetry on the vortices generated by Stokes third-order waves was studied by Kim *et al.* (1994) in 2D using a numerical method that incorporated a turbulence closure model. Only one flow forcing period was considered. The numerical method involved the use of finite difference schemes to solve for velocity and pressure from the continuity and Reynolds-averaged momentum equations. The flow Reynolds number considered was approximately $Re = 27\,700$, and it was concluded that the impact of changes in ripple asymmetry with respect to vortex dynamics is negligible. The authors also observed that ripple steepness has consistent visible effects on vorticity dynamics.

A number of other direct numerical simulation (DNS) investigations of flow over symmetric ripples have been conducted (Angelis *et al.* , 1997; Cherukat *et al.* , 1998); however, computationally less intensive methods such as large-eddy simulation (LES) have been more widely chosen for the examination of flow over ripples. Grigoriadis *et al.* (2012) used LES to study the wave turbulent boundary layer over rippled beds in order to investigate oscillatory-unidirectional flow (wave-plus-current) over symmetric ripples with a corner at the crest. They found that these flows are dominated by the oscillatory part of the flow and the ripple height. The effect of the currents considered was found to be relatively weak with respect to the flow patterns over the ripple. Coherent structures in steady 3D flows over 2D dunes, including asymmetric dunes, were studied by Chang & Constantinescu (2013) using LES for the case of channel flow. Their investigation was focused on the primary mechanisms through which large-scale hairpin vortices form and on how these mechanisms change between two dune geometries (sinusoidal versus asymmetric dunes). In terms of both height and length, the asymmetric dunes considered in this work were about twice the size of the symmetric ripples.

Numerical experiments have seldom focused on the investigation of flow dynamics over asymmetric ripples. The work presented in this thesis is an investigation of the changes in the flow dynamics that occur as the flow forcing and ripple shape deviate slightly from their initial symmetric profiles. Details of the symmetric ripple and flow forcing have been taken from Blondeaux & Vittori (1991). The asymmetric forcings we have used are excursion-length-preserving flow forcings adapted from Malarkey & Davies (2012), and the asymmetric ripples are the area-preserving asymmetric deviations from the ripple shape used by Blondeaux & Vittori (1991). The excursion length of the water particles associated with an oscillatory flow determines the natural length of the ripples formed: the ripple length is generally about four-thirds of the horizontal excursion length of the water particles and is independent of the Reynolds number and the density of the sand comprising the ripple (Longuet-Higgins, 1981; O'Donoghue & Clubb, 2001). The asymmetric ripple shapes found in nature are often also associated with the presence of

steady background currents (Dumas *et al.* , 2005; Sekiguchi & Yokokawa, 2008; Testik *et al.* , 2006). For this reason, we have also explored the effects that a weak background current may have on vortex generation.

The maximum Reynolds number considered in this work, $Re = 1250$, is much lower than the Reynolds numbers typically associated with flow over ripples in physical experiments. Admiraal *et al.* (2006) utilized a U-tube along with Reynolds numbers ranging from approximately 13 000 to 47 000 to investigate vortex dynamics for sinusoidal flows over self-formed ripples. For their study of asymmetric sand-ripple profiles formed under nonlinear shoaling waves in a wavetank, Testik *et al.* (2006) used flow forcings with an associated Reynolds number of approximately 60 000. Given the numerical model used in our study (SPINS) and its current parallelization limitations (scaling) for handling mapped grids, achieving convergence at high Reynolds numbers such as $Re = 60\,000$ is computationally infeasible.

This thesis is organized as follows. The governing equations, model setup, numerical model, and validations are given in Chapter 2. Chapter 3 provides a look at the initial evolution of the vortices associated with two different ripple shapes and three flow forcings. An analysis of the vorticity and the flow fields at the quasi-steady state is presented in Chapter 4.

Chapter 2

Governing equations, numerical model, and boundary layers

In this chapter, we give the governing equations, the numerical model, some validation results, and basic concepts related to oscillatory boundary layers.

2.1 Governing equations

The governing equations are the 2D incompressible Navier-Stokes equations

$$\mathbf{u}^*_{\mathbf{t}^*} + \mathbf{u}^* \cdot \nabla^* \mathbf{u}^* \; = \; -\frac{\nabla^* \mathbf{P}^*}{\rho^*} + \gamma^* \nabla^{*2} \mathbf{u}^* + \mathbf{F}^*_{\mathbf{b}}, \tag{2.1}$$

$$\nabla^* \cdot \mathbf{u}^* \; = \; 0, \tag{2.2}$$

where $\mathbf{u} = (u, w)$, u is the horizontal velocity, w is the vertical velocity, P is the pressure, ρ is the density, γ is the kinematic dynamic viscosity, $\mathbf{F_b}$ is the body force per unit mass, and $*$ indicates dimensional quantities. Periodic boundary conditions are used in the x-direction, and no-slip boundary conditions are imposed at the top (flat, rigid-lid) and bottom (ripple-shaped) boundaries.

For the purpose of non-dimensionalization, we use the following scales (Blondeaux & Vittori, 1991; Blondeaux $et\ al.$, 2004; Scandura $et\ al.$, 2000):

$$t^* = \tfrac{t}{\omega^*}, \quad (u^*, w^*) = s^* \omega^* (u, w), \quad (x^*, z^*) = s^* (x, z), \tag{2.3}$$

where $\omega^* = \frac{2\pi}{T^*}$, T^* is the oscillation period, and s^* is the excursion length of the oscillatory forcing, all of which have the same value for all forcings. The excursion length is half the distance moved by a particle during each period of rightward or leftward flow in the absence of any steady background currents. The non-dimensional governing equations are given by

$$\mathbf{u_t} + \mathbf{u} \cdot \nabla \mathbf{u} = -\nabla \mathbf{P} + \frac{1}{\mathbf{Re}} \nabla^2 \mathbf{u} + \mathbf{F_b}, \tag{2.4}$$

$$\nabla \cdot \mathbf{u} = 0, \tag{2.5}$$

where the Reynolds number is

$$Re = \frac{\omega^* s^{*2}}{\gamma^*}. \tag{2.6}$$

The velocity field is enforced using the body force $\mathbf{F_b} = (G(t), 0)$, where $G(t)$ is the time-derivative of the desired far field flow. For the simulations, we considered a bottom boundary in the form of a single smooth ripple with height h^* and length l^*. Other non-dimensional parameters include the ripple height $h = \frac{h^*}{s^*}$, the ripple length $l = \frac{l^*}{s^*}$, and the water depth $H = \frac{H^*}{s^*}$.

There is an alternate Reynolds number often used in similar previous studies, where the length scale is taken as $\delta^* = \sqrt{\frac{2\gamma^*}{\omega^*}}$, the boundary layer thickness, which is briefly discussed in Section 2.2. With this length scale, the governing equations become

$$\frac{1}{Re_\delta} \mathbf{u_t} + \mathbf{u} \cdot \nabla \mathbf{u} = -\nabla P + \frac{1}{Re_\delta} \nabla^2 \mathbf{u} + \mathbf{F_b}, \tag{2.7}$$

$$\nabla \cdot \mathbf{u} = 0, \tag{2.8}$$

where the Reynolds number is

$$Re_\delta = \frac{\omega^* s^* \delta^*}{\gamma^*}. \tag{2.9}$$

The two Reynolds numbers Re and Re_δ are related by

$$Re_\delta = \sqrt{2Re}, \tag{2.10}$$

Unless otherwise explicitly mentioned, for the rest of the thesis, all quantities are non-dimensionalized using the scales given in (2.3).

2.2 Boundary layers

In the previous section, one of the Reynolds numbers introduced, Re_δ, was based on the boundary layer thickness associated with oscillatory flows. Here we give some theoretical background regarding the oscillatory boundary layer associated with oscillatory flow near a fixed infinite plate (Svendsen, 1990). In its simplest form, the wave boundary layer is given by Stokes' second problem and the boundary layer thickness is associated with $\delta = \sqrt{\dfrac{2}{Re}}$ (or $\delta^* = \sqrt{\dfrac{2\gamma^*}{\omega^*}}$ in dimensional quantities).

Suppose there is a semi-infinite column of a viscous incompressible fluid undergoing horizontal oscillations above a stationary horizontal boundary and that the oscillations are sinusoidal. Assuming laminar flow, the governing equations (2.4) simplifies to

$$\frac{\partial u(z,t)}{\partial t} = \frac{1}{Re} \frac{\partial^2 u(z,t)}{\partial z^2} \tag{2.11}$$

The boundary conditions are

$$u(z,t) = \cos(t) \text{ as } z \to \infty \tag{2.12}$$
$$u(0,t) = 0 \tag{2.13}$$

The solution to (2.11-2.13) is given by

$$u(z,t) = \cos(t) - e^{-\frac{z}{\delta}} \cos\left(t - \frac{z}{\delta}\right) \tag{2.14}$$

where $\delta = \sqrt{\frac{2}{Re}}$. Figure 2.1 shows how the phase difference between the boundary layer and the far field vary at different times in a cycle. The flow field in the boundary layer is always ahead of that in the far field, but this phase shift effect decays exponentially away from the boundary.
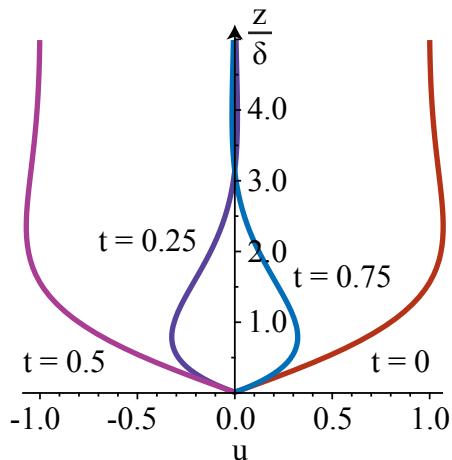
Figure 2.1: The variation of the phase shift of the flow field near the boundary relative to the outer flow field at $t = 0$ (red), $t = 0.25$ (purple), $t = 0.5$ (mulberry), and $t = 0.75$ (blue) cycles.

2.3   Numerical method

For our simulations, we employed SPINS, which is a pseudo-spectral solver for use with incompressible Navier-Stokes equations in two and three dimensions. It is written in C++ and was developed by Subich *et al.* (2003).

SPINS maps the domain to a flat-bottomed domain where the transformed equations are solved. Fourier discretization is used in the horizontal and Chebyshev in the vertical. SPINS uses a mixed explicit-implicit time-stepping scheme: advection and forcing are treated explicitly, and diffusion implicitly. Explicit terms are handled with a third-order Adams-Bashforth method, and a Richardson extrapolation is used for generating the additional information required at initiation. This process gives a globally third-order method in time. Because currently the top and bottom boundary conditions must be either both no-slip or both free-slip, in our simulations, a no-slip boundary condition is applied on the upper boundary.

In SPINS, continuous functions are approximated spatially on a discrete set of grid points, and spectral collocation methods are used for approximating derivatives. The build-up of energy at high wavenumbers is controlled by exponentially filtering out energy at all wavenumbers greater than two-thirds of the Nyquist frequency (low pass filter).

Parallelization is achieved using MPI. For our simulations, 16 cores were typically used, and the run time for one period was about 3 to 4 hours. All simulations were run in a cluster consisting of 2.7GHz 8-core Intel Xeon processors and the optimal run time was obtained (for this setup using mapped grids) when the 16 cores used were constrained to one node, where each node consists of two 8-core processors. The SPINS output includes the velocities, pressure, and the vorticity.

2.4   Model setup and validation

For this work, we first validated the results obtained using SPINS against those obtained by Blondeaux & Vittori (1991). Table 2.1 lists the Reynolds numbers used by Blondeaux *et al.* (2004), Blondeaux & Vittori (1991), Scandura *et al.* (2000), and in our simulations. $Re = 1250$ was used for validating the results obtained using SPINS. A number of simulations were then conducted involving asymmetric flow forcings over asymmetric ripples.

Table 2.1: Comparison of Reynolds numbers, h/l, and s/l used in Blondeaux & Vittori (1991), Scandura *et al.* (2000), Blondeaux *et al.* (2004), and the simulations for the current study.

Reference	Re	h/l	s/l
Blondeaux & Vittori (1991)	1250, 5000	0.15, 0.20	0.75, 1.5
Scandura *et al.* (2000)	875, 1005, 1250, 2000	0.076, 0.12, 0.14, 0.15	0.75
Blondeaux *et al.* (2004)	1250, 1600	0.125, 0.15	0.75
Our simulations	1250, 5000	0.15	0.75

2.4.1   Oscillatory (sinusoidal) flow over symmetric ripples

The first step was to use SPINS to replicate the results obtained by Blondeaux & Vittori (1991) for symmetric ripples and forcing. A schematic of the numerical simulation setup is shown in Figure 2.2, in which H is the depth at the ripple trough, l is the wavelength of the ripple, and h is the trough-to-crest height of the ripple. The bottom ripple is defined

by $z = F(x)$, where z and x are represented parametrically as

$$x\left(\xi\right) = \xi - \frac{h}{2}\sin\left(k\xi\right),\tag{2.15}$$

$$z\left(\xi\right) = \frac{h}{2}\left[1 + \cos\left(k\xi\right)\right] - H,\tag{2.16}$$

where $k = \frac{2\pi}{l}$, and the dummy variable $\xi \in [0, l]$. This defines a ripple profile with a crest narrower than the trough, with a crest to trough ratio 0.35:0.65, approximately. This non-linear expression can be used directly in SPINS in order to define the ripple surface, provided that non-uniform grid spacings are used in the x-axis. However, the use of non-uniform grid spacings sometimes causes spurious oscillations. For this reason, we employed an iterative method for generating uniform grid spacing. The details of the iterative scheme are given in Appendix A.

To obtain the horizontal flow field $u(t) = \sin(t)$, we set

$$G(t) = \cos(t)\tag{2.17}$$
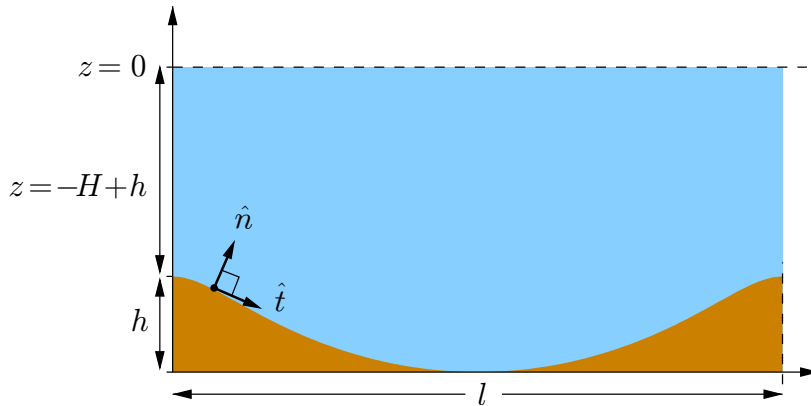
Figure 2.2: Schematic of the symmetric ripple shape used in the simulation.

Figure 2.3 shows comparative composite images of the results obtained using SPINS and those obtained by Blondeaux & Vittori (1991). The areas in red (SPINS) or the thick black lines (Blondeaux & Vittori, 1991) represent clockwise vorticity, and the areas in blue (SPINS) or the thin black lines (Blondeaux & Vittori, 1991) indicate counterclockwise vorticity. It is evident that the results produced using SPINS closely resemble those obtained

12

by Blondeaux & Vittori (1991) for $Re = 1250$. Figure 2.4 shows a similar comparison at later times. The two results show some significant differences, especially for the clockwise vorticity. We can observe that the two results have deviated somewhat, especially after 1 cycle. Figures 2.5 and 2.6 show similar results, but at higher Reynolds number, $Re = 5000$. It can be observed that the vortex structures are very similar, especially when $s/l = 1.5$.

For the domain $\left[0, \frac{4}{3}\right] \times \left[0, \frac{2}{3}\right]$, Blondeaux & Vittori (1991) reported that 128×128 grid points (uniform) was sufficient for convergence up to $Re = 5000$. The same domain cannot be used in SPINS due to the effects of the no-slip top boundary condition, which alters flow dynamics at $z = \frac{2}{3}$, unless the boundary is much further up. For this reason, in SPINS, we used a larger domain size: $\left[0, \frac{4}{3}\right] \times [0, 3.2]$, with 256×512 grid points. As explained in section 3.1.2, this number of grid points provides sufficient convergence for the strongest current C4 over three oscillatory cycles. Because a Chebyshev grid is used in the vertical, the resolution near the bottom boundary is much higher than in the center of the water column.

In the next chapter, we will also look at the bottom shear stress. We give here some convergence results for the bottom shear stress. The shear stress acting on the surface of the ripple. The bottom shear stress is given by (Barr *et al.* , 2004)

$$\tau \;=\; \frac{1}{Re}\frac{\partial}{\partial \boldsymbol{n}}\left(\boldsymbol{u} \cdot \boldsymbol{t}\right) \;=\; \frac{1}{Re}\boldsymbol{\nabla}\left(\boldsymbol{u} \cdot \boldsymbol{t}\right) \cdot \boldsymbol{n}. \tag{2.18}$$

Using (2.15)-(2.16), $\boldsymbol{t} = \left(\frac{\partial x}{\partial \xi}, \frac{\partial z}{\partial \xi}\right)$, $\boldsymbol{n} = \left(-\frac{\partial z}{\partial \xi}, \frac{\partial x}{\partial \xi}\right)$, $\hat{\boldsymbol{t}} = \frac{\boldsymbol{t}}{\|\boldsymbol{t}\|}$, and $\hat{\boldsymbol{n}} = \frac{\boldsymbol{n}}{\|\boldsymbol{n}\|}$, we can evaluate this expression.

We replicate bottom shear stress results reported in Blondeaux & Vittori (1991) and details of how this is done using SPINS can be found in the Appendix B. Figures 2.7-2.8 are composite images comparing the shear stress obtained by SPINS with those reported in Blondeaux & Vittori (1991). For $Re = 1250$, there is good agreement for the shear stresses. For $Re = 5000$, there is good agreement until $t = \pi$. There are deviations for longer times, most likely due to the slightly different vorticity as visible in Figure 2.5.
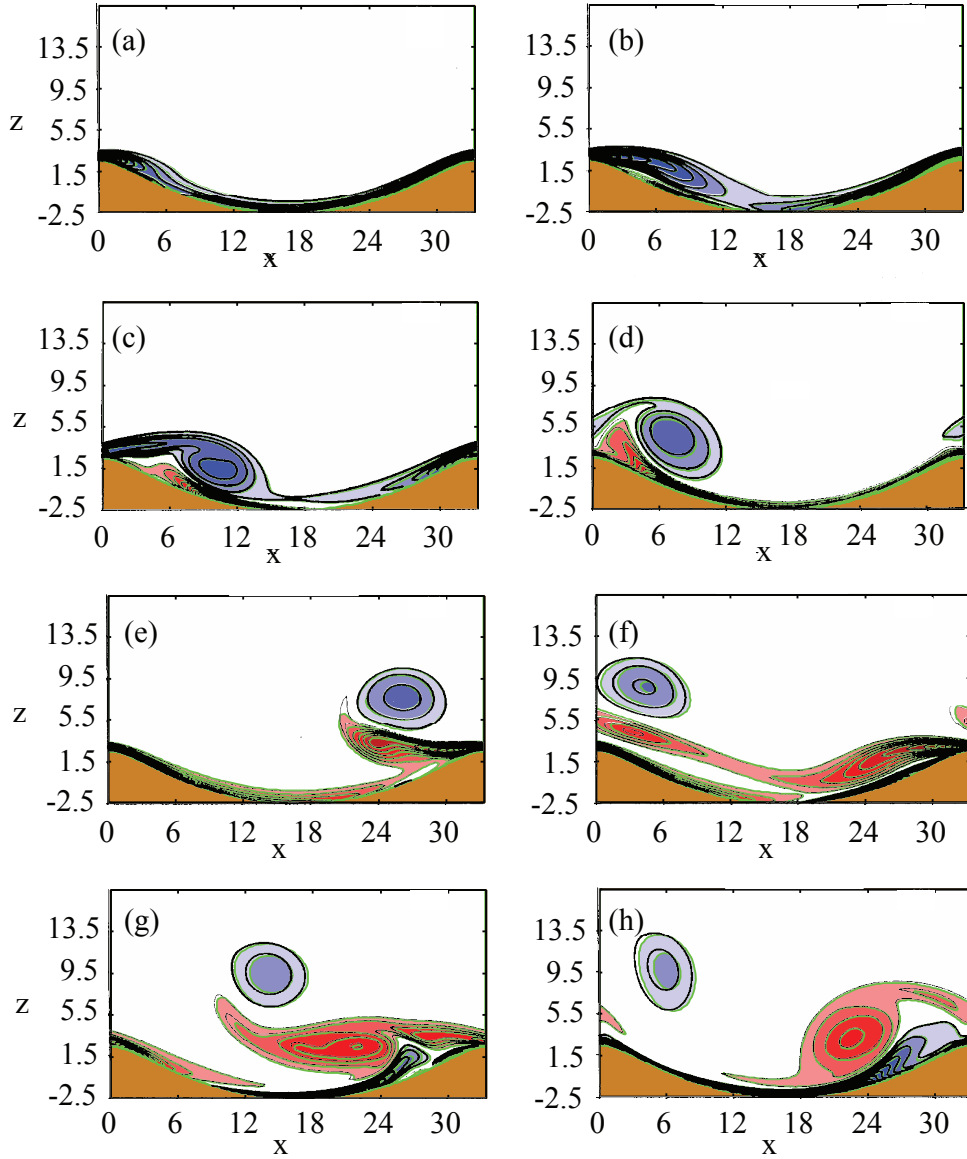
Figure 2.3: Figure 6 from Blondeaux & Vittori (1991). The black contours are from Blondeaux & Vittori (1991) and those in color are from our simulation. Vorticity contours $\Delta\omega = 0.15$, $Re = 1250$, $h/l = 0.15$, $s/l = 0.75$. Time (cycles) values: (a) $t = 0.125$, (b) $t = 0.25$, (c) $t = 0.375$, (d) $t = 0.5$, (e) $t = 0.625$, (f) $t = 0.75$, (g) $t = 0.875$, (h) $t = 1$. In Blondeaux & Vittori (1991), lengths are non-dimensionalized using the length scale $\delta^* = \sqrt{\frac{\gamma^* T^*}{\pi}}$.
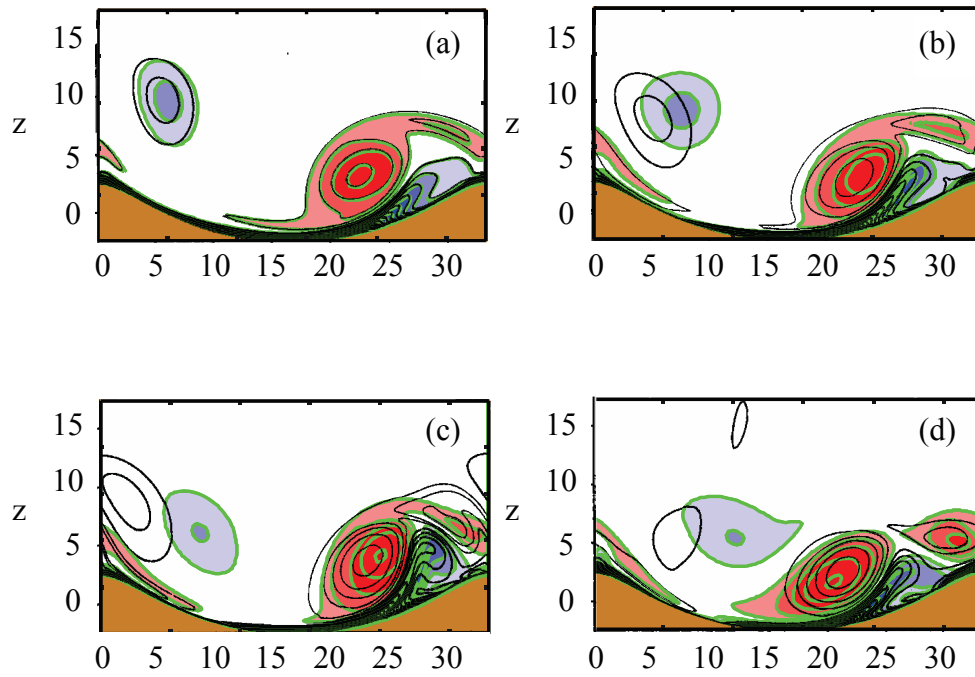
Figure 2.4: Reproduction of Figure 18 in Blondeaux & Vittori (1991). Vorticity contours $\Delta\omega = 0.15$. $Re = 1250$, $h/l = 0.15$, $s/l = 0.75$, (a) $t = 1$; (b) $t = 2$; (c) $t = 3$; (d) $t = 5$ cycles.
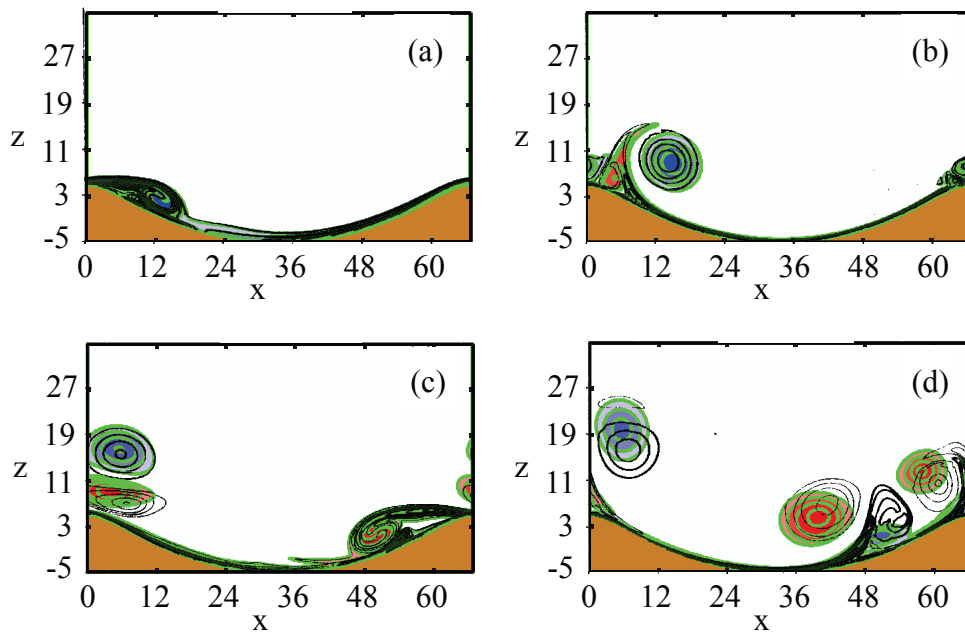
Figure 2.5: Reproduction of Figure 7 in Blondeaux & Vittori (1991). Vorticity contours $\Delta\omega = 0.15$. $Re = 5000$, $h/l = 0.15$, $s/l = 0.75$, (a) $t = 0.25$; (b) $t = 0.5$; (c) $t = 0.75$; (d) $t = 1$ cycles.
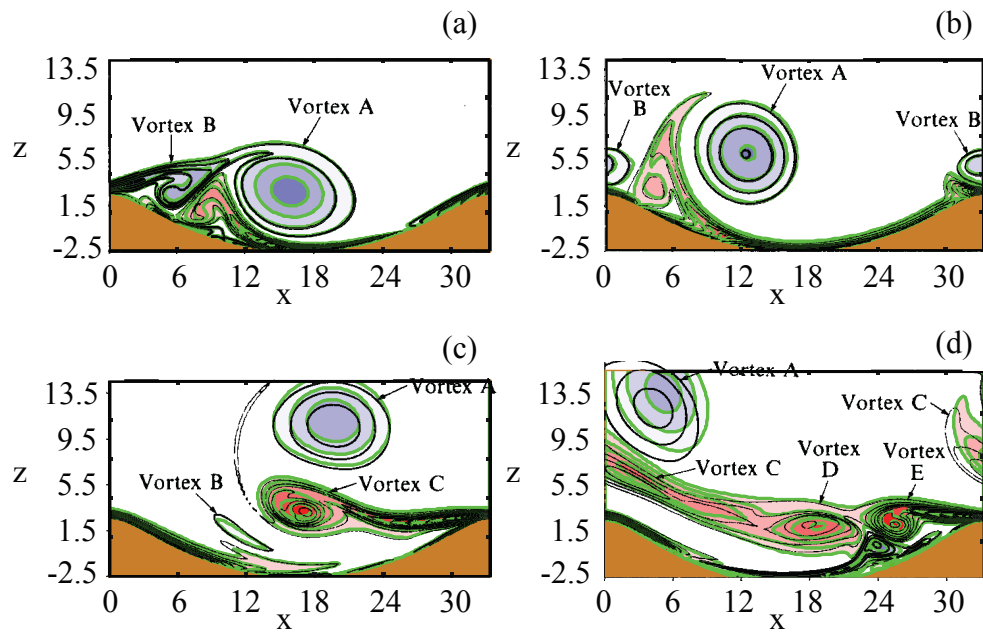
Figure 2.6: Reproduction of Figure 15 in Blondeaux & Vittori (1991). Vorticity contours $\Delta\omega = 0.15$. $Re = 5000$, $h/l = 0.15$, $s/l = 1.5$, (a) $t = 0.375$; (b) $t = 0.5$; (c) $t = 0.625$; (d) $t = 0.75$ cycles.
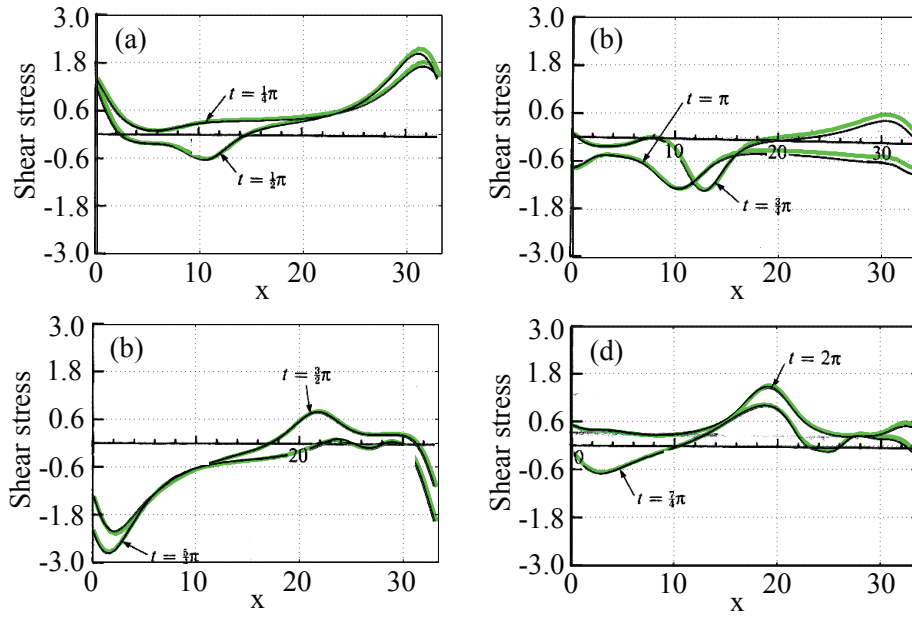
Figure 2.7: Reproduction of Figure 21 in Blondeaux & Vittori (1991): Bed shear stress time development for parameters $Re = 1250$, $h/l = 0.15$, and $s/l = 0.75$. (a) $t = 0.125$ and $t = 0.25$; (b) $t = 0.375$ and $t = 0.5$; (c) $t = 0.625$ and $t = 0.75$; and (d) $t = 0.875$ and $t = 1$ cycles. The green curve indicates the bottom shear stress obtained using SPINS, black curve represents the bottom stress obtained in Blondeaux & Vittori (1991).
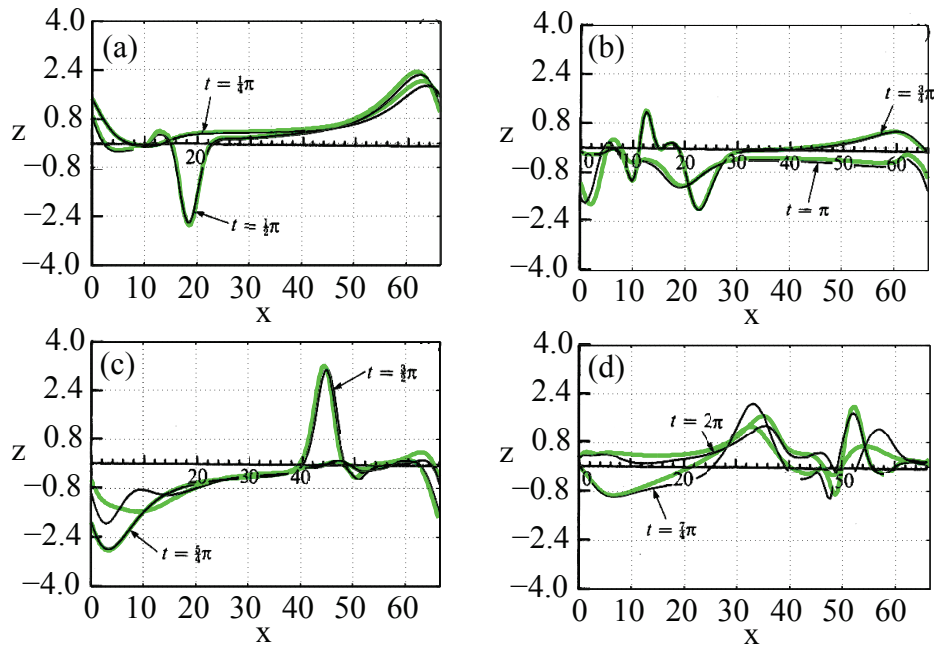
Figure 2.8: Reproduction of Figure 22 in Blondeaux & Vittori (1991): Bed shear stress time development for parameters $Re = 5000$, $h/l = 0.15$, and $s/l = 0.75$. (a) $t = 0.125$ and $t = 0.25$; (b) $t = 0.375$ and $t = 0.5$; (c) $t = 0.625$ and $t = 0.75$; and (d) $t = 0.875$ and $t = 1$ cycles. The green curve indicates the bottom shear stress obtained using SPINS, black curve represents the bottom stress obtained in Blondeaux & Vittori (1991).

Chapter 3

Two dimensional vortices generated by oscillatory flow over ripples: early stages

In the previous chapter, vortex dynamics associated with symmetric oscillatory flow over a symmetric ripple was presented. In this chapter, this is extended to encompass some oscillatory asymmetric flows over an asymmetric ripple in combination with the symmetric cases. Further, the flow behavior when the flow forcing have a passive background current on top of the active oscillatory forcing is also investigated. This chapter organized as follows: first the asymmetric flow forcings and the ripple shape is defined, followed numerical convergence results, simulations results, and discussions. For flows with $Re = 1250$, vortex paths, their strengths, and velocity profiles during the early stages are analyzed. The chapter concludes with a brief look at vortex structures for flows with $Re = 5000$.

3.1 Asymmetric oscillatory flow over asymmetric ripples

Flows over ripple beds occur frequently in nature, most notably at beaches. Sinusoidal flows over symmetric ripples, however, are uncommon. Ripples found at beaches, for example, are asymmetric in shape, and fluid flows over them are often asymmetric as well (Dumas *et al.* , 2005; Sekiguchi & Yokokawa, 2008; Testik *et al.* , 2006). This section describe the simulations we carried out in order to examine symmetric (sinusoidal) flow forcings at $Re = 1250$ as well as increasingly asymmetric flow forcings with the same excursion length. Our investigation also included consideration of a ripple profile that deviates (asymmetrically) from those used by Blondeaux & Vittori (1991).

3.1.1 Ripple shapes and flow forcings

Our asymmetric currents, defined by equation (3.1), follow the form specified by Malarkey & Davies (2012), who developed a model based on the velocity profiles observed under asymmetric waves during physical experiments:

$$u(t) = \alpha \left[(1 - b^2) \frac{\sin(t + \psi) - b\sin(\phi)}{1 + b^2 - 2b\cos(t + \psi - \phi)} \right], \tag{3.1}$$

where α is the amplitude parameter, ψ is a phase shift parameter, ϕ is a waveform parameter, and b is the asymmetry parameter. All of our asymmetric currents have a maximum rightward current that is stronger than the maximum leftward current. The ratio $\frac{s}{l}$ for all of the asymmetric velocity profiles used was

$$\frac{s}{l} = \frac{1}{2l} \int_0^{t'} u(t)dt = -\frac{1}{2l} \int_{t'}^{2\pi} u(t)dt = \frac{1}{l} = 0.75, \tag{3.2}$$

where t' is the intra-wave time at which $u(t)$ reverses direction; l is the ripple length; and s is the excursion distance, which has a non-dimensional value of 1. Maintaining the ratio $\frac{s}{l}$ ensures that all wave forcings result in the same excursion, an important consideration since the excursion determines the length of the ripples formed by the oscillatory flows (Traykovski *et al.* , 1999).

Flow asymmetry is characterized by velocity skewness (velocity asymmetry) and acceleration skewness (acceleration asymmetry) (Kranenburg *et al.* , 2012). Velocity skewness

Table 3.1: Parameters used for defining flow forcings C1, C2, and C4 along with their flow characteristics (accurate to 2 decimal places). A is the asymmetry defined by (3.3), $u_{\max} = \max\limits_{t\in[0,T]} |u(t)|$. For the flow reversal times, n represent the period number and takes values $0, 1, 2, ...$

Label	Parameter values				Flow characteristics					
	α	b	ψ	ϕ	A	$A1$	$B1$	$u_{\max}$	Re	Flow reversal times
C1	1	0	0	0	1.00	0.50	0.50	1.00	$1250, 5000$	$nT, (n+0.5)T$
C2	1.05	0.25	0.18	$\pi/4$	2.04	0.59	0.64	1.24	$1250, 5000$	$nT, (n+0.44)T$
C4	1.14	0.40	0.35	$\pi/3$	4.24	0.67	0.62	1.55	$1250, 5000$	$nT, (n+0.39)T$

can be measured in a number of ways, including

$$A = \left(\frac{\max_{t\in[0,2\pi]} u(t)}{\min_{t\in[0,2\pi]} u(t)}\right)^2 \tag{3.3}$$

and

$$A1 = \frac{\max_{t\in[0,2\pi]} u(t)}{\max_{t\in[0,2\pi]} u(t) + \left|\min_{t\in[0,2\pi]} u(t)\right|} \tag{3.4}$$

According to these definitions, a flow is considered symmetric in terms of its velocity profile (no velocity skewness), if $A = 1$ or $A1 = 0.5$. In analogy to (3.4), acceleration skewness can be defined using

$$B1 = \frac{\max_{t\in[0,2\pi]} \dot{u}(t)}{\max_{t\in[0,2\pi]} \dot{u}(t) + \left|\min_{t\in[0,2\pi]} \dot{u}(t)\right|} \tag{3.5}$$

where $\dot{u}(t) = \frac{du(t)}{dt}$. Accordingly, the acceleration of a flow is considered symmetric (no acceleration skewness) if $B1 = 0.5$.

To investigate the changes in vortex dynamics as the flow forcing becomes increasingly asymmetric, we made use of the flow forcings C1 ($A = 1.0$, symmetric), C2 ($A = 2.04$), and C4 ($A = 4.24$). Table 3.1 lists the parameters used for defining these flow forcings as well as some of the characteristics of the flows. The flow forcings are depicted in Figure 3.1.
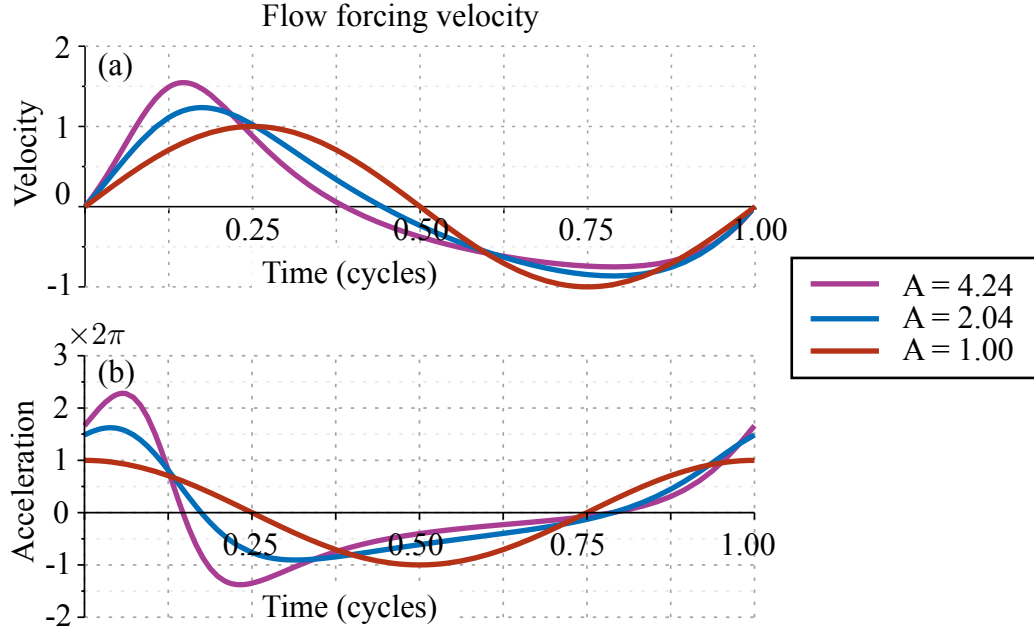
Figure 3.1: Flow forcings used in the numerical experiments. (a) Velocity profile for C1 ($A = 1.0$), C2 ($A = 2.04$), and C4 ($A = 4.24$); and (b) their corresponding accelerations.

To investigate the changes in hydrodynamics that occur when the ripple shape is slightly asymmetric, we defined an asymmetric ripple profile in which the ripple shapes are expressed parametrically based on

$$x(\xi) = \xi - \frac{h}{2}\sin(k\xi) - \frac{\epsilon}{2}[1 - \cos(k\xi)], \tag{3.6}$$

$$z(\xi) = \frac{h}{2}[1 + \cos(k\xi)] - H, \tag{3.7}$$

where $k = \frac{2\pi}{l}$, $\xi \in [0, l]$, and ϵ is the parameter used to control the asymmetry of the ripple shape. The ripple shapes R0 and R1, shown in Figure 3.2, are defined using the choices $\epsilon = 0.0$ and 0.1, respectively. R0 is the symmetric ripple that matches the shape used by Blondeaux et al. (1991, 2004). For the ripple shapes defined by (3.6)-(3.7), the ripple area is independent of ϵ:

$$\int_0^l z(\xi)\, x'(\xi)\, d\xi = -Hl - \frac{\pi h^2}{4} + \frac{hl}{2}.$$

This step eliminates any contribution to the strength of the vortices due to the effects related to fluid-volume. For the ripple shapes we employed, $\frac{h}{l}$ and ϵ are small, and we used a simple iterative scheme as a means of generating a uniform grid. The details of the iterative scheme are given in Appendix A.
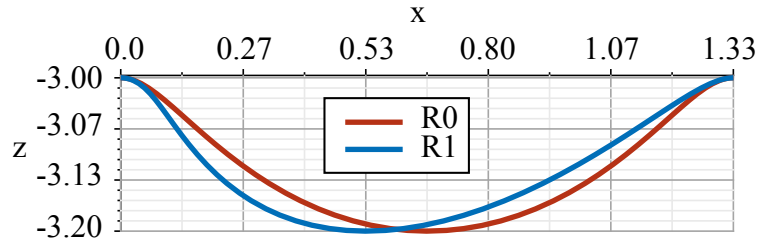
Figure 3.2: Bottom profiles R0 ($\epsilon = 0$) and R1 ($\epsilon = 0.1$) used in the numerical experiment. R0 is the symmetric ripple.

This section introduced two ripple shapes, R0 and R1, and three flow forcings, C1, C2, and C4. The combinations of these ripple shapes and flow forcings comprise six cases that are referred to as "the six base cases", labeled Rm-Cn, $n = 1, 2, 4$ and $m = 0, 1$.

3.1.2 Convergence

For the most asymmetric case, which used C4 current and R1 ripple shape, convergence was considered and was checked with respect to four aspects: vortex trajectory, vortex strength, enstrophy, and mean horizontal velocity averaged over a single period.

Figure 3.3 shows the convergence of the near-wall horizontal velocity profile at times of strongest far-field (forcing) velocity in the 5th and 6th cycles. Profiles obtained using 128×256 (blue), 256×512 (red), and 512×1024 (black) grids are shown. At the lower boundary, the velocity is measured above the ripple crest. It can be observed that there is sufficient convergence for the two highest grid sizes, at least until the sixth period. Also, the boundary layer thickness is thinner by a factor of about two at the lower boundary, reaching about $\frac{z}{\delta} = 0.5$ above the ripple crest. In the simulations conducted in this thesis, a 256×512 grid is used and the number of grid points within the boundary layer, $0 < \left| \frac{z}{\delta} \right| < 0.5$, is about 26.

To quantify the strength of a vortex, the vorticity was integrated about a neighborhood containing the center of the vortex (defined as the point where the vorticity has maximum
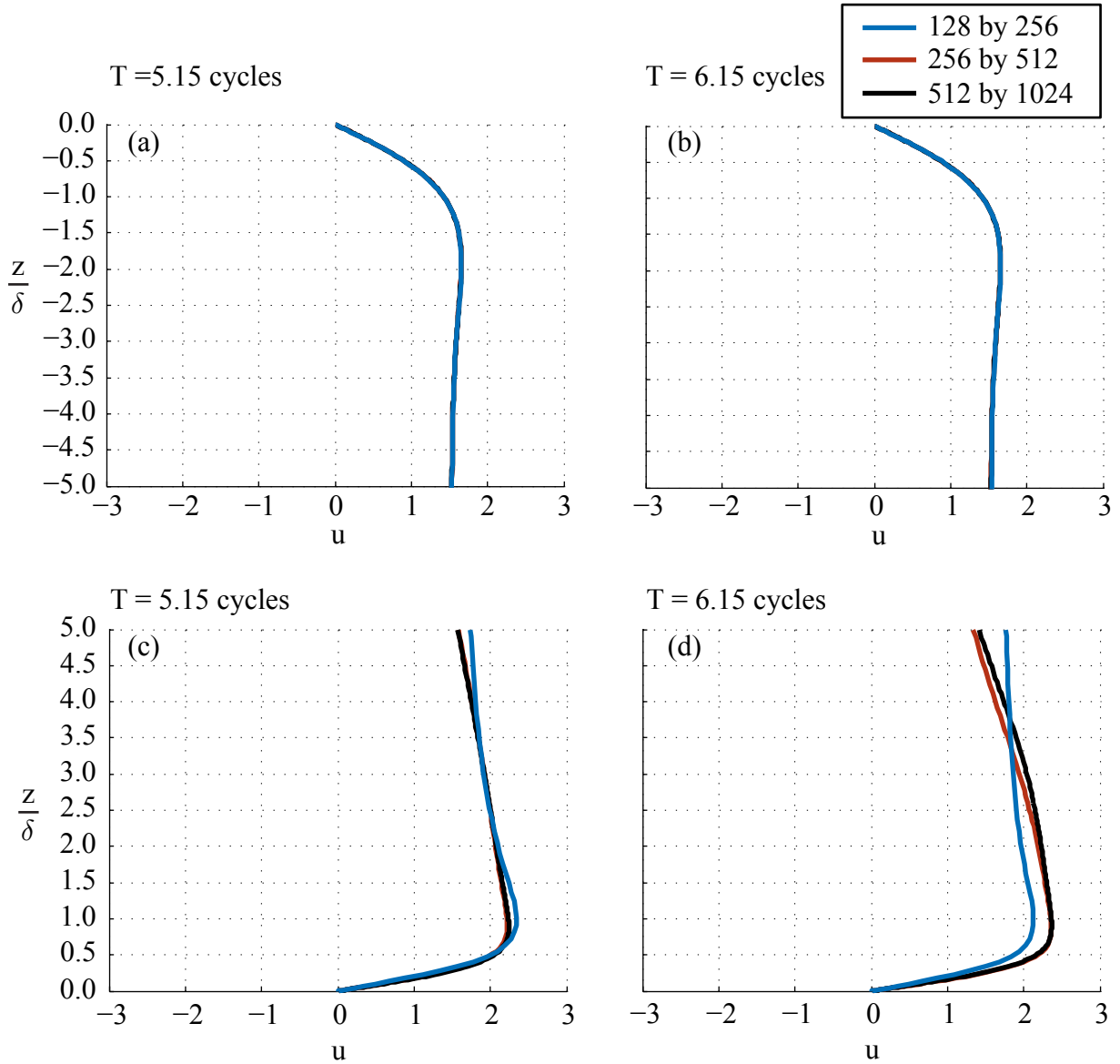
Figure 3.3: Instantaneous horizontal near-wall top and bottom velocity (u) for the case R1-C4 at $Re = 1250$ and 128×256 (blue), 256×512 (red), and 512×1024 (black) grids. The profiles shown are the near-wall velocity at the (a) top boundary at 5.15 cycles, (b) top boundary at 6.15 cycles, (c) bottom boundary at 5.15 cycles, and (d) bottom boundary at 6.15 cycles. The bottom near-wall velocity is measured at the ripple crest. $\delta = \sqrt{\frac{2\gamma}{\omega}}$ is the Stokes boundary layer thickness. In (a) and (b), the three curves overlap each other. In (c), the black and the red curves overlap.

magnitude). This neighborhood is defined as the region where the vorticity is greater than a cut-off 3.75, determined based on the work reported by Blondeaux & Vittori (1991). The value 3.75 demarcates near circular or elliptical neighborhoods around vortex centers. Figure 3.4 shows typical neighborhoods around vortex centers: the $+$ and $\times$ signs indicate the vortex centers, and the neighborhood boundary is indicated by the green contour. In the Figure, the x-range $\left[0, \frac{4}{3}\right]$ of the domain has been given a periodic extension in order to illustrate how the areas are traced when the vortices cross the periodic boundary.
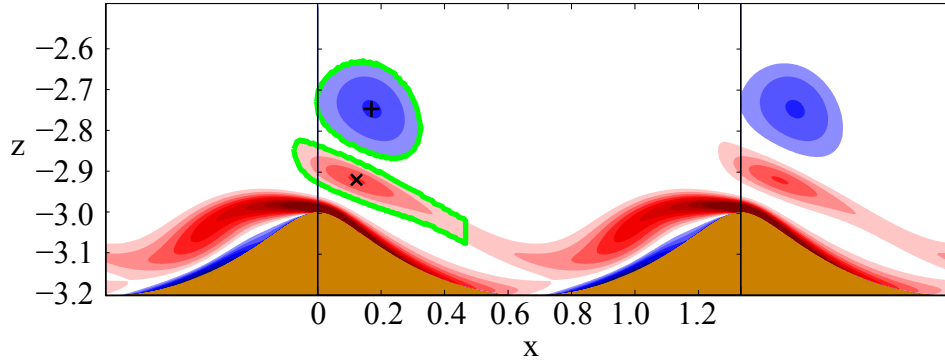
Figure 3.4: Illustration of the area considered for the calculation of the strength of the vortices. Clockwise (counterclockwise) vorticity is indicated by blue (red) colors. Vorticity contours $\Delta\omega = 3.75$, and the green contours indicate the neighborhood boundary at which $|\omega| = 3.75$. For each vortex, we consider the area bounded by the green contour for the calculation of its vorticity strength.

The enstrophy is defined as $\frac{1}{2}\int_S \omega^2 dx dz$, where ω is the vorticity and S is the domain defined by the area bounded by $x = 0$, $x = l$, $z = 0$, and by the bottom ripple profile. Figure 3.5 shows the enstrophy for the R1-C4 case obtained for three different resolutions: mulberry solid, red dashed, blue dotted curves represent 128×256, 256×512, and 512×1024 resolutions, respectively. It can be observed that, with respect to enstrophy, convergence is sufficient for both 256×512 and 512×1024 at least up to the third cycle. However, due to the high degree of shear near the top and bottom boundaries, enstrophy is dominated by vorticity near the boundaries and may not be a good indicator of convergence for the relatively much weaker vorticity in the interior of the domain.

Figure 3.6 shows the convergence of the vortex paths with increasing resolution for the vortices of the vortex pair formed at the first, third, and fifth flow reversals. The dotted and the dashed curves for the two highest resolutions largely overlap. Sufficient
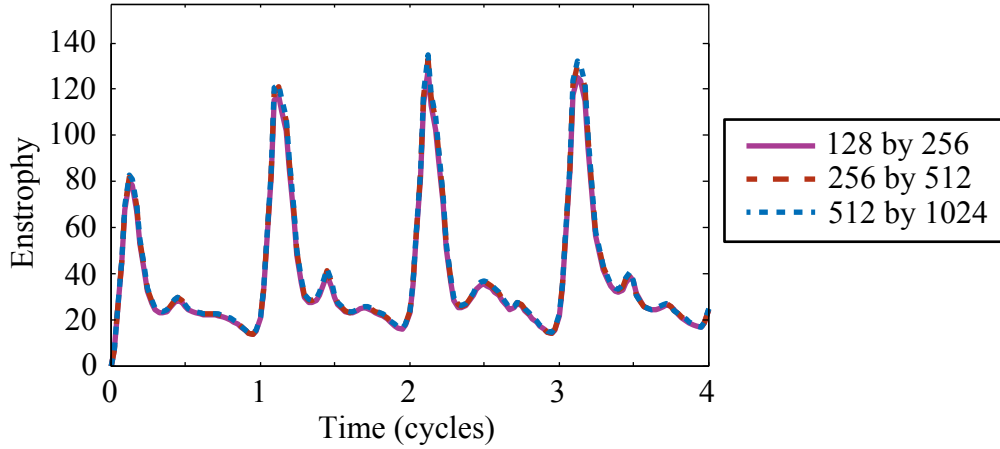
Figure 3.5: Convergence of enstrophy for the R1-C4 case at grid sizes 128×256, 256×512, and 512×1024. All three curves overlap each other.

convergence can be observed for the highest two resolutions, at least until the end of the second cycle.

Figure 3.7(a) illustrates how the strength of a vortex varies with increasing resolution. It should also be noted that, for the two highest resolutions, the rates of decay of the vortex strengths are nearly identical: averaged in time, approximately 0.6 per cycle, provided there are no vortex interactions. Figure 3.7(b) shows the convergence of the mean horizontal current during the third cycle. Both figures reveal that convergence is sufficient with 256×512 grids.

Figure 3.8 indicates the vorticity field after 2.5 cycles for the C4 flow forcing and the R1 ripple shape. The presence of many vortex structures can be seen, and not just the vortices generated during this cycle. As the number of cycles increases, so does the number of vortices, and the vortex interactions also become more frequent. This effect makes the evolution of the flow field more and more chaotic, and as a consequence, the simulations at different resolutions diverge over time.

We used 256×512 for our simulations, and our discussion in this Chapter is limited to the first three cycles. Beyond the third cycle, a resolution of 256×512 did not provide a converged solution for the R1-C4 case.
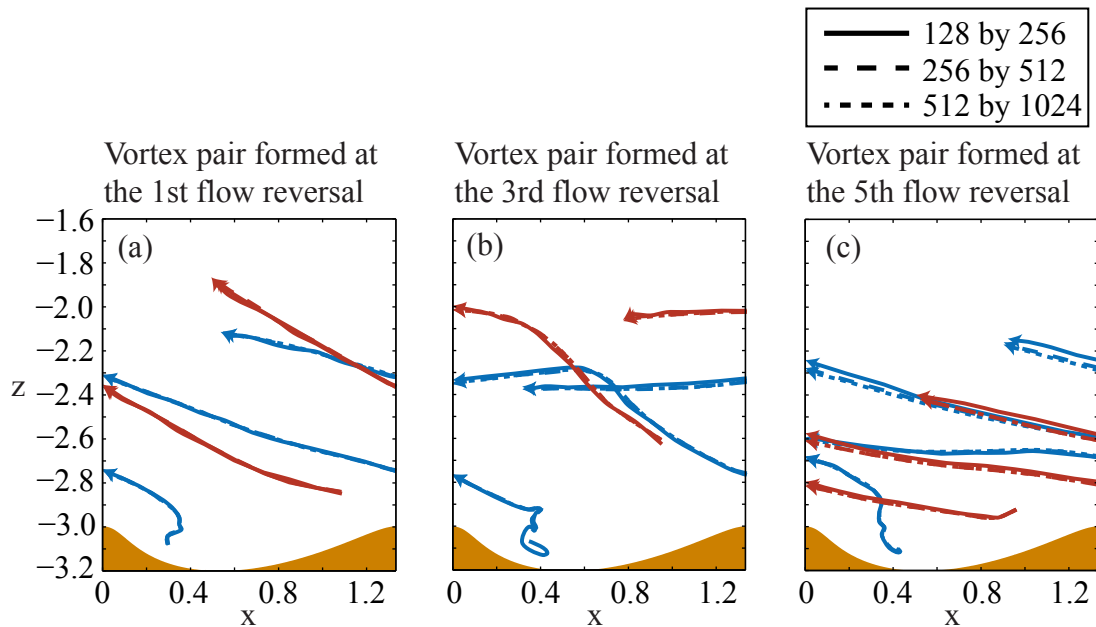
Figure 3.6: Convergence of the vortex paths for the R1-C4 case at grid sizes 128×256, 256×512, and 512×1024. Figures (a), (b), and (c) represent the paths for vortices of the vortex pair formed near the first, third, and fifth flow reversals, respectively. Paths traced in blue (red) are vortex paths with clockwise (counterclockwise) vorticity. The curves that appear as dash-dot are an overlay of the dashed and dotted curves for the two highest resolutions.
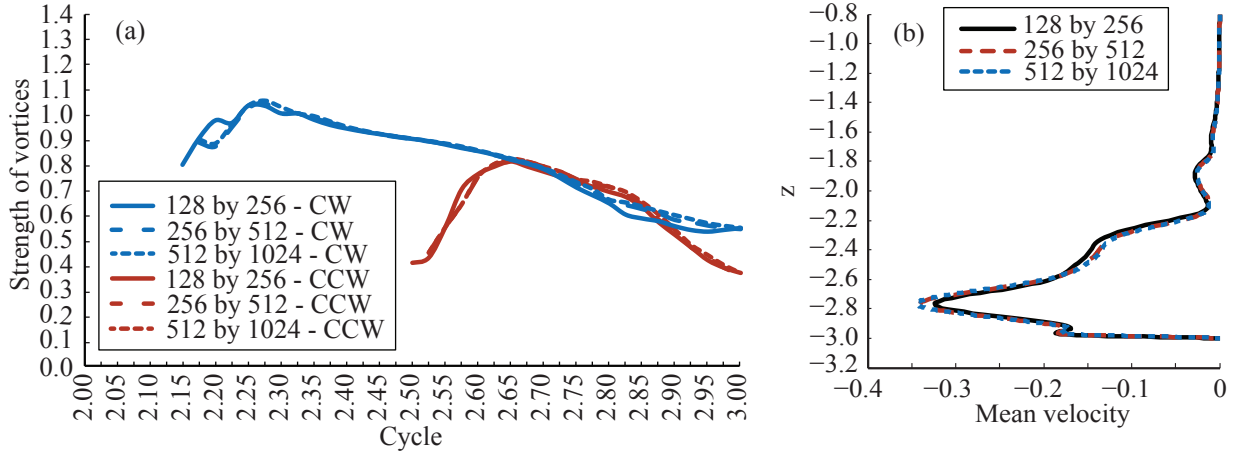
Figure 3.7: Convergence of (a) the strength of the vortices, clockwise (blue) and counterclockwise (red), of the vortex pair formed at the third flow reversal and (b) the mean horizontal current over the entire second cycle for the case R1-C4. The curves represent the strength of the vortex for resolutions 128×256, 256×512, and 512×1024.

3.2 Results and discussion

This section presents a discussion of the sources of vorticity, instantaneous vorticity fields, the paths taken by newly generated vortices, and the early-stage velocity fields for the six base cases, Rm-Cn, $n = 1, 2, 4$ and $m = 0, 1$, which were defined in Section 3.1.1.

3.2.1 Vorticity and its sources

The vorticity $\Omega = u_z - w_x$ is governed by the 2-dimensional incompressible vorticity equation given by

$$\Omega_t + \mathbf{u} \cdot \nabla \mathbf{\Omega} = \frac{1}{Re} \nabla^2 \Omega$$

Let V be the whole domain or a subdomain $a < z < b$, where $-H + h < a < b < 0$, and δV be the boundary of V. Using the incompressibility condition, rearranging, and integrating

29
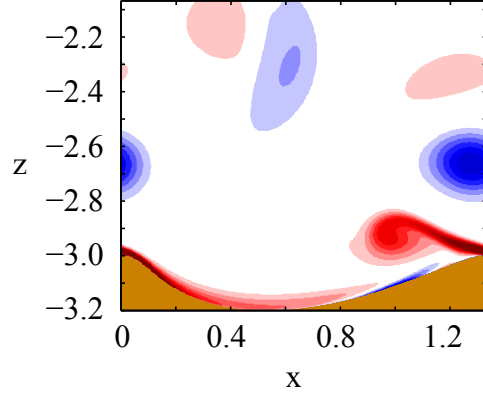
Figure 3.8: Vorticity at $t = 2.5$ cycles for the C4 flow forcing and the R1 ripple shape. Vorticity contours $\Delta\omega = 3.75$, and clockwise (counterclockwise) vorticity is indicated by blue (red) color.

with respect to time and space, we get

$$\underbrace{\iint_V \Omega\,dx\,dz}_{\Omega_{x,V}} = \overbrace{\underbrace{\int_0^t \oint_{\partial V} (u\Omega, w\Omega)\cdot(-\hat{n})\,ds\,dt}_{\Omega_{x,\partial V}} + \frac{1}{Re}\int_0^t \oint_{\partial V} \nabla\Omega\cdot\hat{n}\,ds\,dt}^{\Omega_{x,\partial V,\mu}} \qquad (3.8)$$

$$= \int_0^t \oint_{\partial V} \underbrace{(u\Omega, w\Omega)\cdot(-\hat{n})}_{F_{x,w}}\,ds\,dt + \int_0^t \oint_{\partial V} \underbrace{\frac{1}{Re}\nabla\Omega\cdot\hat{n}}_{F_{x,\mu}}\,ds\,dt \qquad (3.9)$$

where $\hat{n}$ is the unit outward normal to ∂V. If V is the whole domain, $\Omega_{x,\partial V,w} = 0$ everywhere along the upper and lower boundaries and we are only left with shear stresses, which are different on the two boundaries. If V is not the whole domain, we will be interested in the advective as well as shear stress terms.

On a theoretical note, if V is taken as the entire domain, $\Omega_{x,V} \equiv 0$ by Stokes' theorem since it is equal to the circulation around the boundary, which is zero, since $u = w = 0$ along the top and bottom boundaries (no-slip boundary condition) and circulation along the lateral boundaries cancels by periodicity. Vorticity is generated at the solid boundaries and, except in cases of reverse flow at the bottom boundary, which may occur beneath a vortex generated at a ripple crest, for example, is of opposite signs at the top and bottom.

For the R1-C2 case, Figure 3.9(a) shows the evolution of vorticity ($\Omega_{x,V}$) and the

30

integrated viscous shear stresses, ($\Omega_{x,\partial V,\mu,t}$ and $\Omega_{x,\partial V,\mu,b}$, where the subscripts t and b denotes that due to top and bottom boundaries) for the whole domain during the first three periods. As expected, both the upper and the lower boundaries generate the same quantity of vorticity, i.e., $|\Omega_{x\,\partial V,\mu,t}| = |\Omega_{x\,\partial V,\mu,b}|$. The vorticity of the entire domain is zero. Figure 3.9(b) shows a similar plot but for the subdomain $-2.9 < z < -0.4$. Note that $z = -2.9$, located just above the ripple crest, and -0.4 are outside the boundary layer and so fluctuations in vorticity across these lines can be attributed to the passage of vortices. Observe that there is no contribution to vorticity in this subdomain from the upper boundary, either through advection or viscous stress. All vorticity in this subdomain originates from the bottom boundary with advection dominating the vorticity transfer. Considering the whole domain again, Figure 3.9(c-d) shows the time evolution of vorticity flux ($F_{x,\mu}$) at the lower ripple-like boundary and the upper boundary $z = 0$. It is this anisotropic spatio-temporal distribution of vorticity flux at the lower boundary that is giving rise to the generation and transfer of vorticity to the interior of the domain.

3.2.2 Instantaneous vorticity field

This section provides a comparison of the instantaneous vorticity at the first six flow reversals for all six base cases. Conclusions based on the comparison can be summarized as follows: (1) clockwise vortices become stronger with increasing flow asymmetry; (2) counterclockwise vortices grow stronger as flow asymmetry decreases; (3) ripple asymmetry causes substantial changes in vortices only during later time periods.

Figures 3.10-3.15 show the instantaneous vorticity field at each flow reversal during the first three cycles. At the first flow reversal, as shown in Figure 3.10, the more asymmetric currents produce stronger vortices, as expected, since the stronger forward currents produce stronger shear layers than the weaker leftward currents do which undergo flow separation to form vortices. Both ripples shapes produce vortices that are similar in shape, strength, and position. We begin to see slight differences across the two ripples at the second flow reversal, as shown in Figure 3.11. The vortices formed by the asymmetric ripples are slightly weaker. The positions of the remnants of the clockwise vortices (blue) formed earlier differs across the two ripple shapes. As shown by the next few figures, at later times, vortex structures at flow reversals become chaotic due to vortex interactions with previously formed vortices.
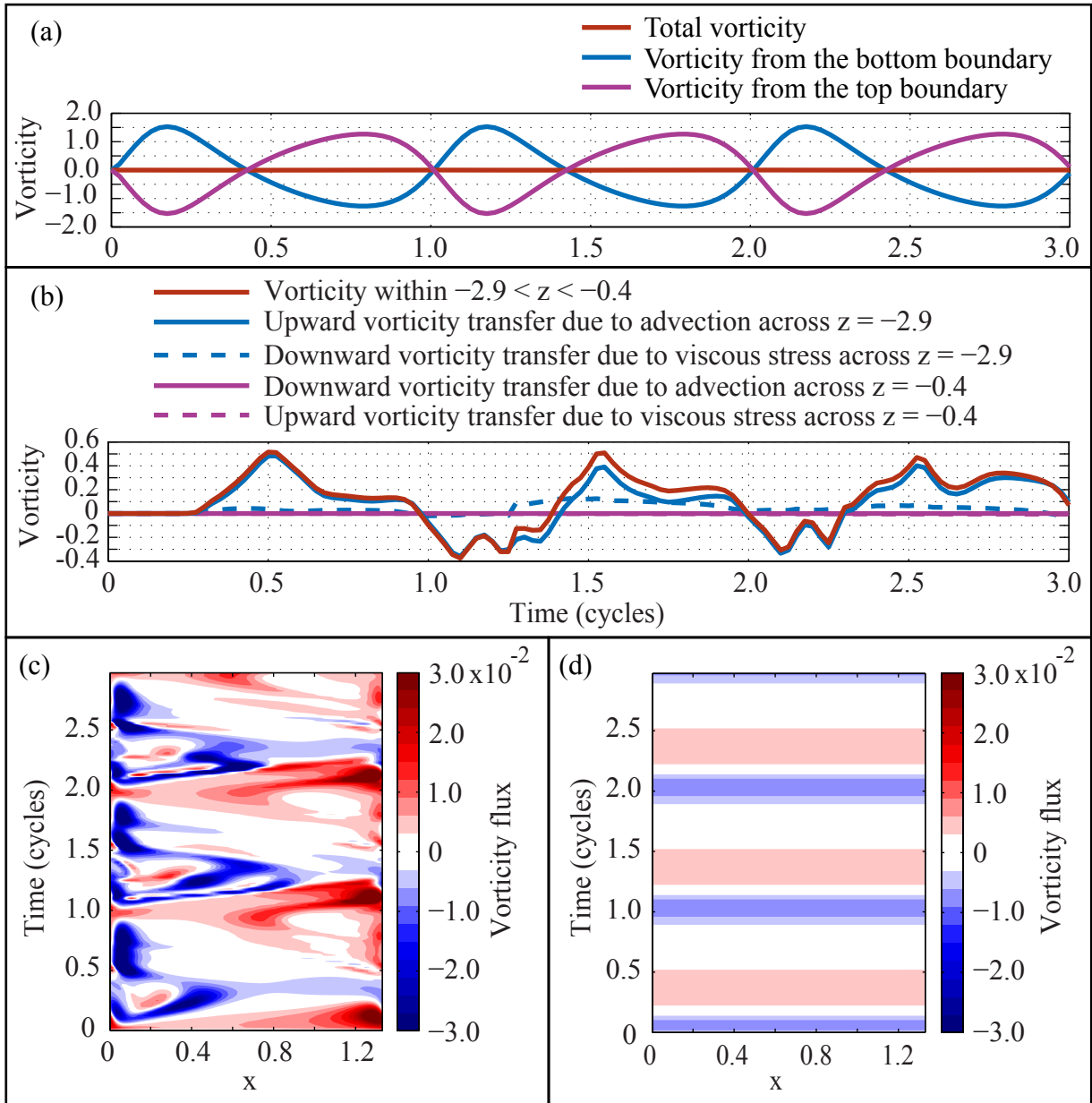
Figure 3.9: Vorticity evolution for the R1-C2 case during the first three periods. (a) Total vorticity (red) in the domain and its viscous shear stress contributions from the top (mulberry) and bottom (blue) boundaries. (b) Total vorticity within $-2.9 < z < -0.4$ (red) and its constituent advective (solid) and diffusive (dashed) contributions crossing the lines $z = -2.9$ (blue) and $z = -0.4$ (mulberry). (c) and (d) shows the distribution of vorticity across the bottom ripple-like and top ($z = 0$) boundaries, respectively.
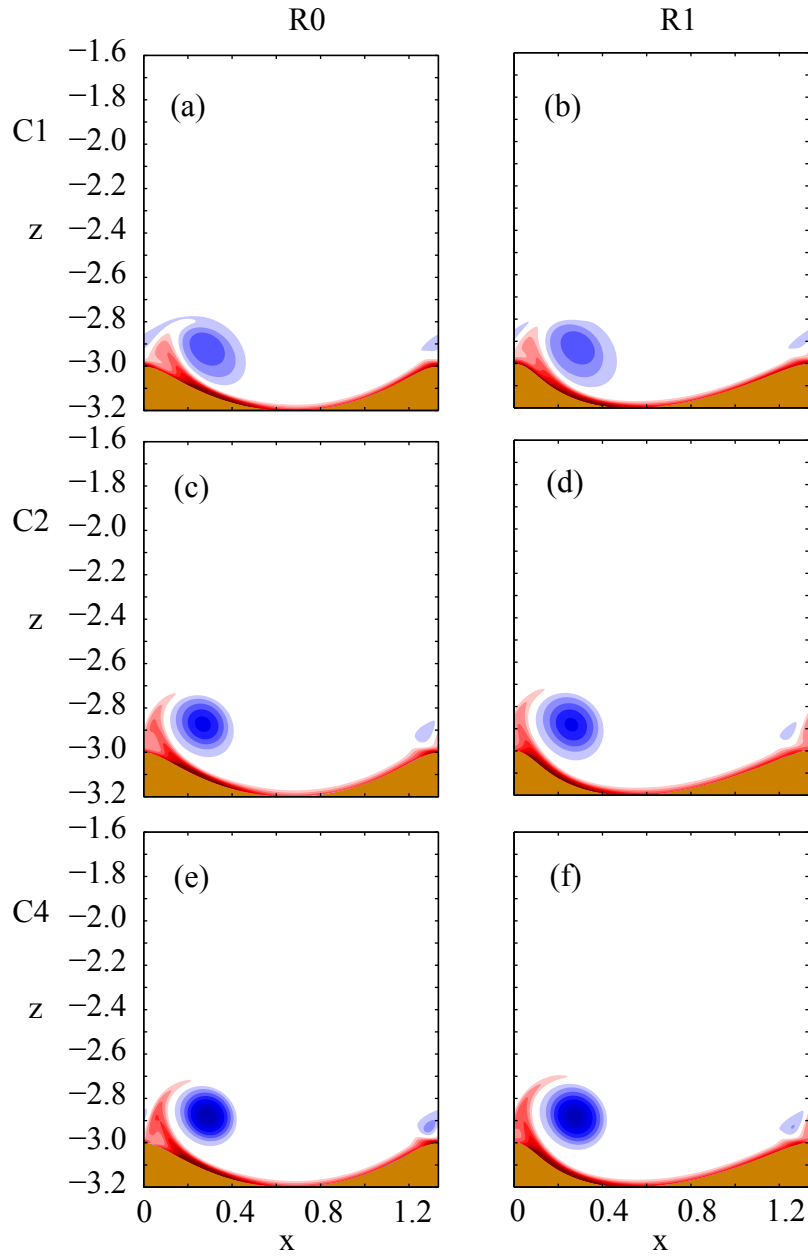
Figure 3.10: Instantaneous vorticity at the 1st flow reversal for the six base cases. Vorticity for ripple shapes R0 and R1 are shown in (a, c, e) and (b, d, f), respectively. Vorticity for flow forcings C1, C2, and C4 are shown in (a, b), (c, d), and (e, f), respectively. Clockwise (counterclockwise) vorticity is indicated by blue (red) color. Vorticity contours $\Delta \omega = 3.75$.
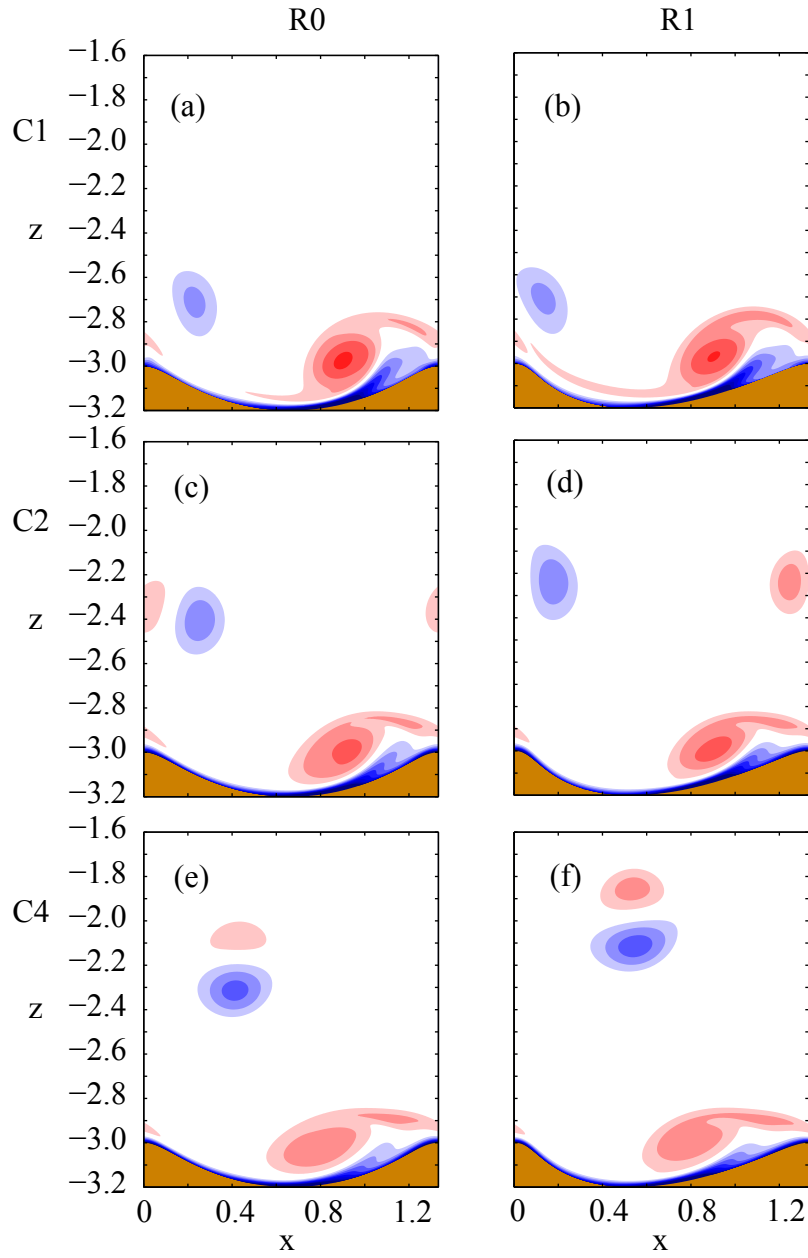
Figure 3.11: Instantaneous vorticity at the 2nd flow reversal for the six base cases. Vorticity for ripple shapes R0 and R1 are shown in (a, c, e) and (b, d, f), respectively. Vorticity for flow forcings C1, C2, and C4 are shown in (a, b), (c, d), and (e, f), respectively. Clockwise (counterclockwise) vorticity is indicated by blue (red) color. Vorticity contours $\Delta\omega = 3.75$.
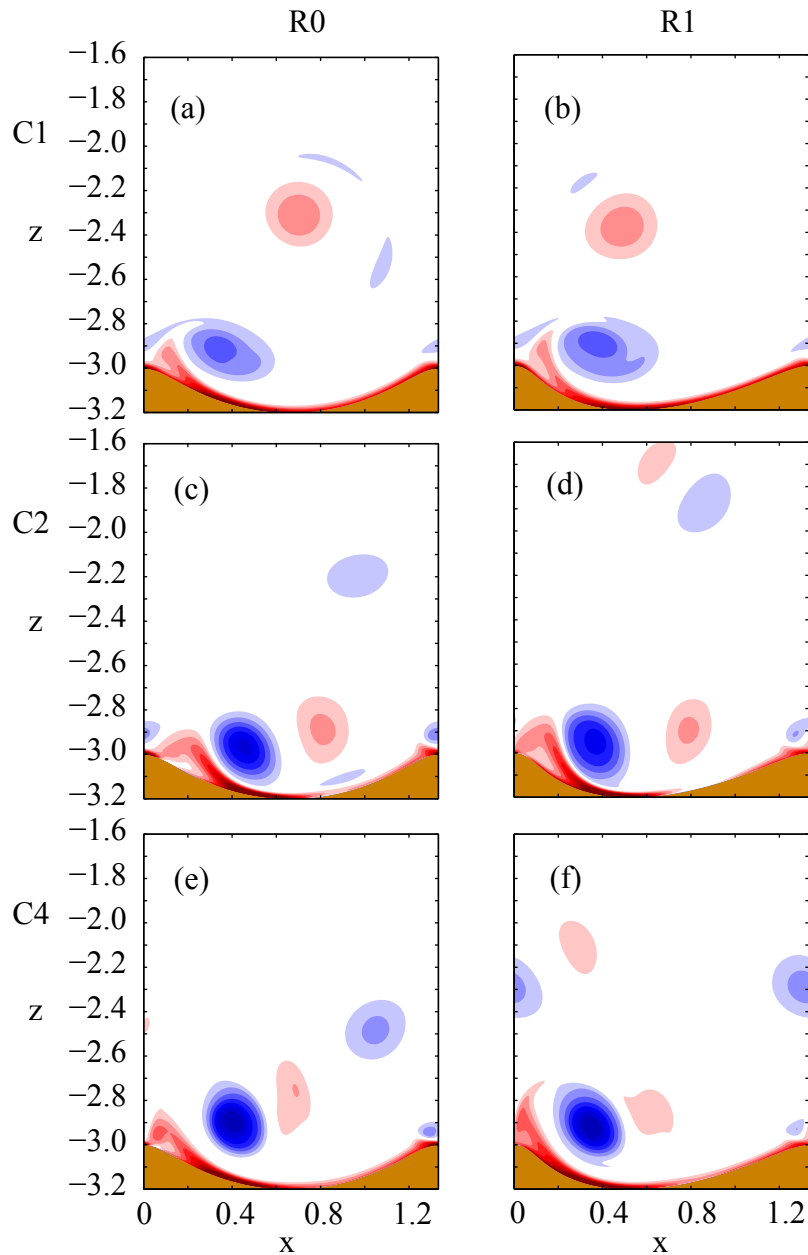
Figure 3.12: Instantaneous vorticity at the 3rd flow reversal for the six base cases. Vorticity for ripple shapes R0 and R1 are shown in (a, c, e) and (b, d, f), respectively. Vorticity for flow forcings C1, C2, and C4 are shown in (a, b), (c, d), and (e, f), respectively. Clockwise (counterclockwise) vorticity is indicated by blue (red) color. Vorticity contours $\Delta \omega = 3.75$.

35
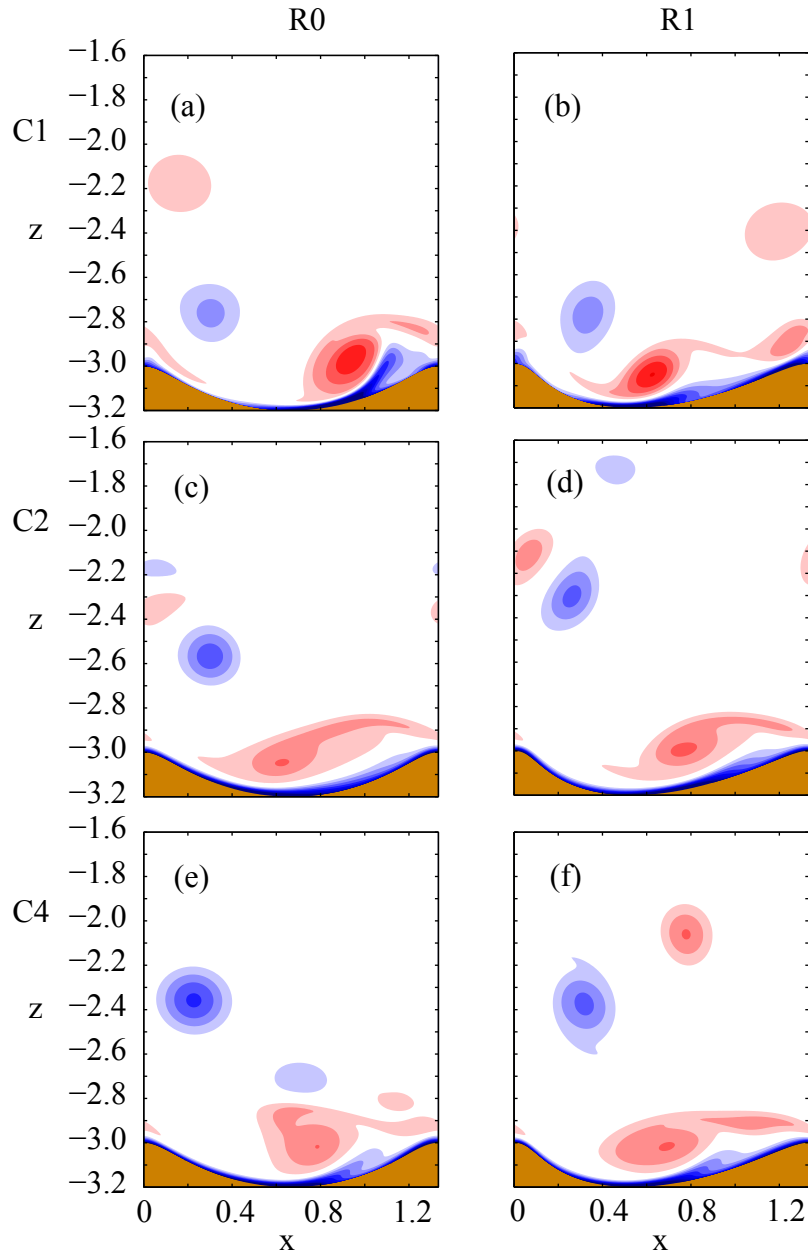
Figure 3.13: Instantaneous vorticity at the 4th flow reversal for the six base cases. Vorticity for ripple shapes R0 and R1 are shown in (a, c, e) and (b, d, f), respectively. Vorticity for flow forcings C1, C2, and C4 are shown in (a, b), (c, d), and (e, f), respectively. Clockwise (counterclockwise) vorticity is indicated by blue (red) color. Vorticity contours $\Delta\omega = 3.75$.
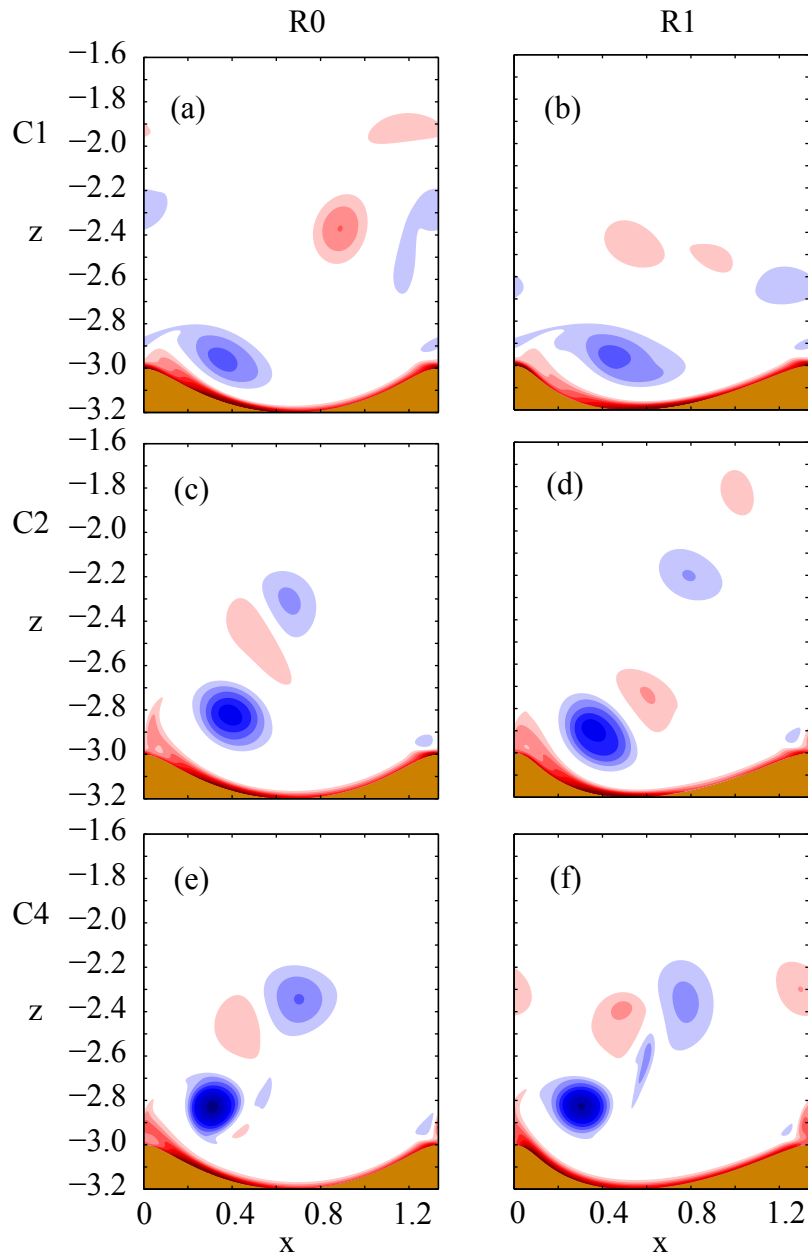
Figure 3.14: Instantaneous vorticity at the 5th flow reversal for the six base cases. Vorticity for ripple shapes R0 and R1 are shown in (a, c, e) and (b, d, f), respectively. Vorticity for flow forcings C1, C2, and C4 are shown in (a, b), (c, d), and (e, f), respectively. Clockwise (counterclockwise) vorticity is indicated by blue (red) color. Vorticity contours $\Delta\omega = 3.75$.
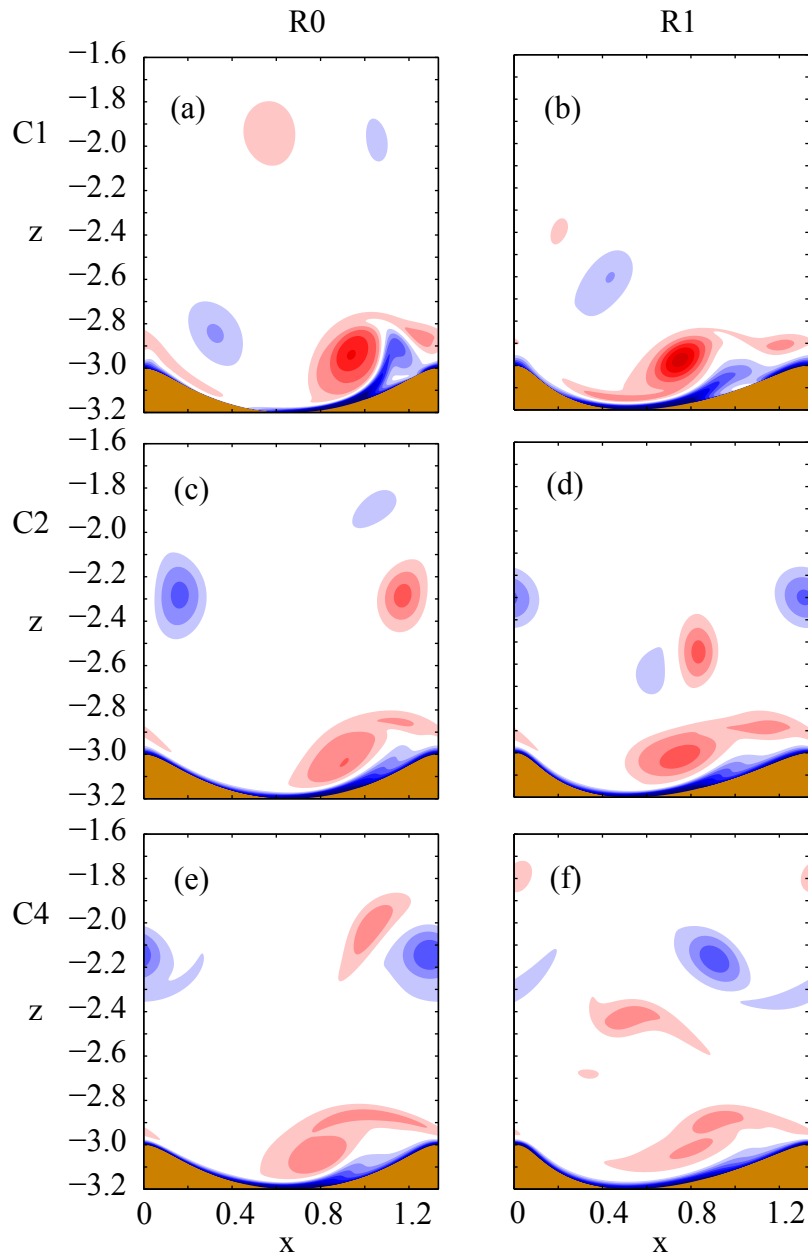
Figure 3.15: Instantaneous vorticity at the 6th flow reversal for the six base cases. Vorticity for ripple shapes R0 and R1 are shown in (a, c, e) and (b, d, f), respectively. Vorticity for flow forcings C1, C2, and C4 are shown in (a, b), (c, d), and (e, f), respectively. Clockwise (counterclockwise) vorticity is indicated by blue (red) color. Vorticity contours $\Delta\omega = 3.75$.

3.2.3 Vortex paths and their strengths

The following discussion, which includes consideration of two ripple shapes and three forcings, addresses the paths taken by the center of these vortices during the first three cycles as well as the strengths of the vortices during the first two cycles.

3.2.3.1 Stages in the formation of vortices

As previously noted, a vortex is generated in each period of rightward and leftward flow. During the first positive part of the flow forcing, a clockwise vortex is formed above the slope to the right of the ripple crest. Upon flow reversal, this vortex moves across the ripple crest and pairs up with a counterclockwise vortex that it helps to generate by the rolling up of the shear layer, as shown in Figures 3.16(a-c). Note that the clockwise vortex is above the counterclockwise vortex just after the formation of the vortex pair. During the leftward flow, the opposite occur, as shown in Figures 3.16(d-f). Since each vortex pair is formed near the time of flow reversal, we will refer to the vortex pair formed in Figures 3.16(a-c) (3.16(d-f)) as the vortex pair generated at the first (second) flow reversal. In the discussions to follow, we consider the vortex pairs associated with the first five flow reversals and label these as FR1, FR2, FR3, FR4, and FR5.

The vortices generated at each flow reversal either move away from the ripple and eventually dissipate, merge with a newly formed vortex at a later time, or exhibit substantial changes as a result of interaction with the ripple. For example, in Figure 3.16(c), the vortex pair moves away from the ripple, as indicated by the green arrow, whereas in Figure 3.16(f), the vortex pair moves toward the ripple and eventually interacts with it. The path of a given individual vortex of a vortex pair generated at a flow reversal is traced until it dissipates, until it undergoes considerable change due to its interaction with the ripple, or until the next flow reversal occurs, whichever event comes first. For the flow forcings chosen for this study (C1, C2, C4), it should be noted that the fluid moves by the excursion distance $s = 1$ between any two consecutive flow reversals, so that the horizontal distance moved by a vortex pair due to the flow forcings alone is identical for all cases. Figure 3.17 illustrates such paths for FR1, when the flow forcing is C4 and the ripple shape is R1.
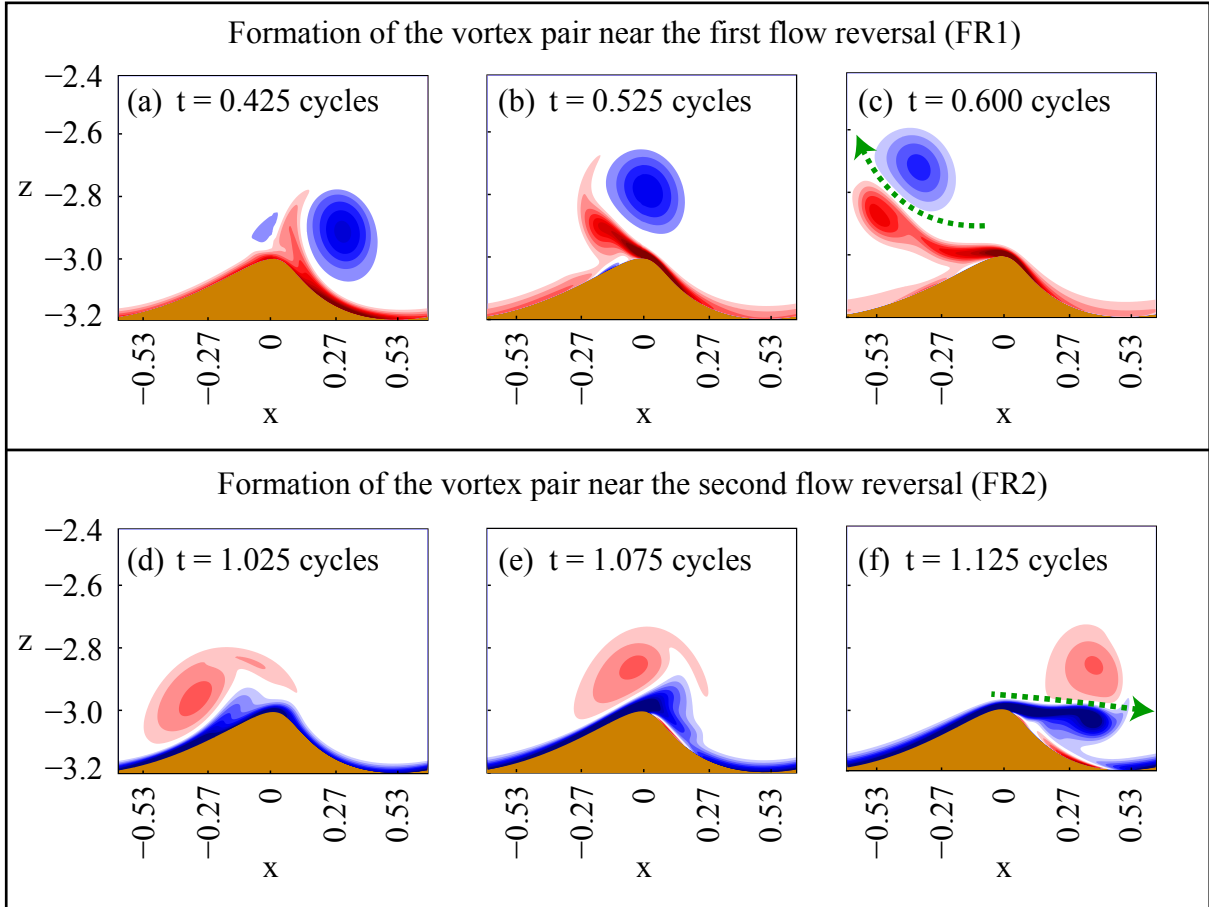
Figure 3.16: Stages in the formation of vortex pairs during the first cycle. Vorticity is shown at times (a) $t = 0.425$, (b) $t = 0.525$, (c) $t = 0.6$, (d) $t = 1.025$, (e) $t = 1.075$, and (f) $t = 1.125$ cycles. The flow forcing is C2 and the ripple shape is R1. Clockwise (counterclockwise) vorticity is indicated by blue (red) color. The clockwise (counterclockwise) vortex assists in the formation and strengthening of the counterclockwise (clockwise) vortex. Vorticity contours $\Delta\omega = 3.75$. Flow reversals occur at 0.44 and 1 cycles.
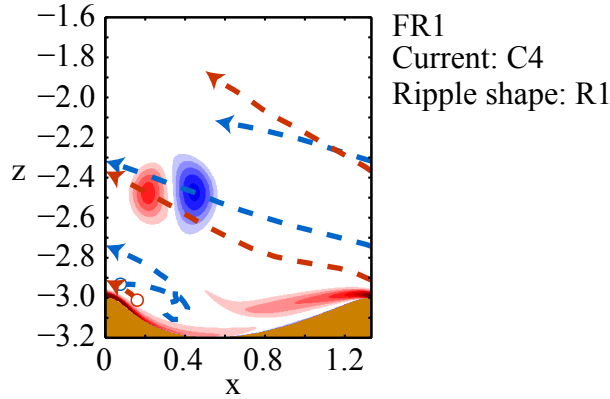
Figure 3.17: Illustration of paths of the two vortices constituting the vortex pair generated at the first flow reversal for the R1-C4 case in the absence of any background current. The vorticity contours are plotted at time 0.65 cycles. Clockwise (counterclockwise) vorticity is indicated by blue (red) color and vorticity contours $\Delta\omega = 3.75$. Paths traced in blue (red) are vortex paths with clockwise (counterclockwise) vorticity.

3.2.3.2 Vortex paths in the absence of a background current

Figure 3.18 shows how the vortex paths evolve for all six base cases over the first three periods. Each figure shows four vortex paths: clockwise (blue) and counterclockwise (red) vortices associated with the R0 (solid) and R1 (dash) ripple shapes. These four vortices form two vortex pairs. As observed and confirmed in earlier studies (Blondeaux & Vittori, 1991; Longuet-Higgins, 1981), the clockwise vortex is generated during rightward flow and the counterclockwise one during the immediately following period of leftward flow. Let us designate these vortex paths as Rm-Cn-CW and Rm-Cn-CCW, where $n = 1, 2, 4$, $m = 0, 1$, and CW (CCW) refer to clockwise (counterclockwise).

CASES: FR1, FR3, AND FR5

This section demonstrates that, for the vortex pairs generated during the transition from rightward to leftward flow (first, third, and fifth flow reversals): (1) vortex pairs move higher as flow asymmetry increases; (2) vortex pairs move higher for the asymmetric ripple only when the flow forcings are strong; (3) the leftward movement increases as flow asymmetry increases, and (4) the movement of a vortex pair is related to the individual strengths of its constituent vortices.

41
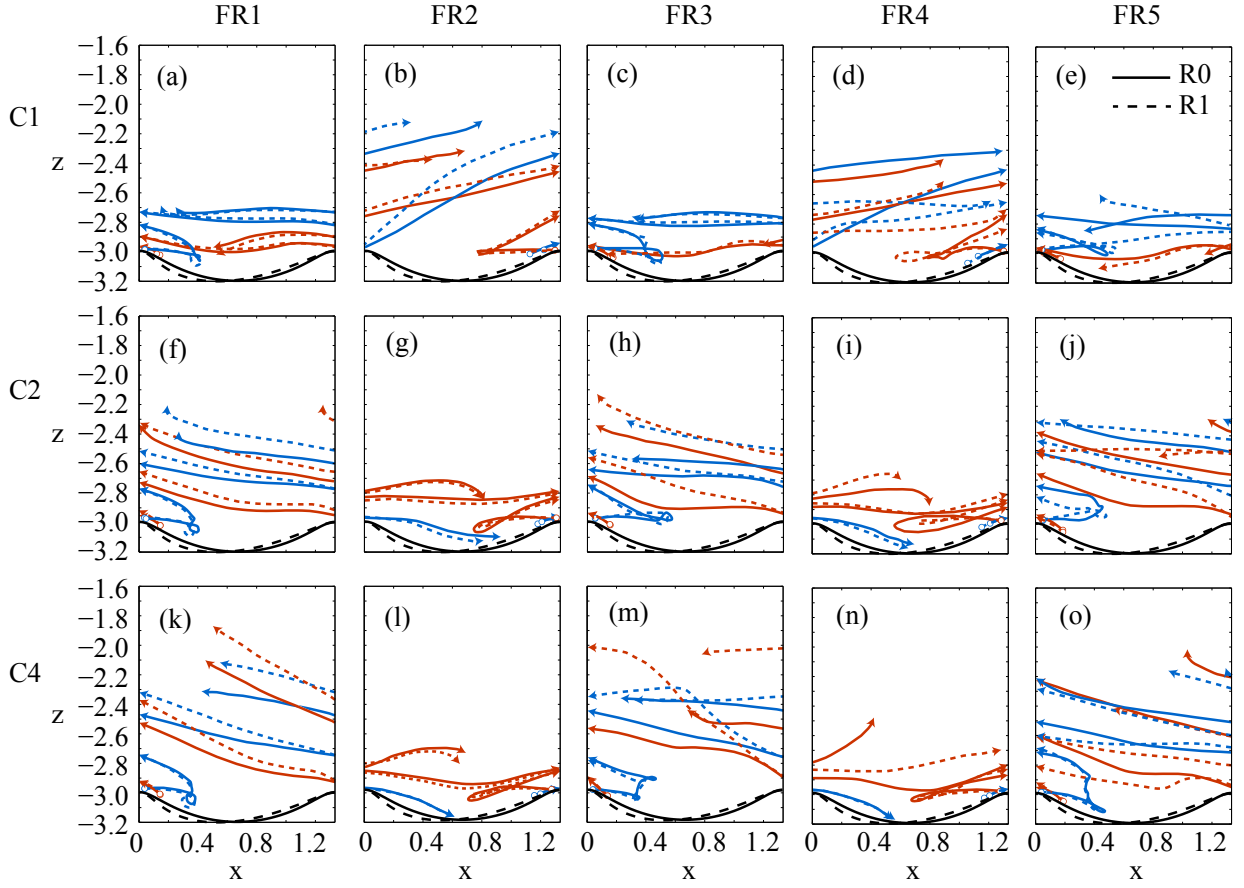
Figure 3.18: Variations in the paths of the vortex centers for the six base cases. Paths in blue (red) correspond to clockwise (counterclockwise) vorticity. FR1, FR2, FR3, FR4, and FR5, shown in (a, f, k), (b, g, l), (c, h, m), (d, i, n), and (e, j, o), respectively, represent paths of vortices of the vortex pairs generated at the first, second, third, forth, and fifth flow reversals, respectively. Vortex paths for the flow forcings C1, C2, and C4 are shown in (a)-(e), (f)-(j), and (k)-(o), respectively.

Let us first consider results for the three currents over the first three periods, in the absence of a background current, and examine the sensitivity of the vortex paths to changes in ripple shape. For the symmetric current C1, as shown in Figures 3.18(a,c,e), the vortex paths do not show any consistent sensitivity to changes in ripple shape. With respect to the clockwise vortices (blue), both ripple shapes result in vortices that travel nearly the same horizontal distance, just over two ripple lengths to the left. In terms of the maximum height reached, it can be seen that all vortices reach nearly the same height, with the exception of R1-C1-CW, which travels to a higher position during the third cycle.

The insensitivity of the vortex paths to changes in ripple shape that can be observed for C1 does not hold for the C2 and C4 asymmetric forcings, which have stronger rightward flows. In general, vortices travel higher up in the presence of stronger currents. In this particular case, the fact that the vortex pairs tend to rise higher up can be attributed to the difference in the strength of the vortices that comprise the vortex pair. A vortex pair whose constituent vortices are of equal strength would be expected to travel in a straight line if they are situated far from boundaries. In contrast to the C1 case, the vortices generated by C2 and C4 move away from the boundary quickly enough that they avoid interacting with the strong shear layer near the bottom boundary. Vortices that interact with the bottom shear layer after its formation tend to weaken quickly, which prevents the pairing of a clockwise and counterclockwise vortex to form a vortex pair, an effect observed only for the C1 current. Figures 3.19(a) and 3.19(b) indicate the strength of these vortices during the first two cycles. The strength of the clockwise vortices increases much faster than that of the counterclockwise vortices, resulting in a rapid increase in the difference between the vorticities of the two vortices that form a vortex pair. When clockwise and counterclockwise vortices pair up, the stronger, clockwise vortex is positioned above the counterclockwise vortex. This positioning results in the vortex pairs moving in a curve-up direction. For a given current and period, it is also evident that the initial trajectories of the lone clockwise vortices (prior to their pairing up with counterclockwise vortices) nearly coincide. This finding is further evidence that the difference in the strengths of the vortices in the vortex pairs contributes to their observed trajectories. As shown in Figure 3.18(m), a degree of chaotic behavior can be noted; i.e., the vortex trajectories change direction abruptly due to the interaction between a vortex pair and an older vortex. The effect of this vortex interaction is indicated in Figure 3.19(b), in which R1-C4-CW can be seen to increase rapidly in strength around $t = 1.55$ due to a merger with an older clockwise vortex.

Another effect of the asymmetric currents is that vortex pairs tend to travel a longer distance horizontally, an effect that can be attributed to the slightly stronger vortices, both clockwise and counterclockwise, that are generated by the asymmetric currents.
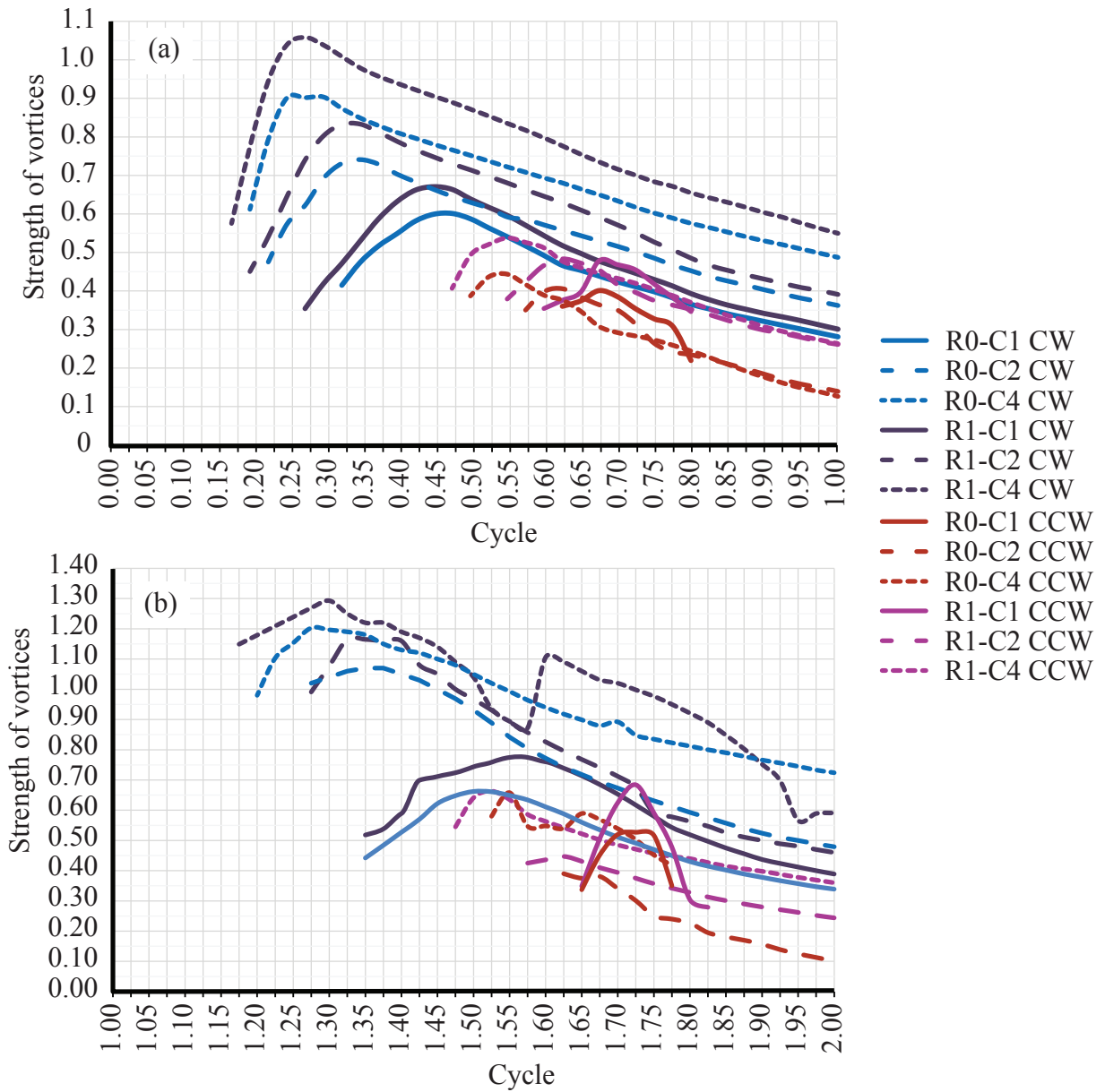
Figure 3.19: Variations in the strength of the vortices for the six base cases during the (a) first and (b) second periods. Clockwise (counterclockwise) vorticity is indicated by CW (CCW).
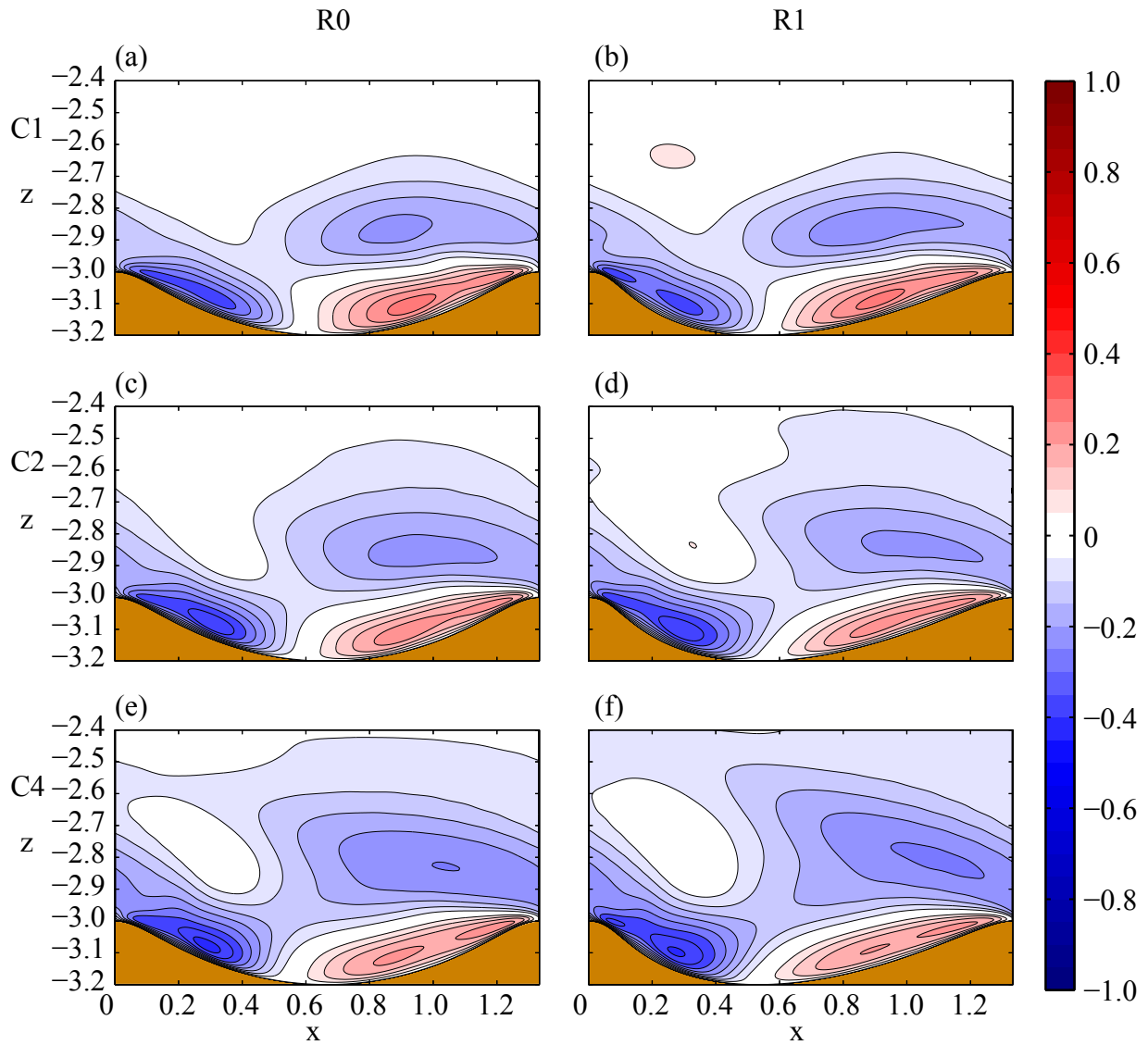
Figure 3.20: Mean horizontal velocities over the first cycle for the six base cases. Velocities for ripple shapes R0 and R1 are shown in (a, c, e) and (b, d, f), respectively. Velocities for flow forcings C1, C2, and C4 are shown in (a, b), (c, d), and (e, f), respectively. Leftward (rightward) velocity is indicated by blue (red) color.
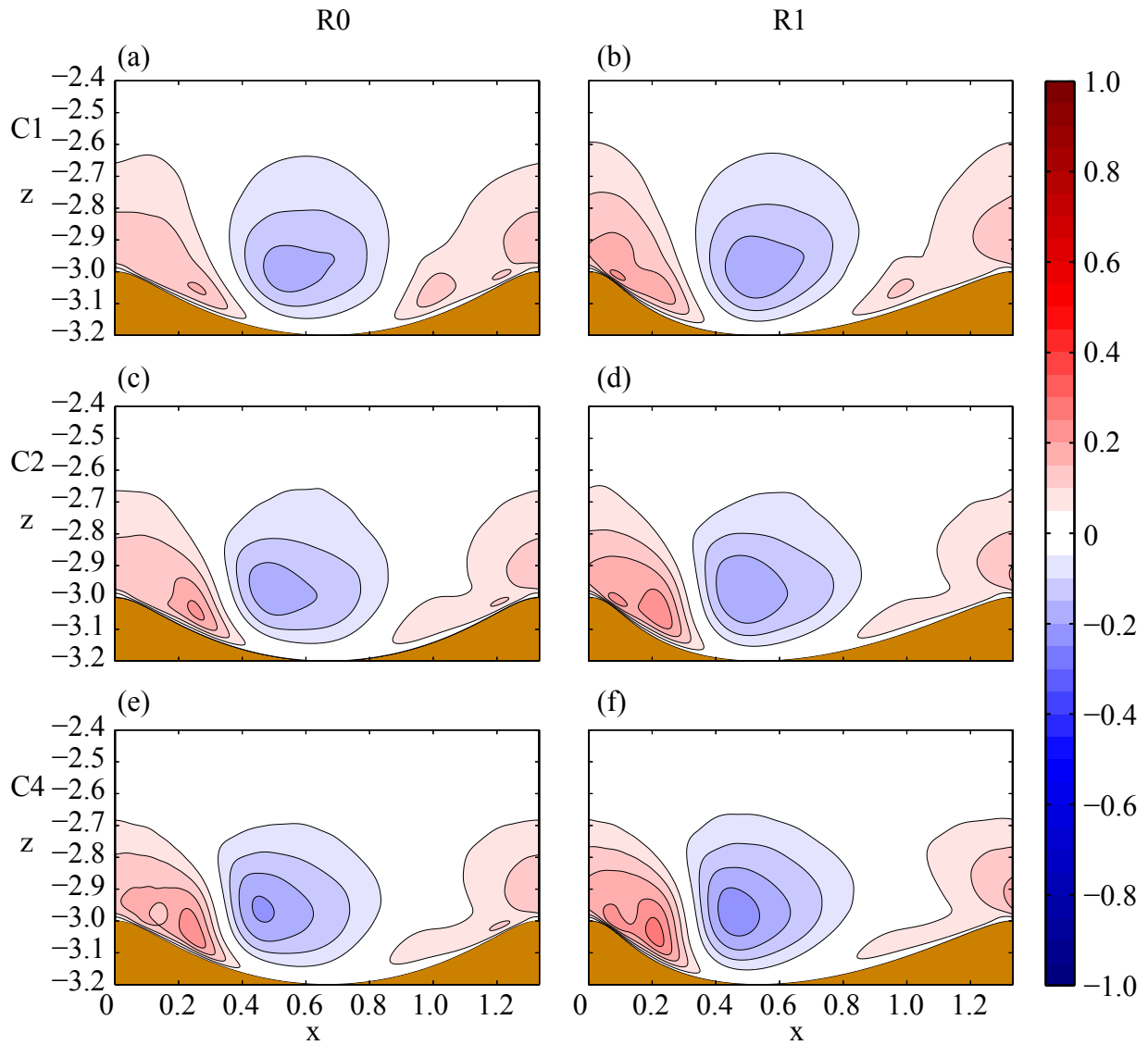
Figure 3.21: Mean vertical velocities over the first cycle for the six base cases. Velocities for ripple shapes R0 and R1 are shown in (a, c, e) and (b, d, f), respectively. Velocities for flow forcings C1, C2, and C4 are shown in (a, b), (c, d), and (e, f), respectively. Upward (downward) velocity is indicated by the red (blue) color.

46

Figures 3.20 and 3.21 show the distribution of mean horizontal and vertical velocities over the first cycle. The blue and red colors respectively indicate leftward and rightward velocities (Figure 3.20) and downward and upward velocities (Figure 3.21). It can be seen that for all three currents, stronger leftward (above the ripple crest level) and downward (near the ripple center) mean currents are associated with the asymmetric ripple. This finding is consistent with the vortex movements observed: the vortices exhibit a tendency to dip slightly when traveling below $z = -2$ (approximately) over the ripple trough.

Compared to the sensitivity exhibited by the vortex paths with respect to changes in the flow asymmetry, the results indicate that vortex paths are much less sensitive to changes in the Reynolds number. Figures 3.22(a,b) shows the vortex paths for current C1*, which is identical to current C1 but simulated at $Re = 1550$, rather than at $Re = 1250$. Decreasing the viscosity increases the Reynolds number while retaining the same forcing. It should be noted that the higher Reynolds number results in the vortices moving only slightly higher up for FR1, and slightly lower for FR2. In contrast, Figure 3.22(c,d) shows the vortex paths for the current C2*, which is identical to current C2 but simulated at $Re = 1250$, rather than at $Re = 1550$. With the lower Reynolds number, the vortices move slightly less high than that for C2. To see the effect of flow asymmetry, as defined by (3.3), we observed the vortex paths generated by the brown curve in Figure 3.24, whose peak velocity is the same as that for C2. Figure 3.23 shows the vortex paths that occurred. The parameters applied to obtain this forcing are $\alpha = 1.23$, $b = 0.49$, $\psi = 0$, and $\phi = 0$. With this current, for FR1, the vortex paths were observed to travel nearly the same distance horizontally but slightly less far vertically than with C2. Vortex paths for FR2 remains similar to that of C2. These results indicate that vortex paths are more sensitive to changes in $\max_{t \in [0,T]} |u(t)|$ than to changes in the flow asymmetry.

CASES: FR2 AND FR4

This section shows that, for vortex pairs generated during the transition from leftward to rightward flow (second and fourth flow reversals), (1) vortex pairs move higher up only with the symmetric current, (2) vortex pairs generated by the asymmetric currents are short-lived due to their interactions with the ripple, and (3) the movement of a vortex pair is related to the individual strengths of its constituent vortices.

With respect to the symmetric current, as indicated in Figures 3.18(b,d), there is no consistent trend that indicates sensitivity of the vortex paths to the ripple shape. One notable observation is that the vortex pairs reach higher up in FR2 and FR4 than in FR1, FR3, or FR5. Again, this effect can be explained in terms of the strengths of the individual vortices in the vortex pairs, which are shown in Figure 3.26(a) for the first
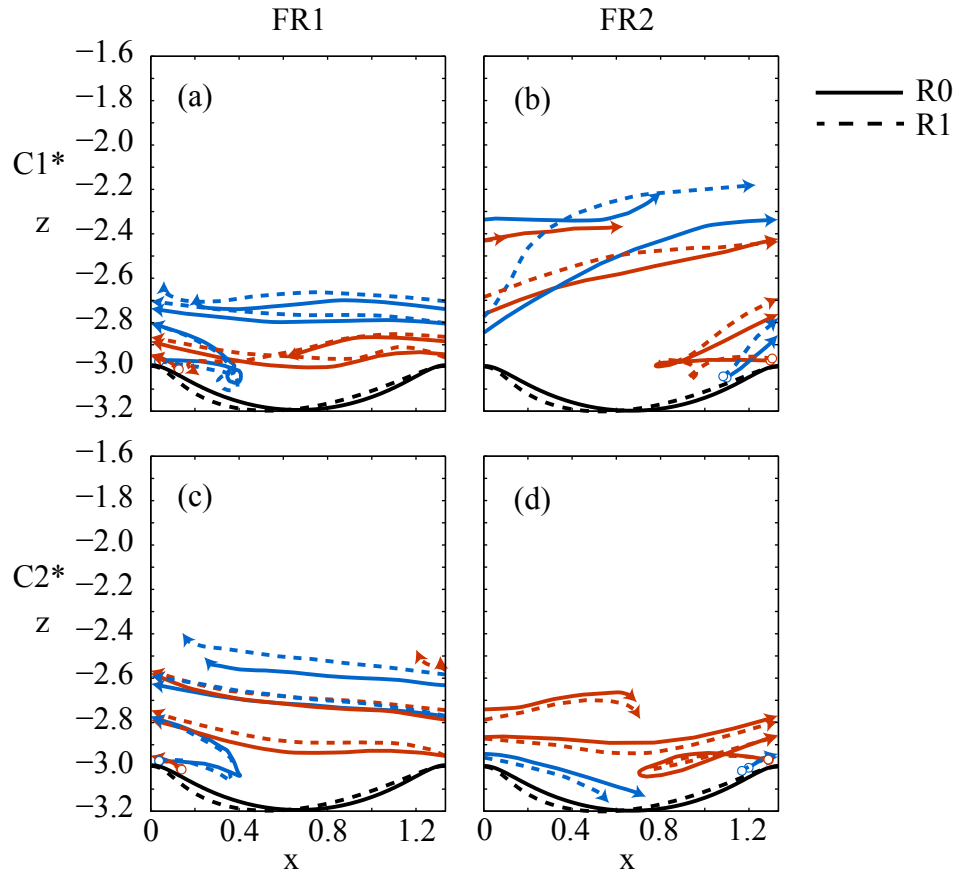
Figure 3.22: Vortex paths for the currents (a,b) C1* and (c,d) C2* and ripple shapes R0 and R1. C1* and C2* are the same as the C1 and C2 currents but simulated at $Re = 1550$ and $Re = 1250$, respectively. Curves in blue and red represent vortex paths with clockwise and counterclockwise vorticity, respectively. Solid and dashed curves represent vortex paths generated by the ripple shape R0 and R1, respectively.
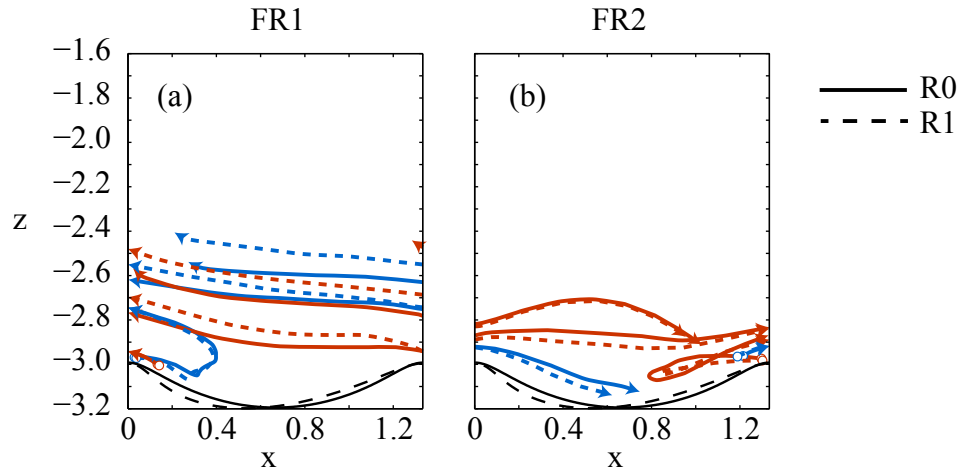
Figure 3.23: Vortex paths for the current corresponding to the brown curve in Figure 3.24 and the R1 and R2 ripple shapes. Vortex paths corresponding to the first and second flow reversal is shown in (a) and (b), respectively.
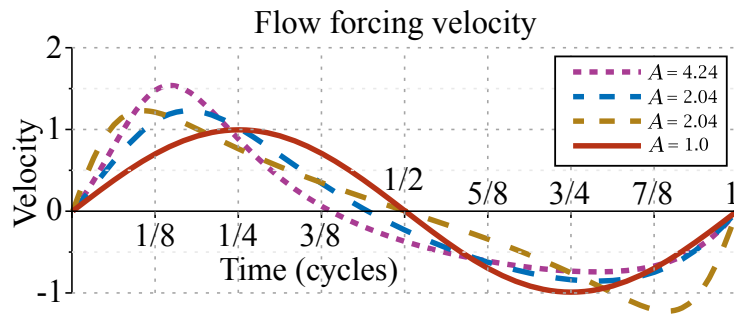
Figure 3.24: An excursion-length-preserving flow forcing (brown) whose peak velocity is the same as that in C2 (blue). The other curves represent the flow forcings C1 ($A = 1.0$), C2 ($A = 2.04$), and C4 ($A = 4.24$) used in the numerical experiments.
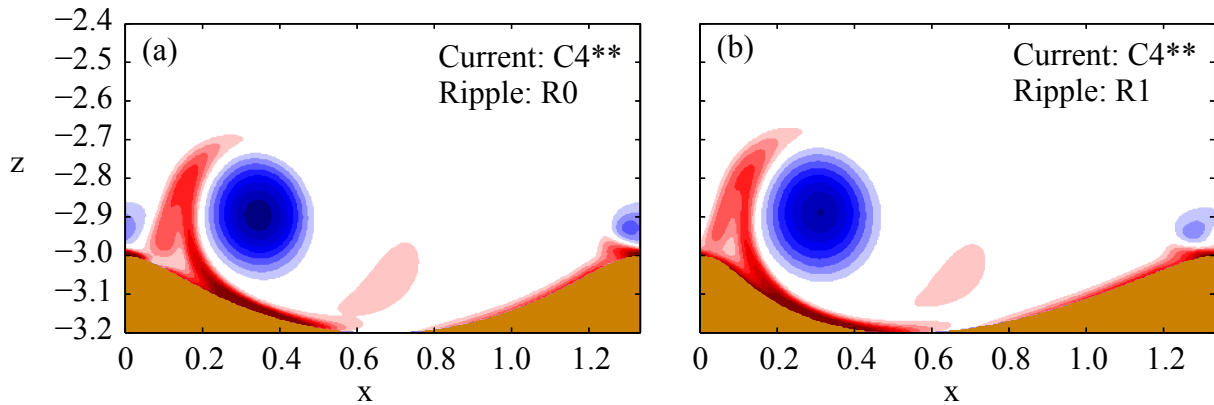
Figure 3.25: Vortices formed at the end of the first period for the (a) R0 and (b) R1 ripple shapes and flow forcing C4**. C4** is the same as the C4 flow forcing but with the simulation initiated with the weaker, negative part of the flow preceding the stronger, positive part. Clockwise and counterclockwise vorticity is represented by blue and red colors, respectively.

period. After the formation of the vortex pair, around 1.15 cycles, the clockwise vortex is considerably weaker than the counterclockwise vortex and, as pointed out in section 3.2.3.1, the clockwise vortex is below the counterclockwise one, which causes the vortex pair to move in a curve-up direction, making it rise higher.

In contrast to the symmetric current, for the asymmetric currents, the vortex pairs remain close to the ripple surface, and the clockwise vortex is short-lived. As can be seen in Figure 3.26(b), during the brief period that the clockwise vortex exists, approximately 1.125 to 1.2 cycles, it is stronger than and located below the counterclockwise vortex, driving the vortex pair to move in a curve-down direction, which causes the clockwise vortex to impinge on the ripple. This interaction of the clockwise vortex with the ripple makes the vortex short-lived: the green arrows in Figure 3.26(b) indicate the times at which the clockwise vortices impinge on the ripple. The counterclockwise vortex, which remains, continues to move rightward in the vicinity of the ripple.

This sensitivity of the paths and strengths of the vortices to the asymmetry of the ripple was not observed in a similar study by Kim *et al.* (1994). In their study, the ratio of the ripple height to length, h/l, ranged from 0.11 to 0.22 with 0.03 increments, which includes the 0.15 value that we used here. The s/l value they employed was 1.04, which is greater than our value of 0.75. Ripple asymmetry is defined as the ratio of the longer half
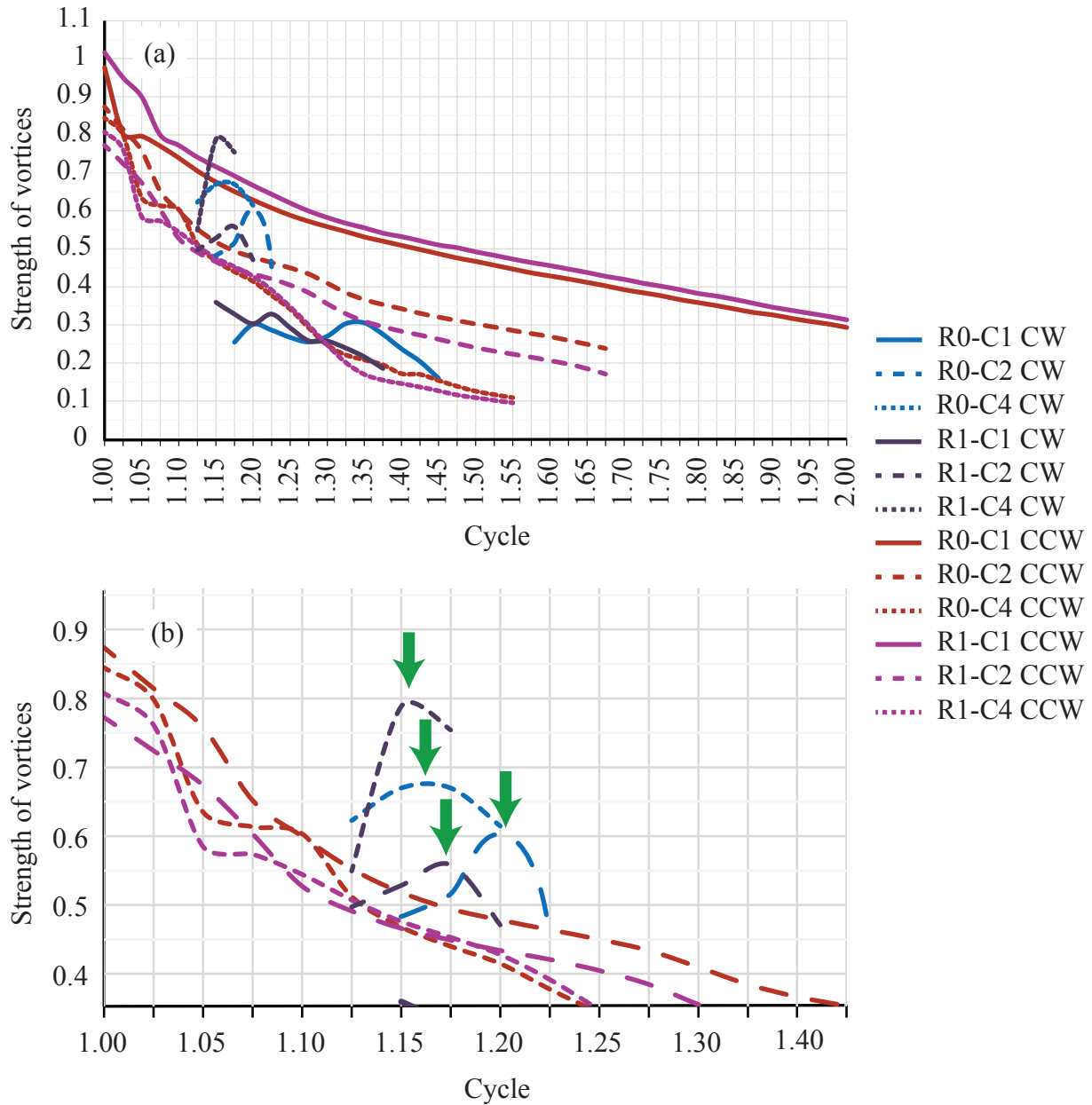
Figure 3.26: (a) Variations in the strength of the vortices of the vortex pair formed at the second flow reversal (FR2) for all six base cases. Clockwise (counterclockwise) vorticity is indicated by CW (CCW). (b) Zoom in on the part of panel (a) to show the clockwise vorticity curves with the green arrows indicating the time at which they interact with the ripple.

51

of the ripple to the ripple length and ranges from 0.50 to 0.70 with 0.05 increments, which includes the approximately 0.6 value that we use in this study. However, the Reynolds number used by Kim *et al.* (1994) was much higher, approximately $Re = 27\,714$; the governing equations were the Reynolds-averaged Navier-Stokes equations with a turbulence closure; and the numerical method was based on finite difference (in a regular grid). Due to their use of a turbulence closure model, note that the effective Reynolds number will be lower than 27 714 since a numerical viscosity is contributed from the turbulence closure model. In addition, the flow forcings were initiated slightly differently, with the weaker, negative part of the wave preceding the stronger, positive part. With this initiation of the simulation and consideration of the first period alone, the effect of the ripple asymmetry on the vortex paths cannot be observed since the allotted time is insufficient for the newly generated vortices to pair up and propagate. This interpretation is confirmed by the results displayed in Figure 3.25, in which the vortex centers for both ripple shapes are positioned at nearly the same place at the end of the first period.

To help explain the reason for the observed stronger vortices associated with the asymmetric ripple, let us consider the mean horizontal velocity for time durations between flow reversals, since the source of energy for vortex growth is created during these times. Figures 3.27 and 3.28 show the mean horizontal velocities during the first periods of rightward and leftward flow, respectively. It can be observed that the strength of the reverse velocity generated during the period of the first rightward flow is stronger in the case of the asymmetric ripple, which helps generate a stronger clockwise vortex. However, the reverse velocity during the second half of the cycle is weaker for the asymmetric ripple. The stronger counterclockwise vortex generated by the asymmetric ripple during the first leftward flow is a side effect of the stronger clockwise vortex that was generated during the period of the first rightward flow. With respect to the asymmetric ripple (R1) and the C2 flow forcing, the clockwise vortex first travels rightward, as shown in Figure 3.18(f). Then, during the period of leftward flow, as shown sequentially in Figures 3.16(a)-(c), it helps separate the boundary layer to form a counterclockwise vortex that it pairs up with and strengthens.

3.2.3.3   Vortex paths in the presence of a background current

This section explains how, in addition to exhibiting the general features observed in the no-current case, when there is a passive background current of -0.15 on top of the active oscillatory flow, (1) the vortices move slightly shorter distances leftward for C1, (2) the vortices move further leftward for the asymmetric flows, and (3) the movement of a vortex is related to the individual strengths of the constituent vortices in the vortex pairs.
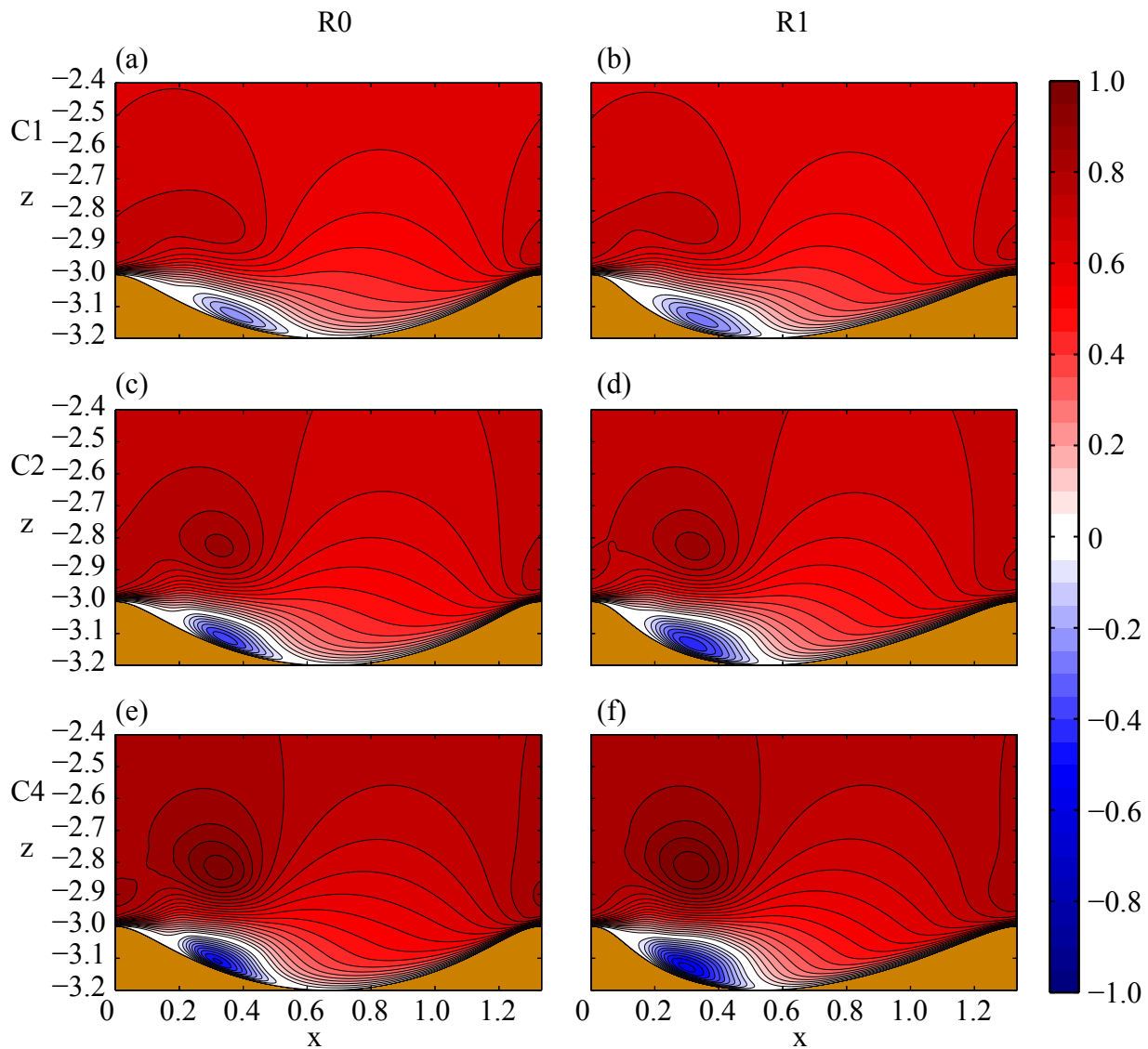
Figure 3.27: Mean horizontal velocities over the first period of rightward flow for the six base cases. Velocities for ripple shapes R0 and R1 are shown in (a, c, e) and (b, d, f), respectively. Velocities for flow forcings C1, C2, and C4 are shown in (a, b), (c, d), and (e, f), respectively. Leftward (rightward) velocity is indicated by blue (red) color.
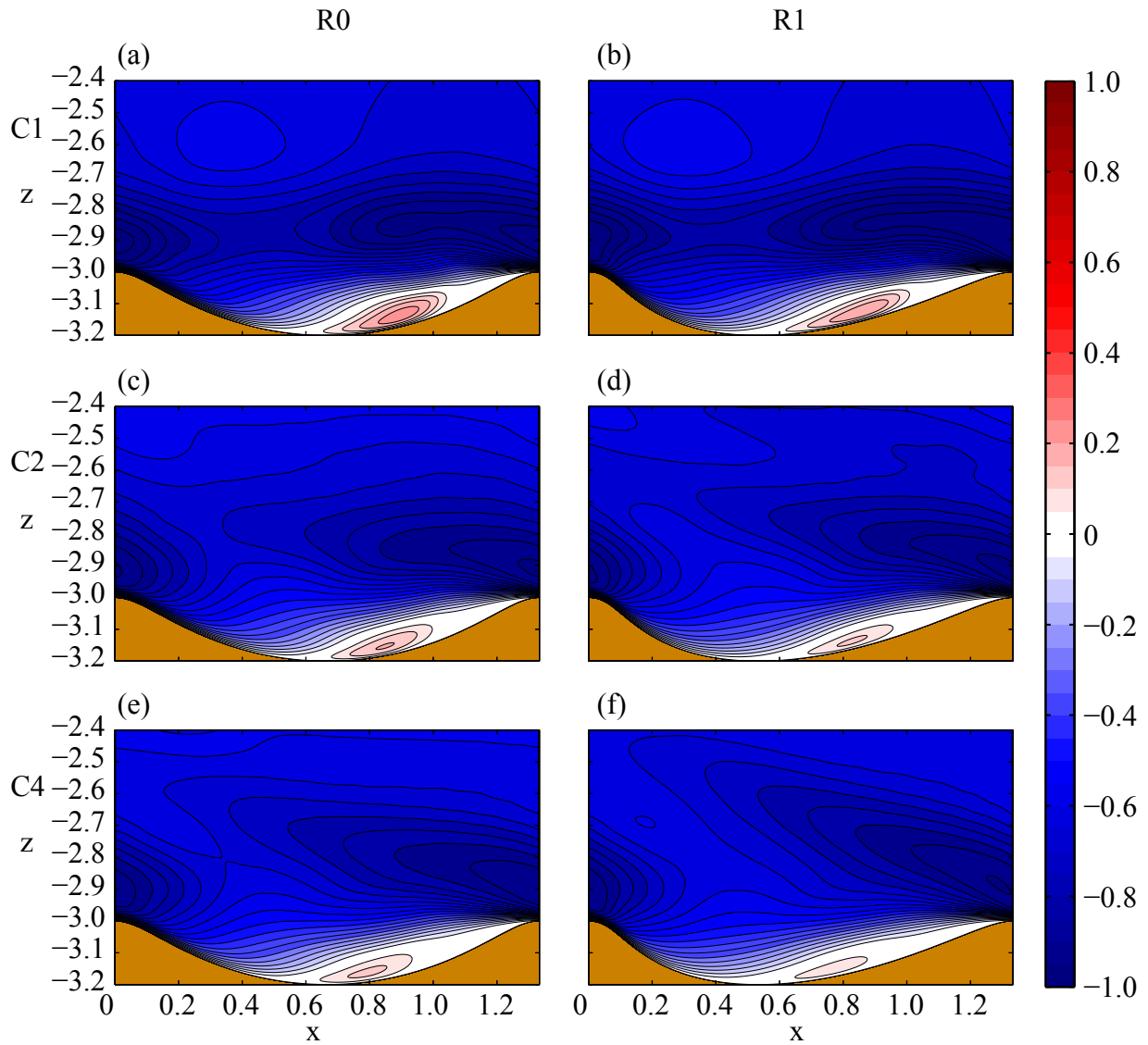
Figure 3.28: Mean horizontal velocities over the first period of leftward flow for the six base cases. Velocities for ripple shapes R0 and R1 are shown in (a, c, e) and (b, d, f), respectively. Velocities for flow forcings C1, C2, and C4 are shown in (a, b), (c, d), and (e, f), respectively. Leftward (rightward) velocity is indicated by the blue (red) color.

Figure 3.29 depicts the vortex paths for the R0 and R1 ripple shapes when the currents are $u_{Ci} + u_b$, where u_{Ci} is the velocity associated with the currents Ci, $i = 1, 2, 4$, and $u_b = -0.15$ is a passive background current. Such background currents, with respect to both direction and strength, are often associated with the asymmetric ripples found in nature (Dumas *et al.* , 2005; Sekiguchi & Yokokawa, 2008; Testik *et al.* , 2006). The corresponding graphs showing the vortex strengths are presented in Figure 3.30 for the vortices of the vortex pairs formed at the first, third, and fifth flow reversals.

CASES: FR1, FR3, AND FR5

The paths of vortex pairs generated during the transition from rightward to leftward flow show little sensitivity to ripple shape or background current for the C1 flow forcing. Vortices are, however, observed to travel a slightly shorter distance for C1, when compared with the corresponding no-current case illustrated in Figures 3.18(a-e). This effect can be attributed to the fact that these vortices are closer to the bottom boundary and are generally weaker, as revealed by a comparison of Figures 3.30(a,b) with Figures 3.19(a,b). Weaker vortex pairs would be expected to propel themselves more slowly, and their close proximity to the boundary would diminish the effect of the background current, hence making them slower overall. In contrast, for the stronger currents, C2 and C4, the vortex pairs are observed to travel further left when compared with that of the no-current case, because these vortex pairs are relatively far from the boundaries, so that the effect of the background current is strong and compensates for their relatively slower self-propulsion. Apart from these differences, the vortex paths exhibit trends similar to those observed in the cases with no background current.

CASES: FR2, FR4

As in the no-current case, for the vortex pairs generated during the transition from leftward to rightward flow, although the height reached is somewhat less, the vortex pairs move higher up only with the symmetric flow forcing. Like the observations in the no-current case, the findings for this case reveal that the vortex pairs formed by the asymmetric forcings interact with the ripple surface and are short-lived.

3.2.3.4   Higher Reynolds numbers

We consider the effect of increasing the Reynolds number by a factor of four to $Re = 5000$. This increase in the Reynolds number is achieved by decreasing the viscosity while preserving all other parameters of the flow, as indicated in Table 3.1. For these higher
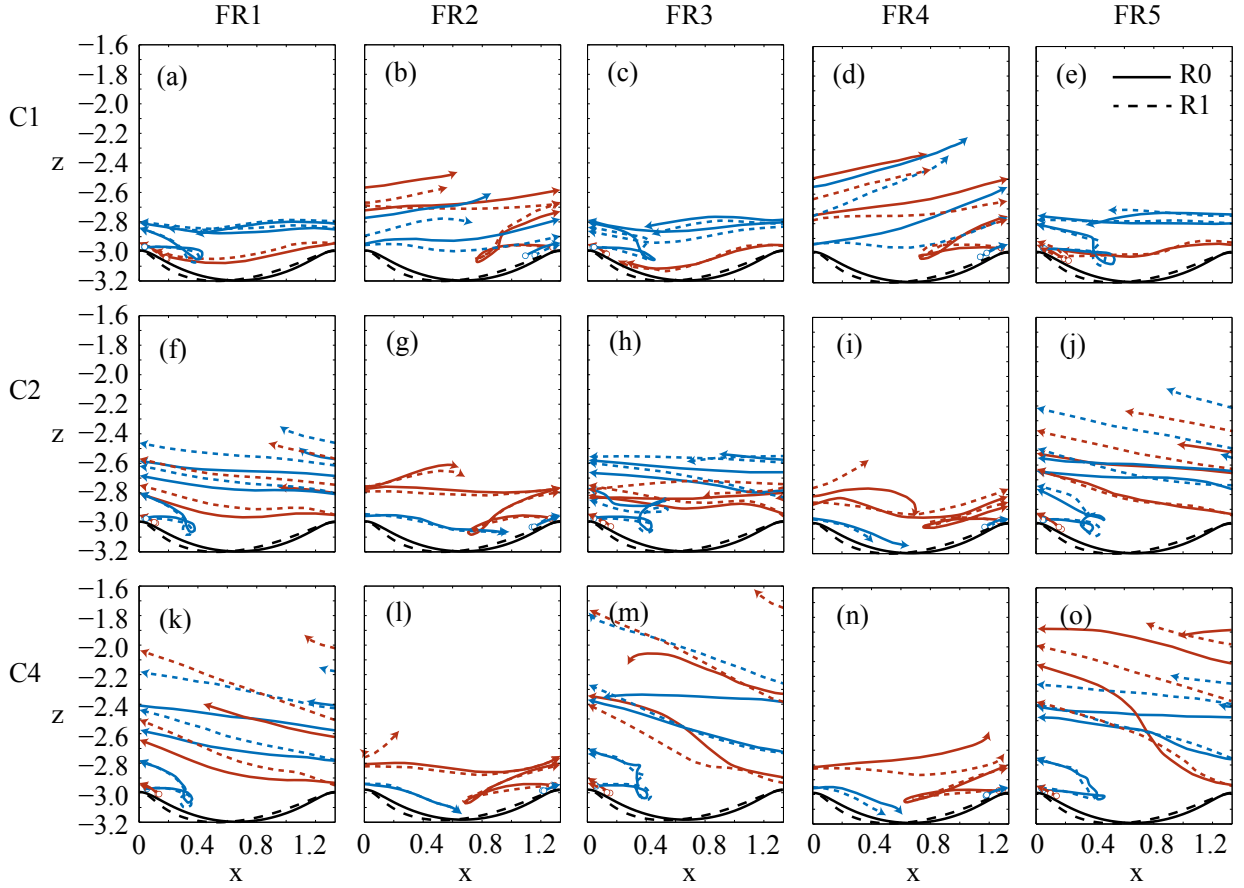
Figure 3.29: Variation in the paths of the vortex centers for the R0 and R1 ripple shapes when the currents are $u_{Ci} + u_b$ where u_{Ci} is the velocity associated with the currents Ci, $i = 1, 2, 4$, and $u_b = -0.15$ is a passive background current. Paths in blue (red) corresponds to clockwise (counterclockwise) vorticity. FR1, FR2, FR3, FR4, and FR5 represent paths of vortices of the vortex pairs generated at the first, second, third, forth, and fifth flow reversals, respectively.
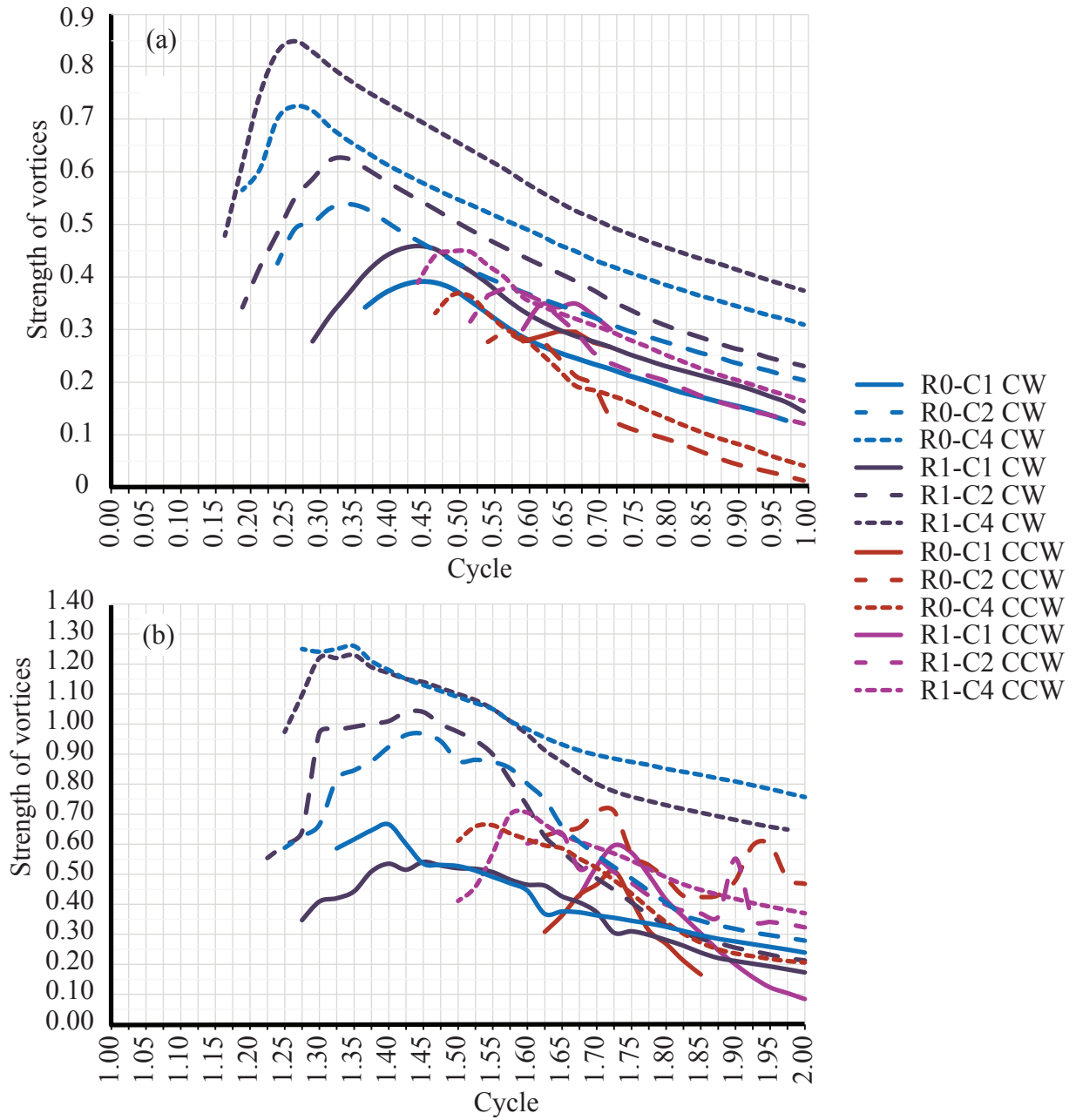
Figure 3.30: Variation in the strength of the vortices for the R0 and R1 ripple shapes when the currents are $u_{Ci} + u_b$, where u_{Ci} is the velocity associated with the currents Ci, $i = 1, 2, 4$, and $u_b = -0.15$ is a passive background current. Vortex strengths are shown for the (a) first and (b) second cycles. Clockwise (counterclockwise) vorticity is indicated by CW (CCW).

Reynolds numbers, we use the 512×1024 grid, which resulted in convergence up to the first cycle.

Figure 3.31 shows the variations in the paths of the vortex centers for all six base cases when the Reynolds number $Re = 5000$. Considering Figures 3.31(a,b), the vortices tend to move higher up than in the lower Reynolds number cases. Again, this can be attributed to the larger difference in the strengths of the two vortices that constitute the vortex pair. This fact can be observed in Figure 3.32, which shows the strengths of each vortex pair for the six base cases. Note also the lower rate of decay of vorticity in the higher Re cases. For the R1-C4 case, whose vortex paths are shown in Figures 3.31(a-c), the trend we observed earlier for the lower Reynolds number ($Re = 1250$), the vortex pairs reaching higher for the asymmetric ripple and more asymmetric currents, is not consistently observed due to the early onset of vortex interactions. Figures 3.33 and 3.34 compare the instantaneous vorticity field at the end of the first cycle. As expected, it can be observed that the higher Reynolds number cases result in stronger longer lasting vortices, in addition to the creation of smaller vortices that are not observed at lower Reynolds numbers.
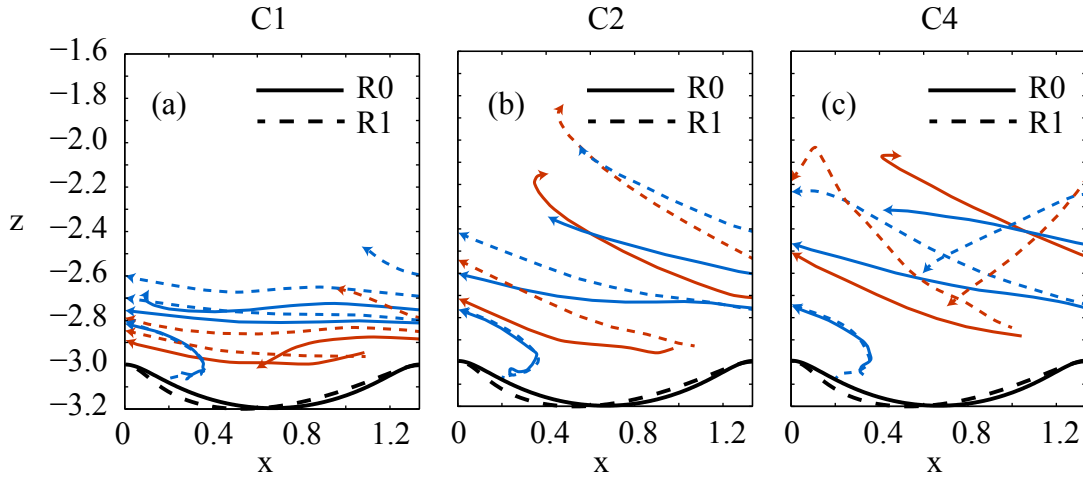
Figure 3.31: Variations in the paths of the vortex centers for ripple shapes R0 and R1 when the currents are (a) C1, (b) C2, and (c) C4 and Reynolds number $Re = 5000$. Paths in blue (red) correspond to clockwise (counterclockwise) vorticity.
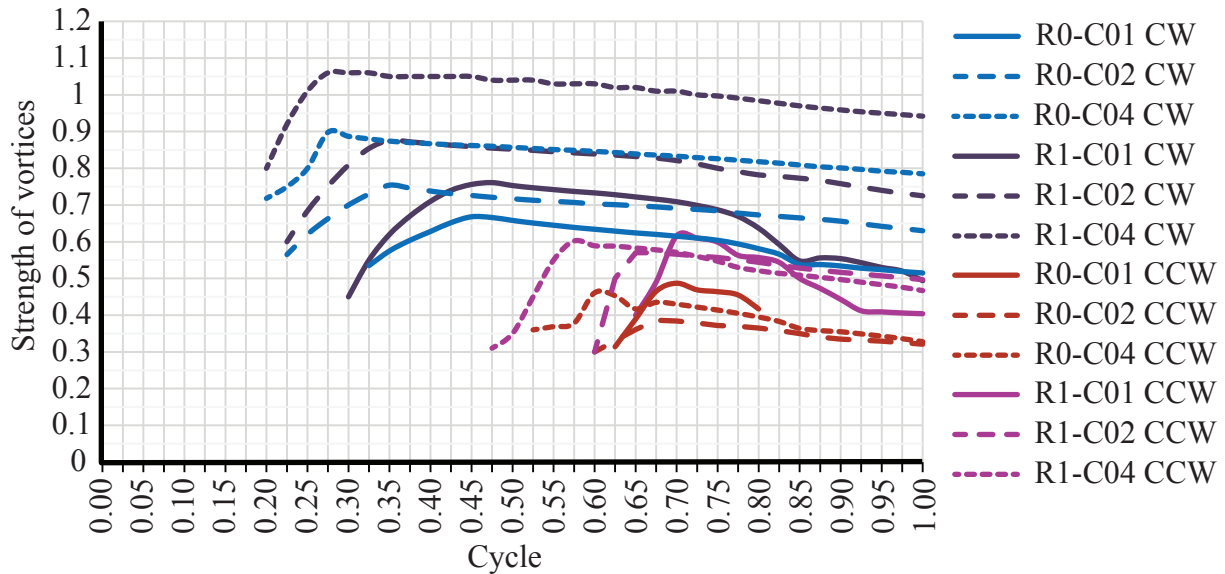
Figure 3.32: Variations in the strength of the vortices during the first cycle for the R0 and R1 ripple shapes when the currents are C1, C2, and C4 and Reynolds number $Re = 5000$.

3.3   Conclusion

In this numerical study, we investigated the effect of asymmetric ripple shapes and flow forcing on the initial trajectories and strengths of newly generated vortex pairs in 2D oscillatory flows over a ripple bed. In addition to experiments involving purely oscillatory flow, simulations were conducted in the presence of a passive background current that was used to mimic undertow currents. The flow forcing was initiated from rest, and the simulations were carried out for three cycles. The numerical method employs the use of a pseudo-spectral technique for solving the incompressible Navier-Stokes equations in 2D.

The simulations were conducted with the following parameters: the height-to-length ratio of the ripple shapes was fixed at 0.15, the flow forcings were constrained to give an excursion length of three-quarters of the ripple length, and the Reynolds numbers were fixed at 1250 and 5000. Under these constraints, the asymmetric forcings were chosen to resemble shapes observed in nature, following Malarkey & Davies (2012), and the asymmetric ripple shapes were generated by adding a slight ripple-area-preserving deviation to the symmetric ripple shape used by Blondeaux & Vittori (1991). The passive background current was -0.15, i.e., 15% of the maximum velocity of the symmetric flow forcing.
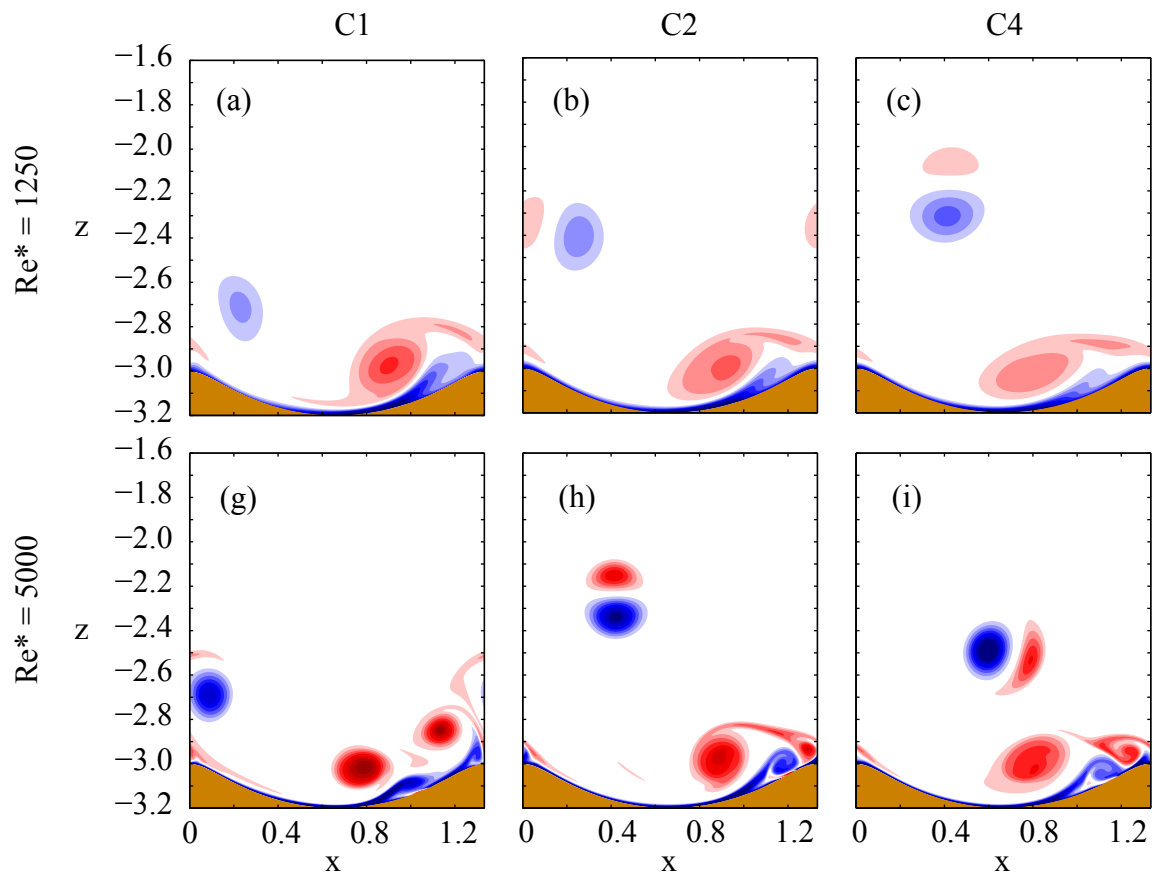
Figure 3.33: Instantaneous vorticity field after one cycle for the ripple shape R0 when currents are (a, g) C1, (b, h) C2, and (c, i) C4 with the Reynolds numbers (a)-(c) 1250 and (g)-(i) 5000. Clockwise (counterclockwise) vorticity is indicated by blue (red) colors. Vorticity contours $\Delta\omega = 3.75$.
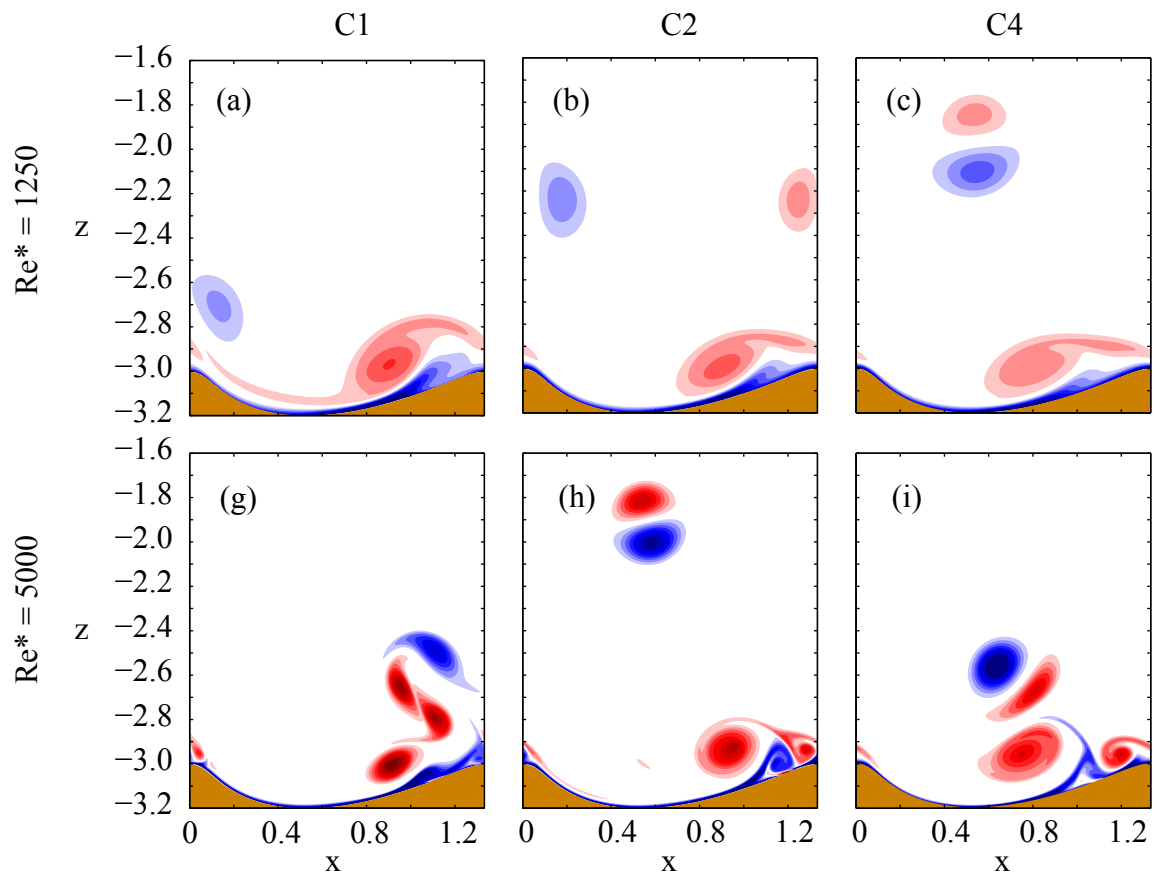
Figure 3.34: Instantaneous vorticity field after one cycle for the R1 ripple shape when currents are (a, g) C1, (b, h) C2, and (c, i) C4 with Reynolds numbers (a)-(c) 1250 and (g)-(i) 5000. Clockwise (counterclockwise) vorticity is indicated by blue (red) colors. Vorticity contours $\Delta\omega = 3.75$.

Considering the transitions from rightward to leftward flow (FR1, FR3, and FR5), for each oscillatory cycle, apart from the typical vortex movements reported in the literature, the results indicate that, compared to a symmetric ripple, an asymmetric ripple generates a vortex pair that is stronger and travels further horizontally (leftward) and vertically (upward). This effect is further increased by the asymmetry in the oscillatory forcing. With respect to an individual vortex pair, it was also observed that a stronger vortex is first generated during a period of stronger rightward flow, as expected, and that during a period of weaker leftward flow, this stronger vortex helps create another vortex that exhibit an opposite vorticity. However, for the weakest, symmetric, oscillatory flow forcing (C1), the strengths of the vortices and the distances they traveled were largely insensitive to the asymmetry of the ripple. For cases FR2 and FR4, the vortex pairs formed by the symmetric forcings reach higher, while those formed by the asymmetric forcings interact with the ripple and are short-lived. As discussed in the next chapter, this asymmetry in vortex ejections associated with asymmetries in the ripple and currents persists in long runs, resulting in the establishment of a near-bed negative mean current.

Similar but diminished trends were exhibited by the vortex paths when the flow forcings had a passive background current on top of the active oscillatory forcing. The passive background current was observed to affect only those vortex paths located relatively far from the bottom boundary.

For the higher Reynolds number, $Re = 5000$, the vortex pairs associated with FR1 and FR3 were observed to move higher when compared to that of $Re = 1250$. However, unlike when $Re = 1250$, due to the early onset of vortex interactions, vortex pair movements were somewhat chaotic for FR5.

Chapter 4

Evolution of the vorticity and flow field generated by oscillatory flows over ripples at the quasi-steady state

4.1   Introduction

We now extend the investigation of the previous chapter to longer times by considering the flow field out to 40 cycles. In the study conducted by Blondeaux & Vittori (1991), simulations were carried out for up to five cycles for the case in which $Re = 1250$, $h/l = 0.15$, and $s/l = 0.75$, which are the parameters used for the work presented in this thesis. Figure 2.4 in Chapter 1 demonstrates that the result of our simulations are close to their findings. The clockwise vortices were observed to be somewhat different after five cycles. Barr *et al.* (2004) used 15 cycles to obtain results at the quasi-steady state. In our simulations, vortex structures can be observed to reach some degree of quasi-steadiness after 15 cycles. The convergence results shown in section 3.1.2 indicate that the convergence of the vorticity field is reasonably good up to about the third cycle. For DNS simulations, ensuring convergence for long runs is nearly impossible due to the computational constraints and the increasingly chaotic nature of the flow. In the work discussed in this section, mean quantities taken over 20 cycles were employed in order to obtain useful information regarding the hydrodynamics.

4.2   Verification that a quasi-steady state has been reached

To ensure that the flow has attained a steady state that is independent of the initial conditions, two different initializations of the flow forcing were implemented, and a determination was made of the cycles beyond which the near-bed horizontal velocities associated with both initializations nearly resemble each other. This step involved consideration of the R1-C4 case (asymmetric ripple and strongest flow), and it was assumed that all other cases (R0-C1, R0-C2, R0-C4, R1-C1, and R1-C2) will also attain a steady state if the R1-C4 case has attained it. The two flow forcing initializations are shown in Figure 4.1. The flow forcing C4p was obtained from C4 by applying the phase shift $-2\psi + \pi$ so that it starts at the beginning of the leftward flow.
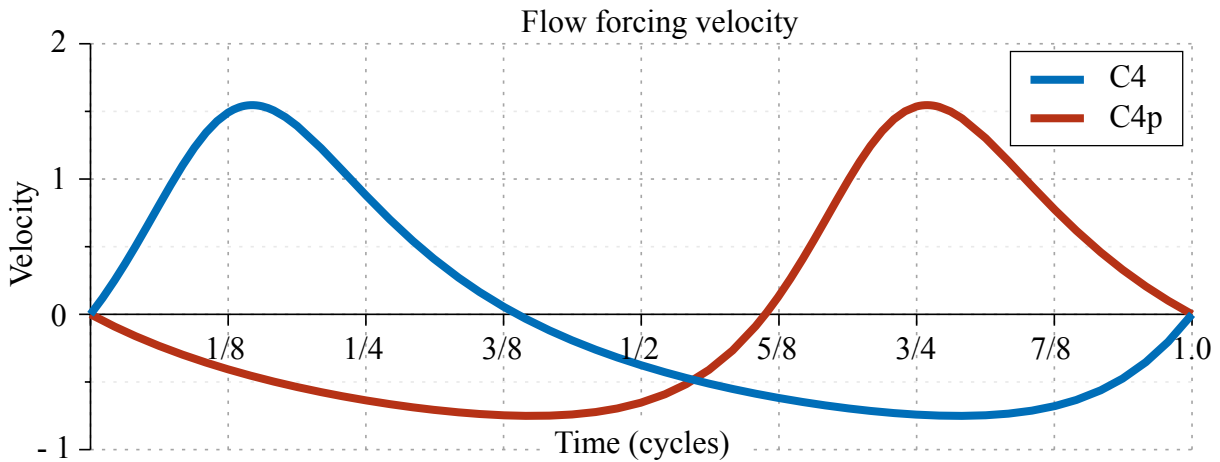
Figure 4.1: C4 and C4p flow forcings. C4p is identical to C4 but starts with the weaker, negative part of the flow forcing that precedes the stronger, positive part.

The simulation was run for 40 cycles, and the horizontal velocity was observed at a point $(0.05, -2.98)$ just above the bottom and to the right of the ripple crest. Figure 4.2 indicates the variations in the horizontal velocity during the first 40 cycles. It can be seen that the horizontal velocity attains a quasi-steady state after about 15 cycles. Figure 4.3 shows the same plot for cycles 20 to 23. Again, it is clear that the flows now resemble each other irrespective of the initializations.
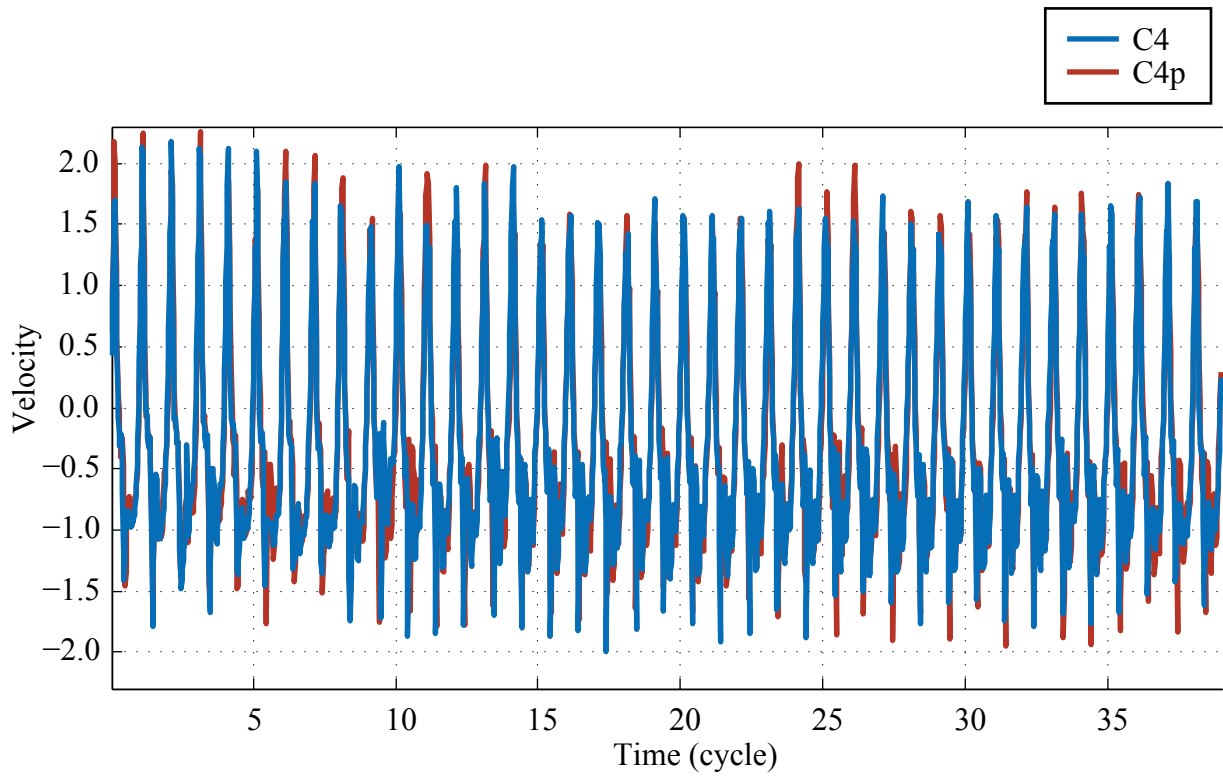
Figure 4.2: Variations in the horizontal velocity at point $(0.05, -2.98)$ during the first 40 cycles for the R1 ripple shape and the two different flow forcings, C4 and C4p. The C4p velocity plot has been shifted by $2\psi - \pi$ so that background currents are in phase.
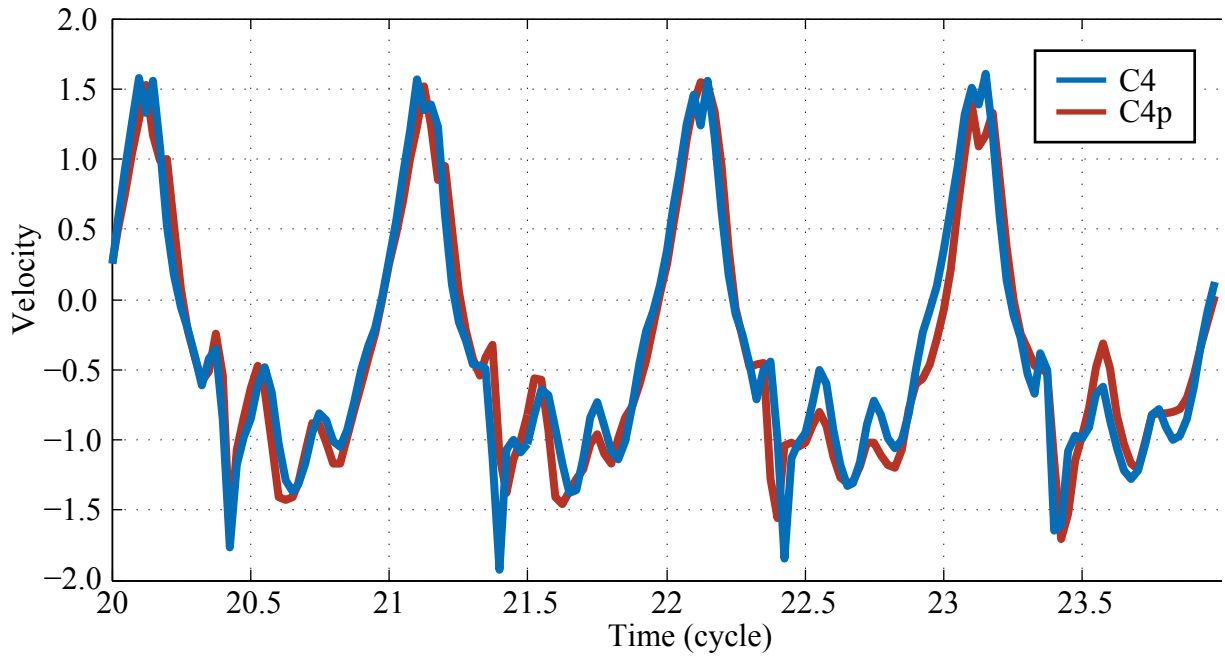
Figure 4.3: Variations in the horizontal velocity at point $(0.05, -2.98)$ during cycles 20 to 23 for the R1 ripple shape and the two different flow forcing initializations, C4 and C4p. The C4p velocity plot has been shifted by $2\psi - \pi$ so that the background currents are in phase.

4.3 Results and Discussion

We now focus on both the instantaneous and mean quantities related to vorticity, velocity, momentum, and viscous and pressure stress.

4.3.1 Vorticity

4.3.1.1 Instantaneous vorticity

The long-term instantaneous vorticity field is chaotic and difficult to characterize. For illustration purposes, this section provides examples of instantaneous vorticity fields in order to offer a glimpse of the underlying vortex structures that create a number of mean flow features discussed in this chapter.

Figures 4.4 and 4.5 show the vortex field at the 70th flow reversal, when the forcing flow changes direction from negative to positive, and at the 73rd flow reversal, when the forcing flow changes direction from positive to negative. These particular times were chosen so that clear, coherent vortex structures can be provided.

In these particular instances, the vorticity field is somewhat similar to the vorticity field that is evident a few time periods after the initiation of the simulation. The vortex structures near the ripple in the 70th flow reversal, illustrated in Figure 4.4, are similar to the vortex structures at the fourth and sixth reversals, as depicted in Figures 3.13 and 3.15. Two differences are that the vortices are stronger for the C1 flow forcing at the 70th flow reversal and that the vortex (red) looks stronger at the sixth reversal for R1-C1. Likewise, the vortex structures near the ripple in the 73rd flow reversal, depicted in Figure 4.5, are similar to the vortex structures at the third and fifth flow reversals, as evident in Figures 3.12 and 3.14. It should be noted that the vortices at the 73rd flow reversal are also stronger for the C1 forcing.

4.3.1.2 Mean vorticity

With respect to the mean vorticity field, this section demonstrates that (1) for the asymmetric flows, clockwise vorticity is relatively compact; (2) with more pronounced flow asymmetry, the counterclockwise vorticity becomes increasingly elongated horizontally as well as less compact; and (3) vorticity fields are largely insensitive to ripple asymmetry.

The near-periodic vortex structures in the quasi-steady state can be obtained by taking the mean of the vorticity fields during the last 20 cycles,

$$\bar{\omega}(x, z, t) = \frac{1}{20} \sum_{i=20}^{40-1} \omega\left(x, z, iT + t\right), \ t \in [0, T], \ x \in \left[0, \frac{4}{3}\right], \ z \in [-3.2, 0]$$

and are shown in Figures 4.6 and 4.7. It should be noted that, in these figures, $\Delta\omega = 2.25$ was used for visual clarity, since the mean vortex field is weaker, especially during the transition from a negative to a positive flow.

During the flow reversal from negative to positive, as indicated in Figure 4.6, the mean vorticity fields are similar in strength in all cases but are more compact for the C1 forcing. Elongated vortex-like structures can be observed for the C2 and C4 cases. On the other hand, during the flow reversal from positive to negative, as shown in Figure 4.7, the R1 ripple and the C2 and C4 asymmetric forcings generate increasingly stronger mean vorticity fields. For the C2 and C4 flow forcings, the presence of a larger but weaker clockwise vortex, a remnant of the previously formed vortex, is also a notable distinction not evident in either the C1 case or in any other cases during the first three cycles.

The clockwise and counterclockwise vorticity fields were then averaged separately for the last 20 cycles using

$$\bar{\omega}_{\text{clockwise}}(x, z) = \frac{1}{20T} \sum_{t=20T}^{40T} \omega_{\text{clockwise}}\left(x, z, t\right), \ x \in \left[0, \frac{4}{3}\right], \ z \in [-3.2, 0]$$

and using a similar expression for counterclockwise vorticity. Figure 4.8 displays the mean vorticity fields for the clockwise and counterclockwise vorticity fields. As expected, the average clockwise vorticity is strongest and most compact for C4, followed by those for C2 and C1. However, the average counterclockwise vorticity becomes stronger and less compact as the flow asymmetry increases, although the reverse flow forcing becomes weaker as the asymmetry of the flow increases. No notable difference is evident between the two ripple shapes, with the exception of the symmetric C1 forcing, for which the mean vorticity field is slightly stronger and less compact for the R1 ripple.
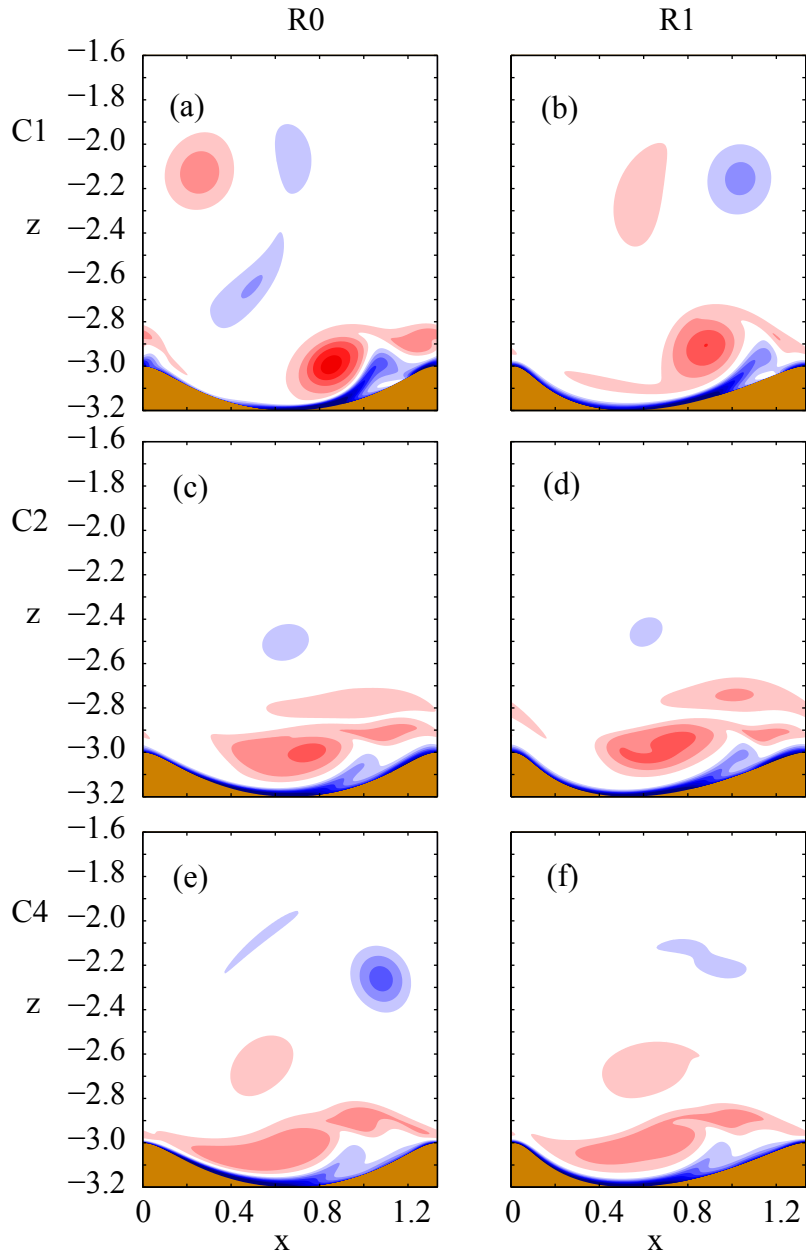
Figure 4.4: Instantaneous vorticity at the 70th flow reversal for all six base cases. Vorticity for ripple shapes R0 and R1 are shown in (a, c, e) and (b, e, f), respectively. Vorticity for flow forcings C1, C2, and C4 are shown in (a, b), (c, d), and (e, f), respectively. Vorticity contours $\Delta \omega = 3.75$. Clockwise (counterclockwise) vorticity is indicated by blue (red) colors.
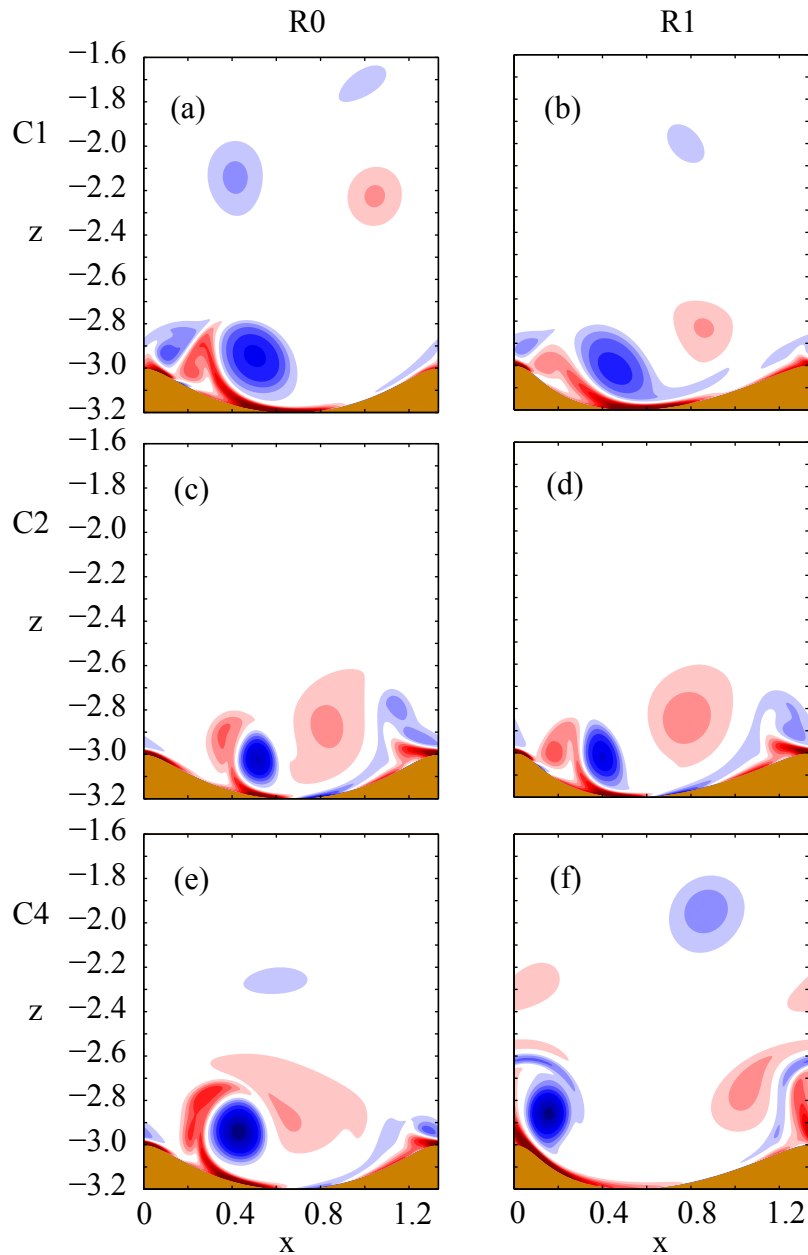
Figure 4.5: Instantaneous vorticity at the 73th flow reversal for all six base cases. Vorticity for ripple shapes R0 and R1 are shown in (a, c, e) and (b, e, f), respectively. Vorticity for flow forcings C1, C2, and C4 are shown in (a, b), (c, d), and (e, f), respectively. Vorticity contours $\Delta\omega = 3.75$. Clockwise (counterclockwise) vorticity is indicated by blue (red) colors.
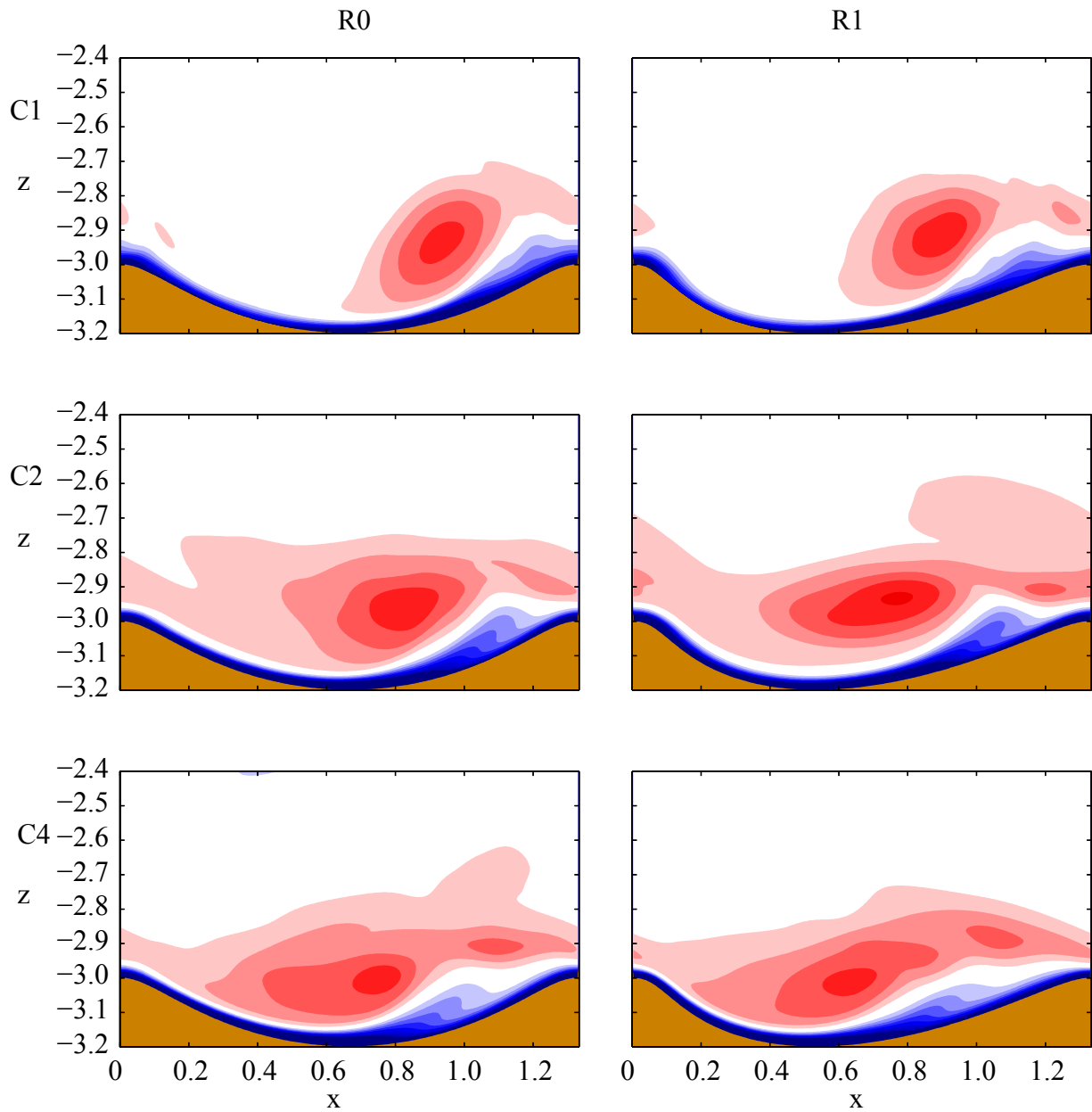
Figure 4.6: Mean vorticity during cycles 20 to 40 at the point of flow reversal (negative to positive) for all six base cases. Vorticity contours $\Delta\omega = 2.25$. Clockwise (counterclockwise) vorticity is indicated by blue (red) colors.
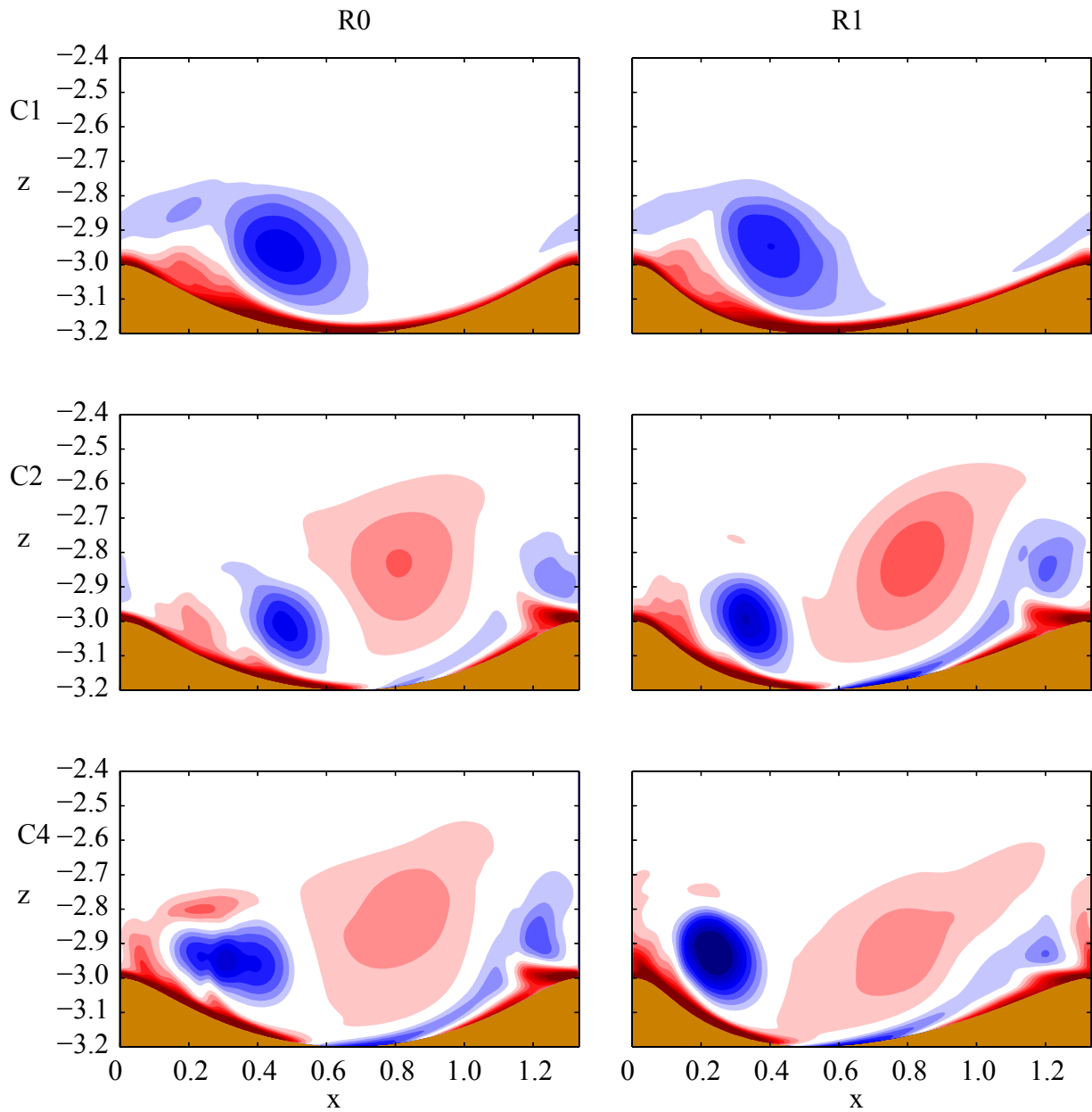
Figure 4.7: Mean vorticity during cycles 20 to 40 at the point of flow reversal (positive to negative) for all six base cases. Vorticity contours $\Delta\omega = 2.25$. Clockwise (counterclockwise) vorticity is indicated by blue (red) colors.
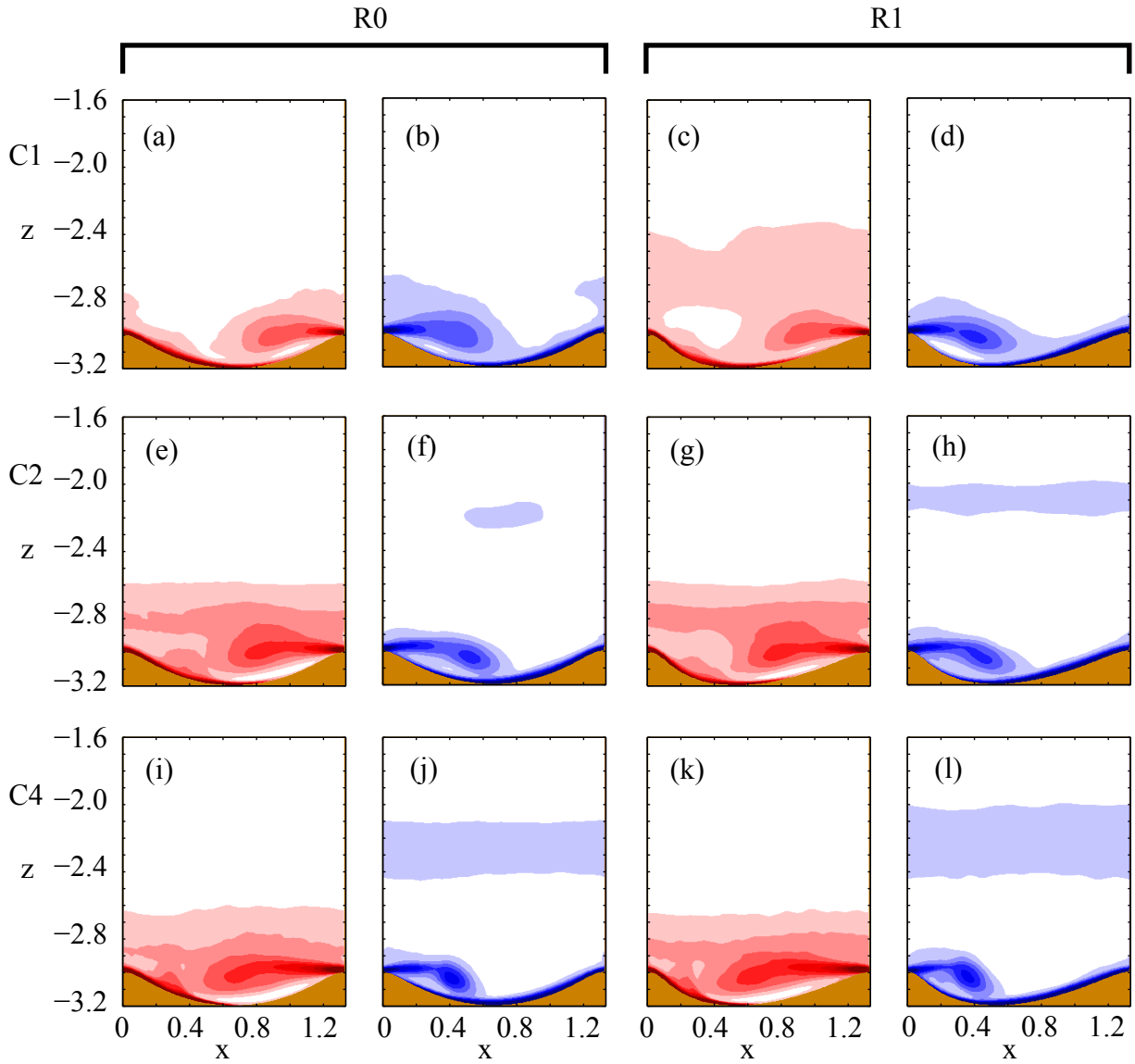
Figure 4.8: Mean clockwise and counterclockwise vorticity over cycles 20 to 40 for all six base cases. Vorticity is shown for the flow forcings (a)-(d) C1, (e)-(h) C2, and (i)-(l) C4. Counterclockwise and clockwise vorticity for the R0 ripple shape is shown in (a, e, i) and (b, f, j), respectively. Counterclockwise and clockwise vorticity for the R1 ripple shape is shown in (c, g, k) and (d, h, l), respectively. Vorticity contours $\Delta\omega = 3.75$. Clockwise (counterclockwise) vorticity is indicated by blue (red) colors.

4.3.2   Velocity distribution

4.3.2.1   Instantaneous velocity

Figure 4.9 shows the variations in the fluctuating horizontal velocity measured along a vertical line extending from the ripple trough during the first 40 cycles for all six base cases. The fluctuating horizontal velocity was obtained by removing the flow forcing component from the horizontal velocity measurements.

In the case of the asymmetric ripple and flow forcings, it can be observed that a band of negative velocity is eventually established just above the ripple crest. This unidirectional negative current develops more quickly and is stronger for the asymmetric ripple and asymmetric flow forcings.

4.3.2.2   Mean velocity

This section shows that (1) for the asymmetric flows and the asymmetric ripple, a band of mean negative flow is established above the ripple; (2) the strength of the mean negative flow is stronger for the asymmetric ripple and becomes greater with increasing flow asymmetry; and (3) for the two asymmetric flows, the band of negative mean flow is closer to the ripple.

Figure 4.10 indicates the mean horizontal velocity during the last 20 cycles for all six base cases. The unidirectional flow is clearly visible for the asymmetric ripple and flow forcings. It should be noted that this flow is stronger for the asymmetric ripple and becomes increasingly stronger for the asymmetric flow forcings. No preferred direction and no mean current are evident for the R0-C1 case, in contrast to all other cases, which feature a particular direction due to the asymmetries.

Figure 4.11 provides a similar diagram but for the R1 and R1f ripples. The shape of the R1f ripple is identical to that of R1 but with the profile flipped horizontally so that the left side of the crest is steeper than the right side. For these cases of asymmetric oscillatory flow forcings, with the stronger forward and weaker backward flows, R1f ripple configuration is rather artificial, not found nature (Testik *et al.* , 2006), and we consider it only for academic interest here to investigate the effect to the mean-flow of flipping the ripple. It should be noted that the mean flow reverses direction for the R1f-C1 case, as indicated in Figure 4.11(b), although the mean currents near the boundary remain unchanged with respect to direction. For the asymmetric currents, as the asymmetry of the flow forcing increases, the direction of the mean velocity remains unchanged, but differences are evident
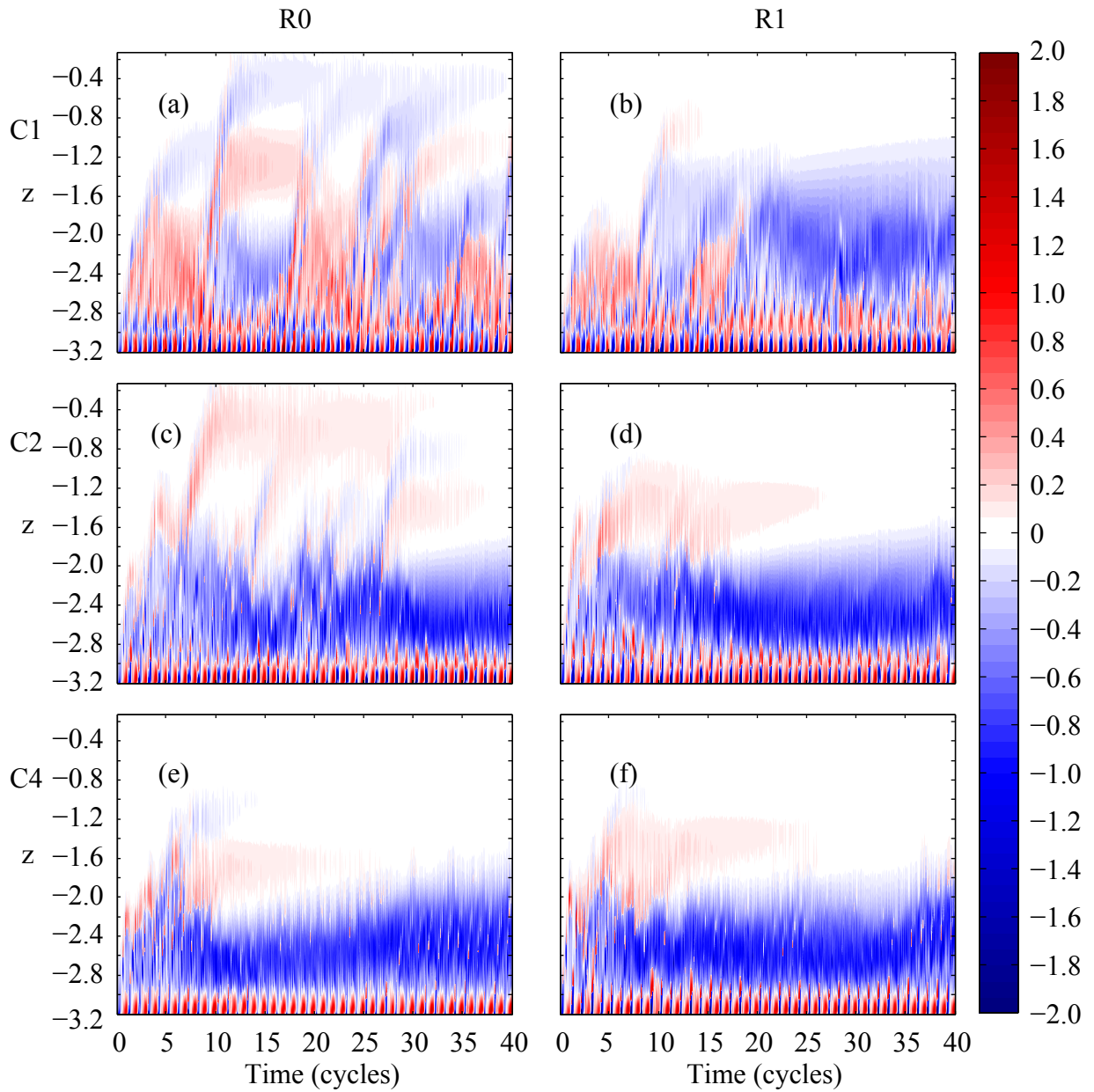
Figure 4.9: Variations in the fluctuating horizontal velocity measured at the ripple trough during the first 40 cycles for all six base cases. Velocities for ripple shapes R0 and R1 are shown in (a, c, e) and (b, d, f), respectively. Velocities for flow forcings C1, C2, and C4 are shown in (a, b), (c, d), and (e, f), respectively.

in the thickness and strength of the layers of the mean flow. In all cases, including when the ripple is flipped, the near-bottom flow is towards the crest on both sides of the crest.

Figure 4.12 displays the vertical distribution of the mean current at the crest and at the trough during the last 20 cycles. As long as the flow forcing is asymmetric, the maximum mean current is observably insensitive to the degree of flow asymmetry. Furthermore, the mean current is strong - about 80% of the peak current in the oscillating flow. A slight increase in the maximum mean velocity is evident for the asymmetric ripple shape with the C4 flow forcing compared with that for the C2 forcing. As previously noted, the vertical distribution of the velocity becomes more compact as the asymmetry of the flow forcing increases. For case R0-C1, the mean current is nearly zero at its crest and trough, whereas it is slightly negative for the R1-C1 case. Except for the R1-C1 case, the mean current can be seen to be centered around a horizontal line at a height of 0.4 above the ripple crest ($z = -2.6$), whereas it is higher up, at a height of about 1.2 above the ripple crest ($z = -1.8$) for the R1-C1 case.

The next step was to consider the velocity profile near the bottom boundary. Figure 4.13 shows the mean current within a distance of 0.2 from the bottom during the last 20 cycles at positions (a) $x = 0$, (b) $x = 0.53$ (trough in R1), and (c) $x = 0.66$ (trough in R0). The mean taken across the entire ripple ($x = 0$ to $x = 1.33$, $\delta = 0.2$) is indicated in (d). As can be seen in 4.13(a), at the crest, a negative velocity is evident near the boundary and becomes stronger as the asymmetry of the forcing velocity increases. The R1 ripple produces a slightly stronger current around $\delta = 0.02$. The mean velocity across the entire ripple indicates that a positive current exists near the bottom, which becomes stronger as the asymmetry of the flow forcing increases and also when the asymmetry of the ripple shape increases from R0 to R1.

4.3.3   Momentum fluxes

Momentum fluxes play an important role in changing the momentum of a system. As observed earlier, asymmetric ripples and flow forcings generate a mean flow above the ripple crest. There are a number of ways of analysing such flows.

Wave-current flows can be analyzed by using the triple decomposition $u(x, z, t) = u_c(x, z) + u_p(x, z, \theta) + u'(x, z, t)$, where $u_c(x, z)$ is the time-averaged mean current, $u_p(x, z, \theta)$ is the phase-averaged flow, as function of the phase θ, and $u'(x, z, t)$ is the fluctuating velocity (Thais & Magnaudet, 1995). This decomposition allows the analysis of radiation and Reynolds stresses that contribute to the establishment of mean flows.
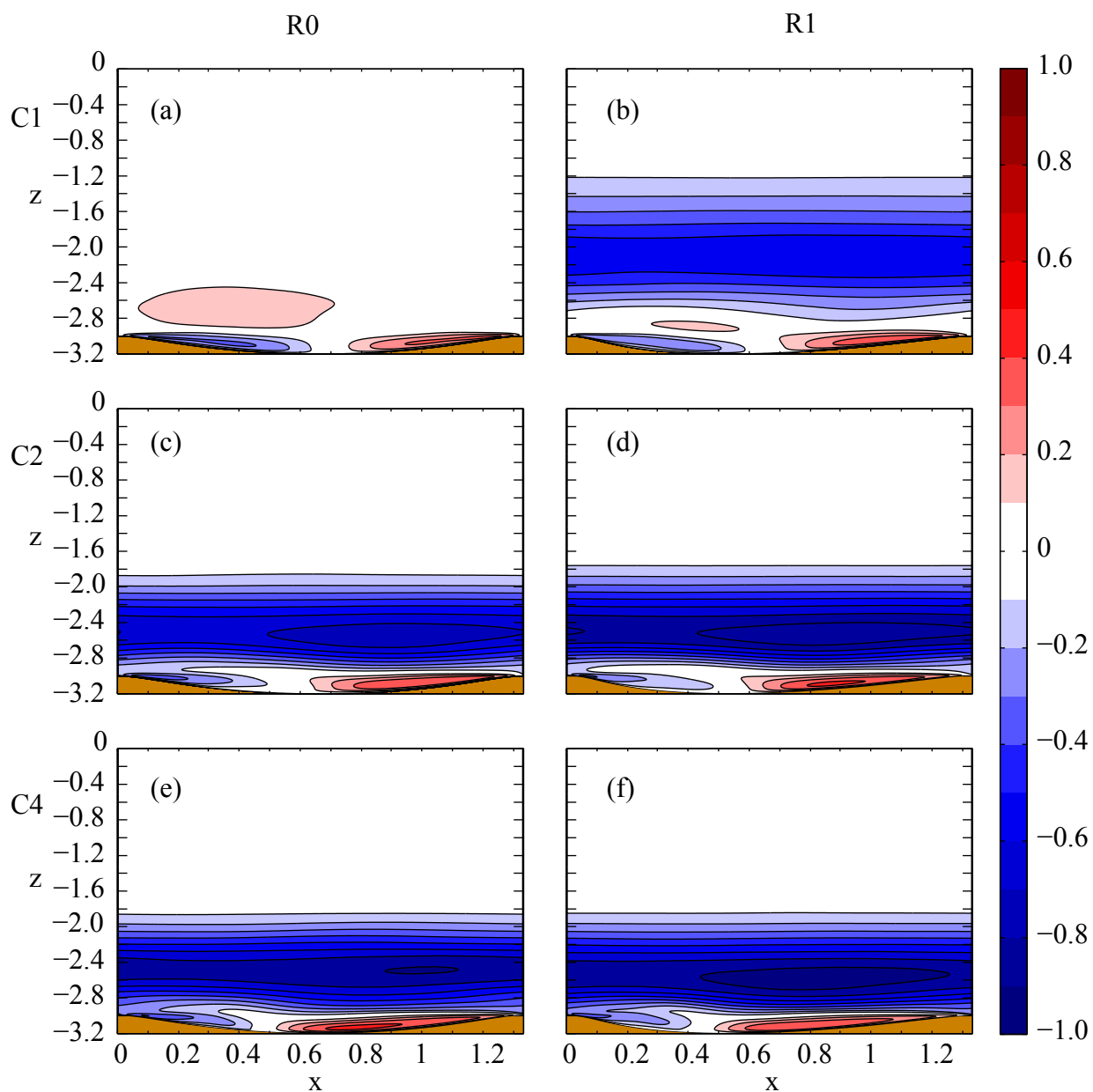
Figure 4.10: Mean horizontal velocity during the last 20 cycles for all six base cases. Velocities for ripple shapes R0 and R1 are shown in (a, c, e) and (b, d, f), respectively. Velocities for flow forcings C1, C2, and C4 are shown in (a, b), (c, d), and (e, f), respectively.
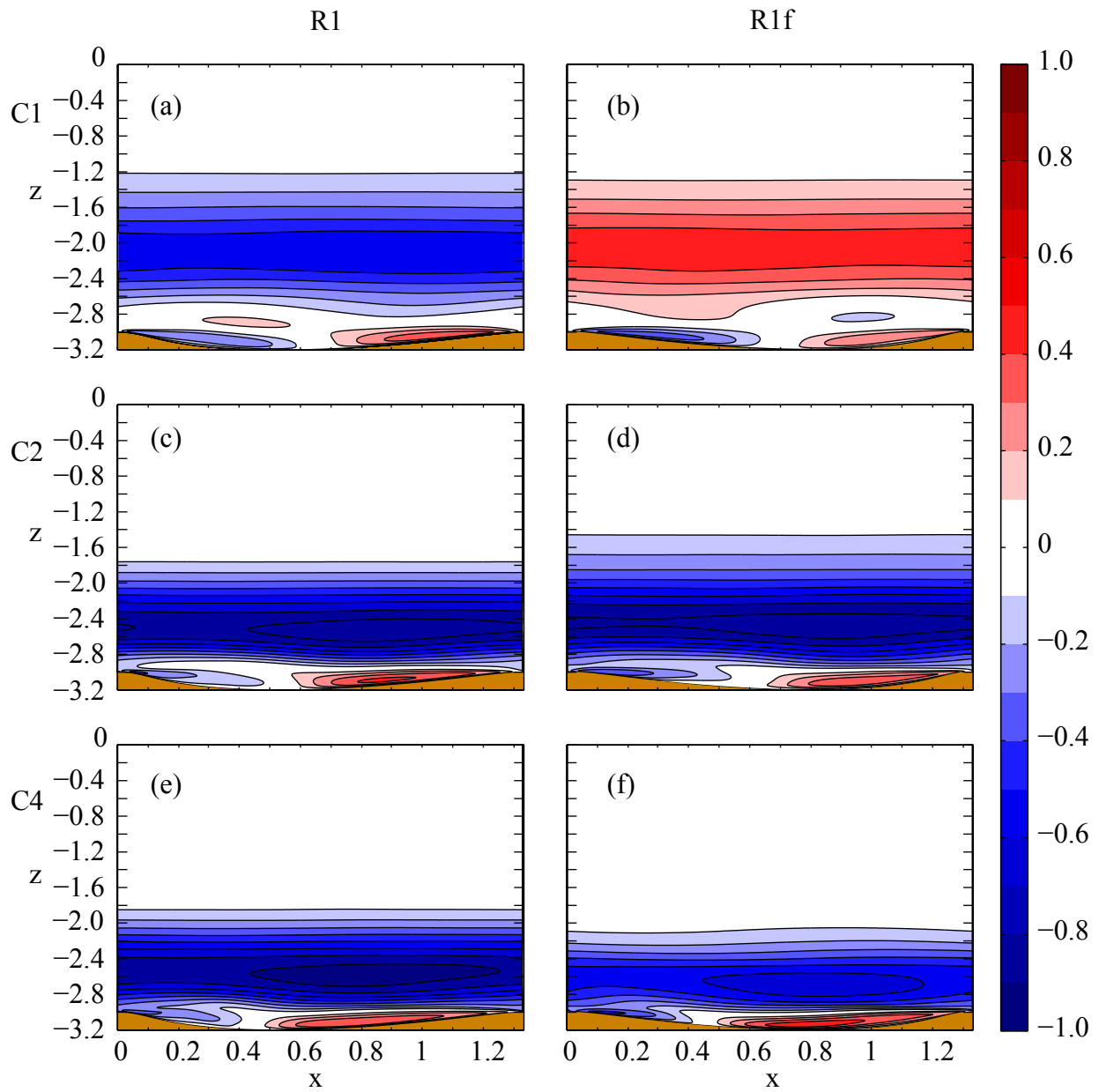
Figure 4.11: Mean horizontal velocity during the last 20 cycles for the R1 and R1f ripple shapes and C1, C2, and C4 flow forcings. Velocities for ripple shapes R0 and R1 are shown in (a, c, e) and (b, d, f), respectively. Velocities for flow forcings C1, C2, and C4 are shown in (a, b), (c, d), and (e, f), respectively.
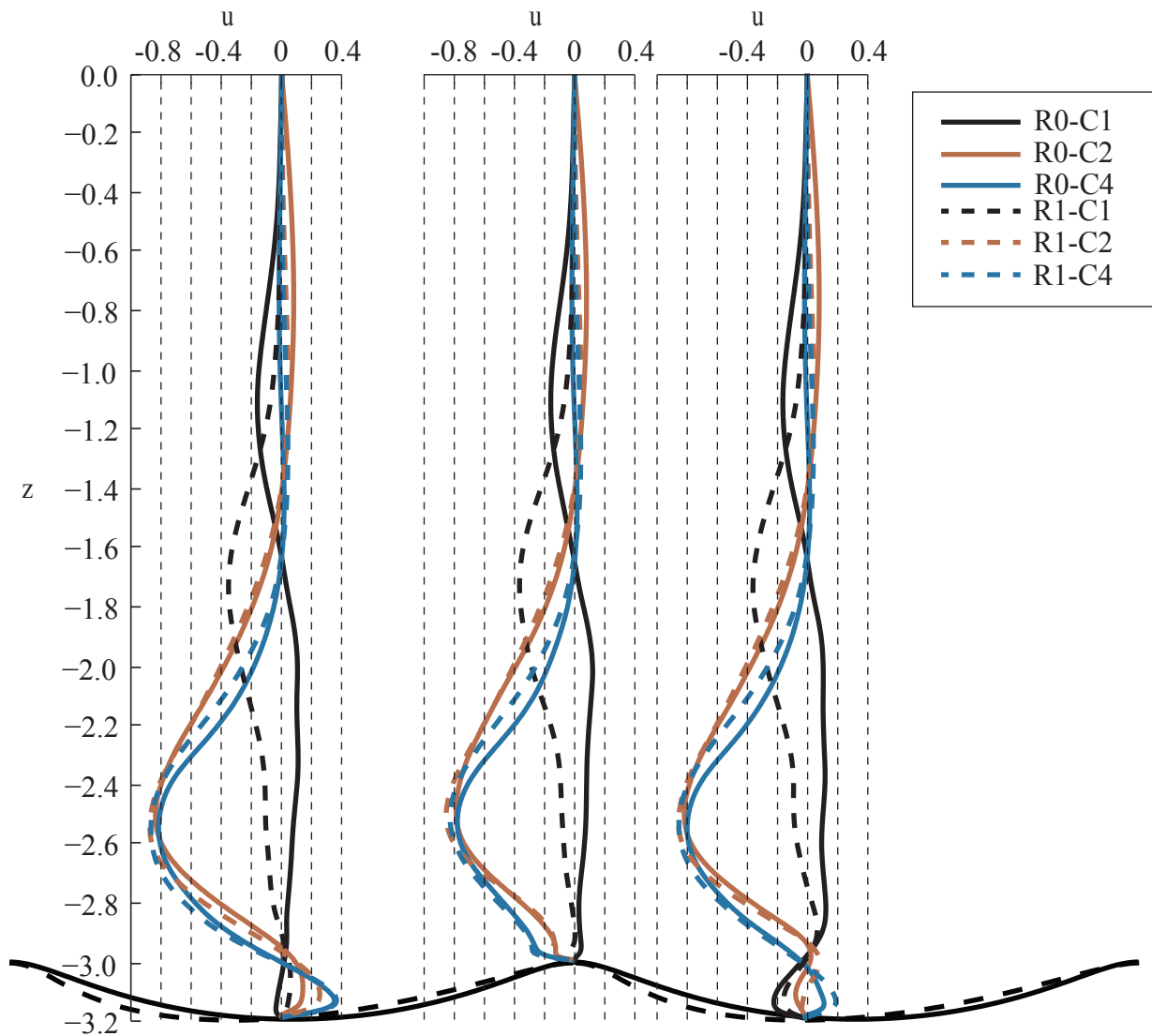
Figure 4.12: Vertical distribution of the mean horizontal velocity at the crest and at the trough during the last 20 cycles for all six base cases.

79
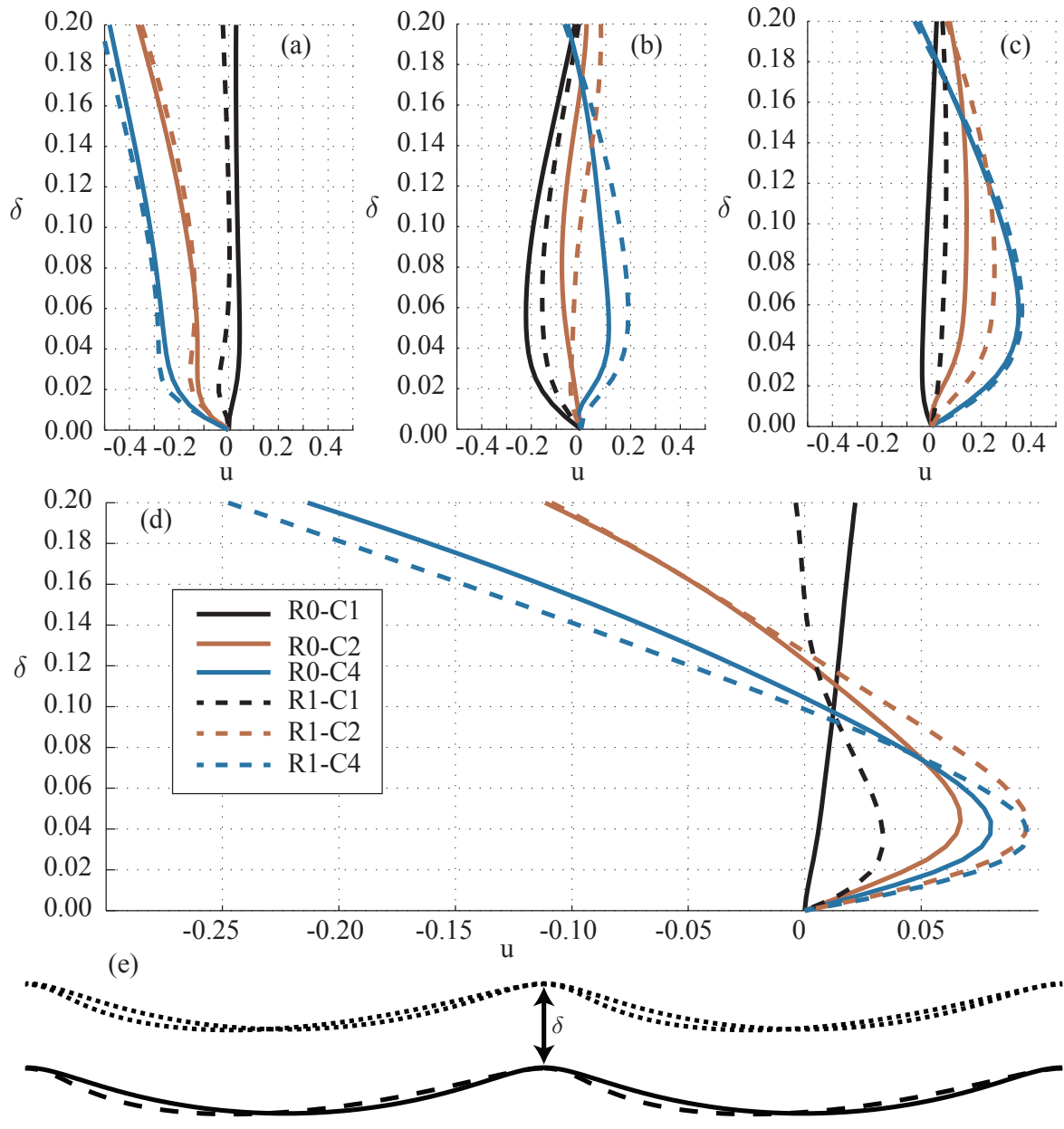
Figure 4.13: Vertical distribution of the mean horizontal velocity at the crest and at the trough near the boundary during the last 20 cycles for all six base cases. Velocity is measured at (a) $x = 0$ (crest), (b) $x = 0.53$ (trough in R1), and (c) $x = 0.66$ (trough in R0). The mean across the entire ripple ($x = 0$ to $x = 1.33$) is shown in (d). Mean currents are plotted as a function of height above the bottom δ, which is illustrated in (e).

80

Wave-current flows can also be analyzed considering momentum and its advective, viscous stress, and pressure contributions at various parts of the flow. This is the methodology we use in this section in order to acquire an understanding of the origin of these mean flows.

Integrating the governing equations,

$$u_t + \nabla \cdot (\vec{u}u) = -p_x + \frac{1}{Re}\nabla^2 u + F_b \tag{4.1}$$

$$w_t + \nabla \cdot (\vec{u}w) = -p_z + \frac{1}{Re}\nabla^2 w \tag{4.2}$$

over the domain gives

$$\frac{d}{dt}\iint_V u\,dxdz = -\iint_V \nabla \cdot (p,0)\,dxdz + \frac{1}{Re}\iint_V \nabla \cdot \nabla u\,dxdz + \iint_V F_b\,dxdz$$

$$= -\oint_{\partial V} (p,0)\cdot\hat{n}\,ds + \frac{1}{Re}\oint_{\partial V}\nabla u \cdot \hat{n}\,ds + \iint_V F_b\,dxdz \tag{4.3}$$

$$\overbrace{\frac{d}{dt}\iint_V w\,dxdz}^{M'_{z,V}} = -\iint_V \nabla \cdot (0,p)\,dxdz + \frac{1}{Re}\iint_V \nabla \cdot \nabla w\,dxdz$$

$$= \underbrace{-\oint_{\partial V} (0,p)\cdot\hat{n}\,ds + \frac{1}{Re}\oint_{\partial V}\nabla w \cdot \hat{n}\,ds}_{M'_{z,\partial V}} \tag{4.4}$$

since the no-slip top and bottom boundary conditions prevent the advective terms from making a contribution to the momentum flux. The x-momentum equation can now be rearranged in order to obtain the perturbed quantities. In terms of the forcing velocity, $u_F(t)$,

$$F_b(t) = \frac{du_F(t)}{dt}$$

Therefore, (4.3) can be written as

$$\underbrace{\frac{d}{dt}\iint_V (u - u_F)\,dxdz}_{M'_{x,V}} = \underbrace{\overbrace{-\oint_{\partial V} (p,0)\cdot\hat{n}\,ds}^{M'_{x,\partial V,p}} + \overbrace{\frac{1}{Re}\oint_{\partial V}\nabla u \cdot \hat{n}\,ds}^{M'_{x,\partial V,\mu}}}_{M'_{x,\partial V}} \tag{4.5}$$

Integrating with respect to time gives

$$\underbrace{\iint_V (u - u_F) \, dxdz}_{M_{x,V}} = \overbrace{\int_0^t \oint_{\partial V} (p,0) \cdot (-\hat{n}) \, ds \, dt}^{M_{x,\partial V,p}} + \overbrace{\frac{1}{Re} \int_0^t \oint_{\partial V} \nabla u \cdot \hat{n} \, ds \, dt}^{M_{x,\partial V,\mu}} \qquad (4.6)$$

$$\underbrace{}_{M_{x,\partial V}}$$

$$= \int_0^t \oint_{\partial V} \underbrace{(p,0) \cdot (-\hat{n})}_{F_{x,\,p}} \, ds \, dt + \int_0^t \oint_{\partial V} \underbrace{\frac{1}{Re} \nabla u \cdot \hat{n}}_{F_{x,\,\mu}} \, ds \, dt \qquad (4.7)$$

Similarly, for the momentum in the z-direction,

$$\underbrace{\iint_V w \, dxdz}_{M_{z,V}} = \underbrace{\int_0^t \oint_{\partial V} (0,p) \cdot (-\hat{n}) \, ds \, dt + \frac{1}{Re} \int_0^t \oint_{\partial V} \nabla w \cdot \hat{n} \, ds \, dt}_{M_{z,\partial V}} \qquad (4.8)$$

$$= \int_0^t \oint_{\partial V} \underbrace{(0,p) \cdot (-\hat{n})}_{F_{z,\,p}} \, ds \, dt + \int_0^t \oint_{\partial V} \underbrace{\frac{1}{Re} \nabla w \cdot \hat{n}}_{F_{z,\,\mu}} \, ds \, dt \qquad (4.9)$$

We will refer to this "perturbation" x-momentum (4.6) as the x-momentum for simplicity. It should be noted that, since the top boundary is horizontally flat, the x-momentum flux contribution from the pressure term there is zero, based on $(p,0) \cdot \hat{n} = 0$. The above expressions can now be further decomposed, and the boundary of the domain, ∂V, can be divided into four parts, Γ_r, Γ_t, Γ_l, and Γ_b to refer to the right, top, left, and bottom boundaries, respectively. For simplicity, a function $f(s,t)$ and its contour integral over ∂V can be considered. Then,

$$\oint_{\partial V} f(s,t)ds = \int_{\Gamma_t + \Gamma_b + \Gamma_l + \Gamma_r} f(s,t)ds \qquad (4.10)$$

$$= \int_{\Gamma_t} f(s,t)ds + \int_{\Gamma_b} f(s,t)ds \qquad (4.11)$$

since $\int_{\Gamma_l} f(s,t)ds = - \int_{\Gamma_r} f(s,t)ds$ because the flow is periodic in the x-direction. Based on consideration of this decomposition, the letter t or b can be appended to the subscript of each of the above terms to refer to their top and bottom contributions, respectively.

Based on known theory, $M_{z,V} = 0$. In the simulations for this work, $|M_{z,V}| \leq 4 \times 10^{-4}$ at all times. Figure 4.14(a) shows the decomposition of the rate of change in z-momentum

$(M'_{z,\partial V,\mu}$, red; $M'_{z,\partial V,p}$, blue). It can be seen that they balance each other so that $M'_{z,\partial V} = 0$, as confirmed by Figure 4.14(c), which indicates that the z-momentum remains unchanged. A comparison with the flow forcing depicted in Figure 4.14(d) reveals that the fluctuating x-momentum is most negative when the flow forcing is at a maximum and vice versa.

To ensure that the C1, C2, and C4 flow forcings in the present study have no inherent mean current associated with them, which could occur through significant rounding or approximation errors, a number of experiments were conducted with these forcing but with a flat bottom. Figure 4.15 shows that the C1, C2, and C4 forcings do not create any mean currents. With respect to this flat-bottom boundary, it should be noted that the x-momentum flux contribution from the pressure term is zero since $(p, 0) \cdot \hat{n} = 0$. Two further tests were carried out, this time for the R0 and R1 bottom profiles with a perturbed initialization. The perturbation employed was the C1 current but restricted to the first cycle. Figures 4.15(d,e) indicate the resulting momentum. It can be seen that the momentum eventually reaches zero, as expected. All of the figures indicate that during the forward (positive) flow forcing, a decrease in the momentum anomaly, (4.6), is evident, whilst during the backward (negative) flow forcing, the momentum anomaly increases. This effect occurs because the momentum anomaly is the momentum of the flow forcing minus the momentum of the background current without the boundary layers and, for example, during forward flow, there is a momentum deficit in the bottom boundary layer.

4.3.3.1 Effect of asymmetries on the mean current

This section explains how the R0-C1 case differs from the other cases. For the R0-C1 case, the x-momentum oscillates at a low frequency caused by slow oscillations in $M_{x,\partial V,p}$. For the asymmetric flows, (1) the x-momentum is more negative for the asymmetric ripple and with increasing flow asymmetry; (2) the negative x-momentum is initially caused by the negativity of $M_{x,\partial V,p}$; and (3) during later time periods, $M_{x,\partial V,\mu}$ also becomes negative and balances the negativity of $M_{x,\partial V,p}$, thus preventing further decreases in the x-momentum.

EFFECT ON THE MEAN CURRENT DUE TO THE FLOW ASYMMETRY

Figure 4.16 illustrates the momentum for the R0-C1 case. Fast oscillations in step with the frequency of the flow forcing are evident, along with oscillations with longer periods of about 10 to 15 flow forcing periods, which we call subharmonic oscillations. These are discussed further in Section 4.3.4.2. As indicated in Figure 4.16(a), the subharmonic oscillations in the momentum of the system are due to the oscillation of $M_{x,\partial V,p}$. This effect is attributable to the momentum flux fluctuations at the bottom boundary since the mean
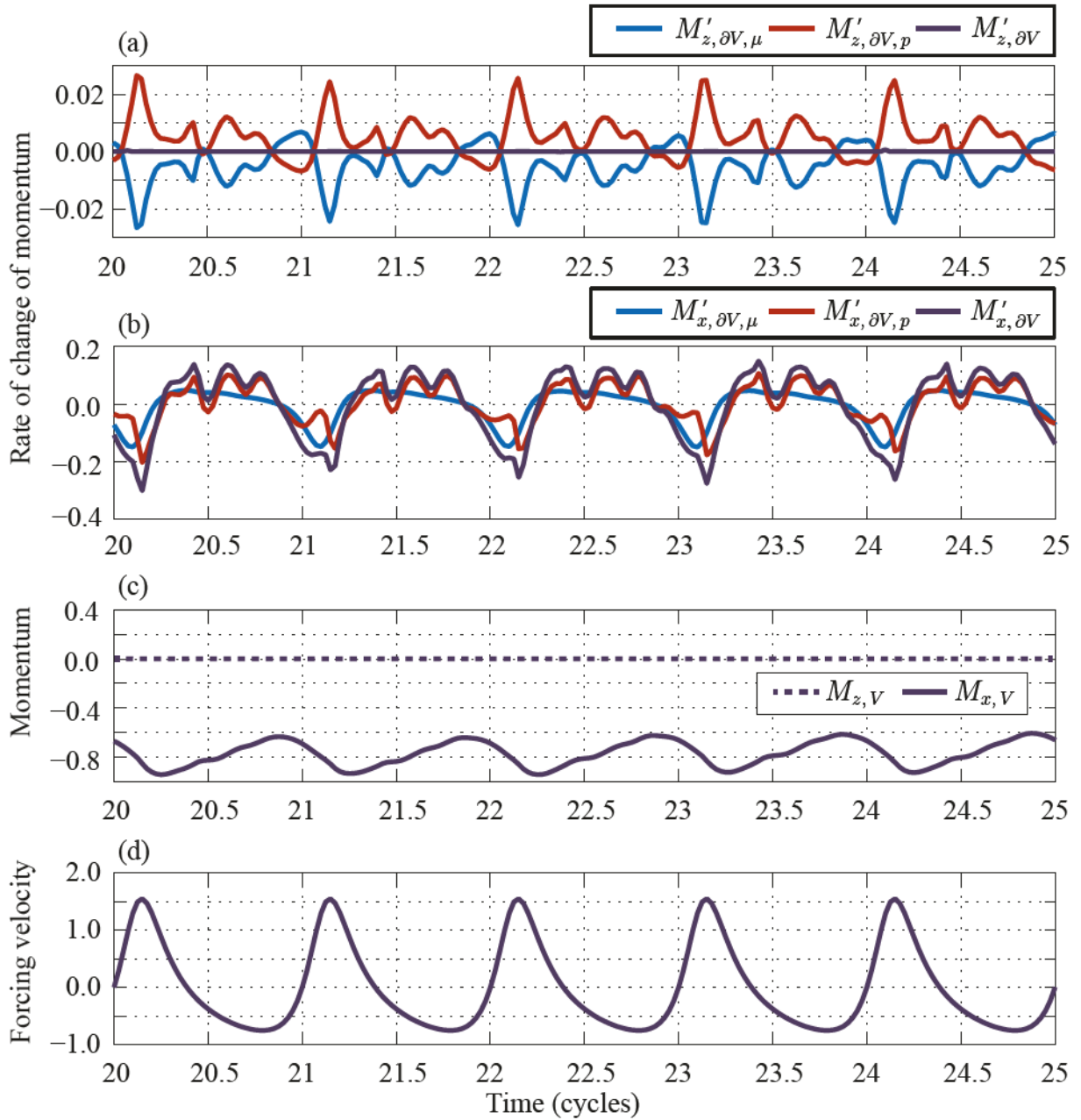
Figure 4.14: For the R1-C4 case during cycles 20-25, instantaneous rate of change in (a) the z-momentum and (b) the x-momentum due to viscous stress ($M'_{x,\partial V,\mu}$, blue), and pressure ($M'_{x,\partial V,p}$, red), along with their totals ($M'_{x,\partial V}$, purple). Also indicated are (c) the momentum in the x and z directions ($M_{x,V}, M_{z,V}$) and (d) the flow forcing (u_F).

84
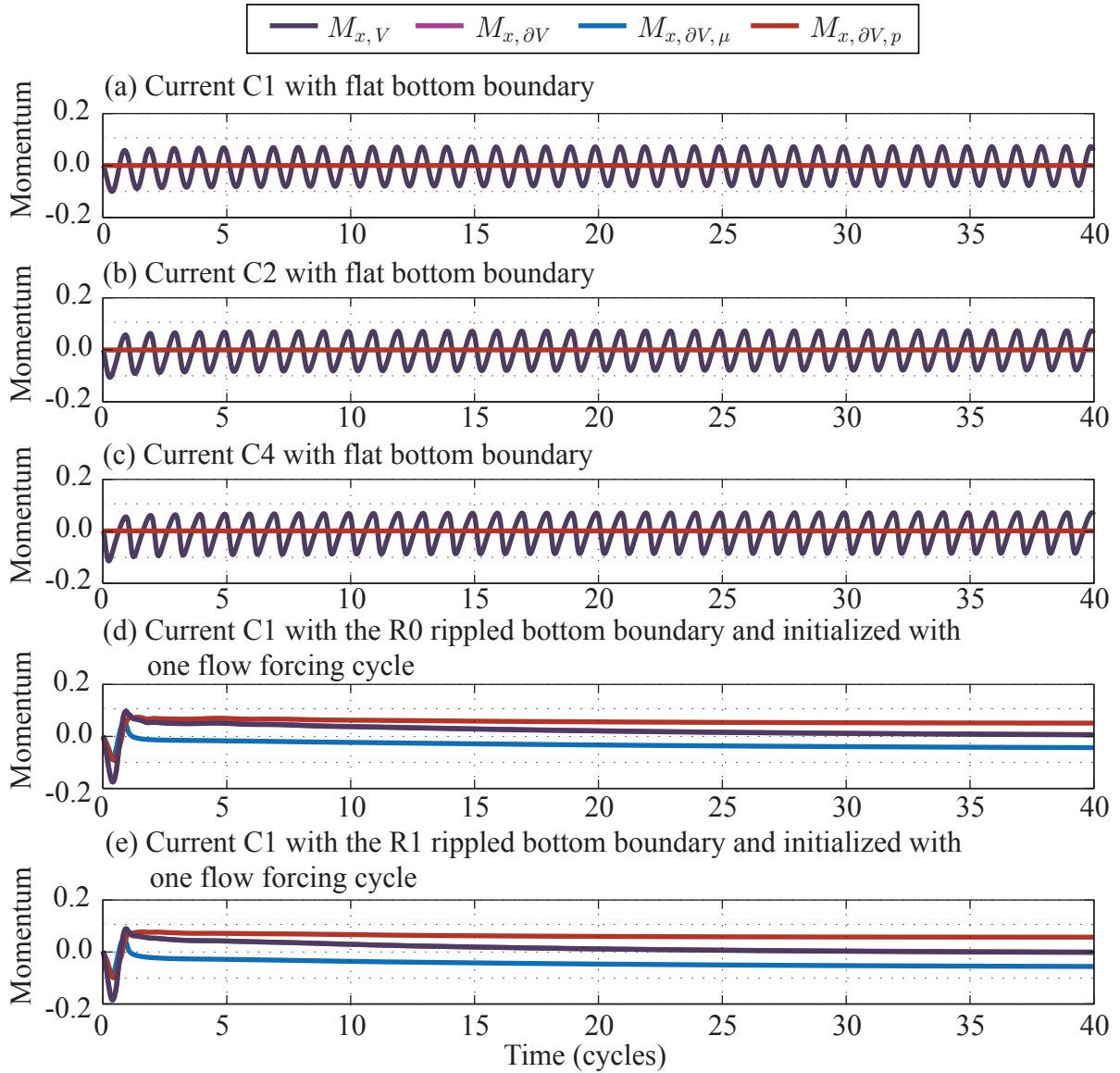
Figure 4.15: Momentum ($M_{x,V}$, purple; $M_{x,\partial V}$, magenta) and its constituent viscous stress ($M_{x,\partial V,\mu}$, blue) and pressure ($M_{x,\partial V,p}$, red) contributions for (a)-(c) the case of a flat-bottom boundary with flow forcings (a) C1, (b) C2, and (c) C4. Similar curves for the (d) R0-C1 and (e) R1-C1 cases but with the flow forcing applied for only a single cycle. In (a)-(c), all curves $M_{x,V}$, $M_{x,\partial V}$, and $M_{x,\partial V,\mu}$ overlap. In (d) and (e), curves $M_{x,V}$ and $M_{x,\partial V}$ overlap.

momentum contribution from the top boundary is relatively small (Figure 4.16(b)). The variations in $M_{x,\partial V,p}$ are therefore the factor that tracks the variations in total momentum, $M_{x,\partial V}$. This discovery of a subharmonic oscillatory mean flow associated with a perfectly symmetric system was unexpected.

Figure 4.17 shows the momentum for the R0-C2 case. As can be seen in Figure 4.17(a), the period-averaged momentum at first decreases due to a reduction in $M_{x,\partial V,p}$. Then, after about 10 cycles, a consistent decrease in $M_{x,\partial V,\mu}$ becomes evident. After about 25 cycles, $M_{x,\partial V,p}$ starts to increase, thus rendering the momentum of the system somewhat steady. Since the graphs represent integrals of the stress terms, this means the stress exerted by the viscous and pressure terms are approximately equal and opposite. Again, as indicated in Figure 4.17(b), the momentum contributed by the fluxes at the top boundary is relatively small.

Figure 4.18 depicts the momentum for the R0-C4 case. As can be seen in Figure 4.18(a), the same general trend observed for the case R0-C2 case is apparent, but $M_{x,\partial V,\mu}$ now decreases consistently from the beginning. $M_{x,\partial V,p}$ diminishes until about seven cycles, when it begins to increase. Around 25 cycles, the rise in $M_{x,\partial V,p}$ increases quickly enough to balance the decrease contributed by $M_{x,\partial V,\mu}$, thus, again, steadying the momentum. Figure 4.18(b) shows that, as with the previous case, no contribution to this momentum stems from the top boundary.

EFFECT ON THE MEAN FLOW FIELD DUE TO THE RIPPLE ASYMMETRY.

Figure 4.19 illustrates the momentum for the R1-C1 and R1f-C1 cases. As previously mentioned, R1f is simply the R1 ripple flipped horizontally. The diagram does not show the evolution of the momentum for the R1f-C1 case for the full 40 cycles.

As indicated in Figure 4.19(a), for the R1-C1 case, the momentum first increases, and then undergoes a few oscillatory increases and decreases before attaining some degree of stationarity. This oscillatory nature of the mean flow is caused almost entirely by $M_{x,\partial V,p}$. $M_{x,\partial V,\mu}$ decreases consistently. When the ripple profile is flipped, the momentum exhibits a consistent increase due to the momentum contributed by both $M_{x,\partial V,p}$ and $M_{x,\partial V,\mu}$. Figure 4.19(b) shows that all net momentum contributions again originate at the bottom boundary.

To summarize, R1-C1 results in a negative momentum and R1f-C1 produces a positive momentum.
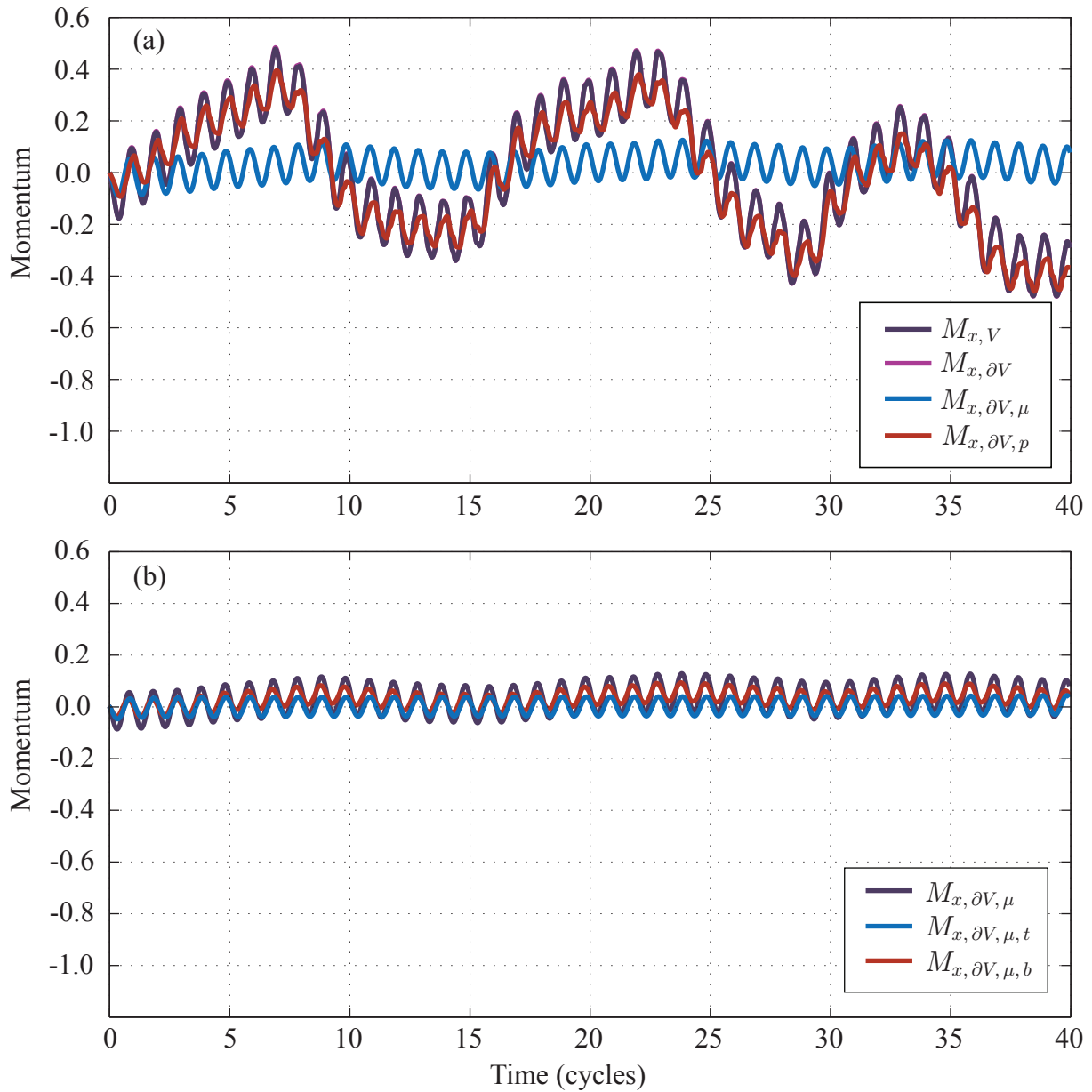
Figure 4.16: For the R0-C1 case, (a) the x-momentum ($M_{x,V}$, purple; $M_{x,\partial V}$, magenta; they overlap each other) and its constituent viscous stress ($M_{x,\partial V,\mu}$, blue) and pressure ($M_{x,\partial V,p}$, red) contributions, and (b) the viscous stress ($M_{x,\partial V,\mu}$, purple) and its contributions from the top (blue) and bottom (red) boundaries.
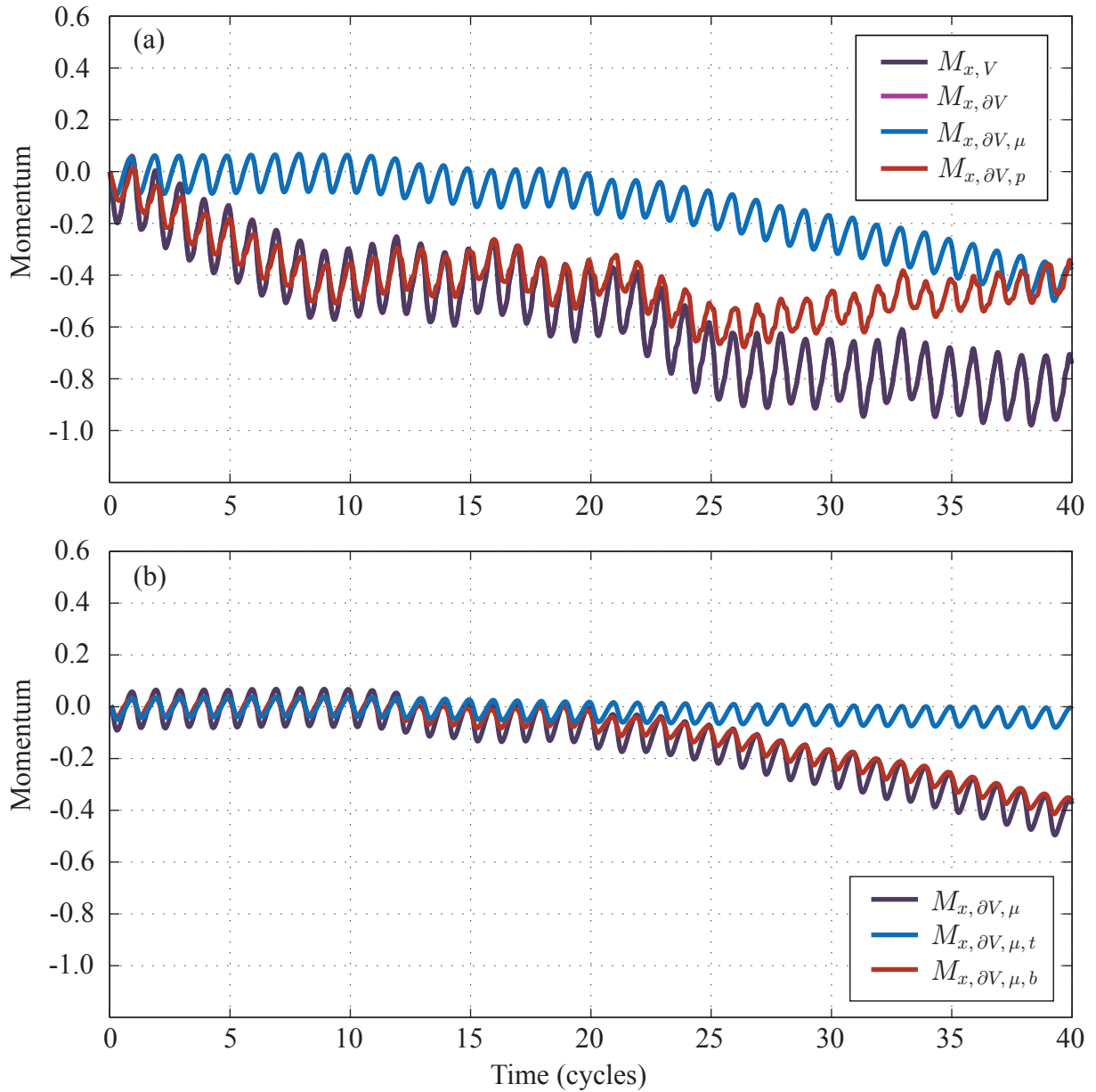
Figure 4.17: For the R0-C2 case, (a) the x-momentum ($M_{x,V}$, purple; $M_{x,\partial V}$, magenta) and its constituent viscous stress ($M_{x,\partial V,\mu}$, blue) and pressure ($M_{x,\partial V,p}$, red) contributions, and (b) the viscous stress ($M_{x,\partial V,\mu}$, purple) and its contributions from the top (blue) and bottom (red) boundaries. In (a), the curves for $M_{x,V}$ (purple) and $M_{x,\partial V}$ (magenta) overlap each other.
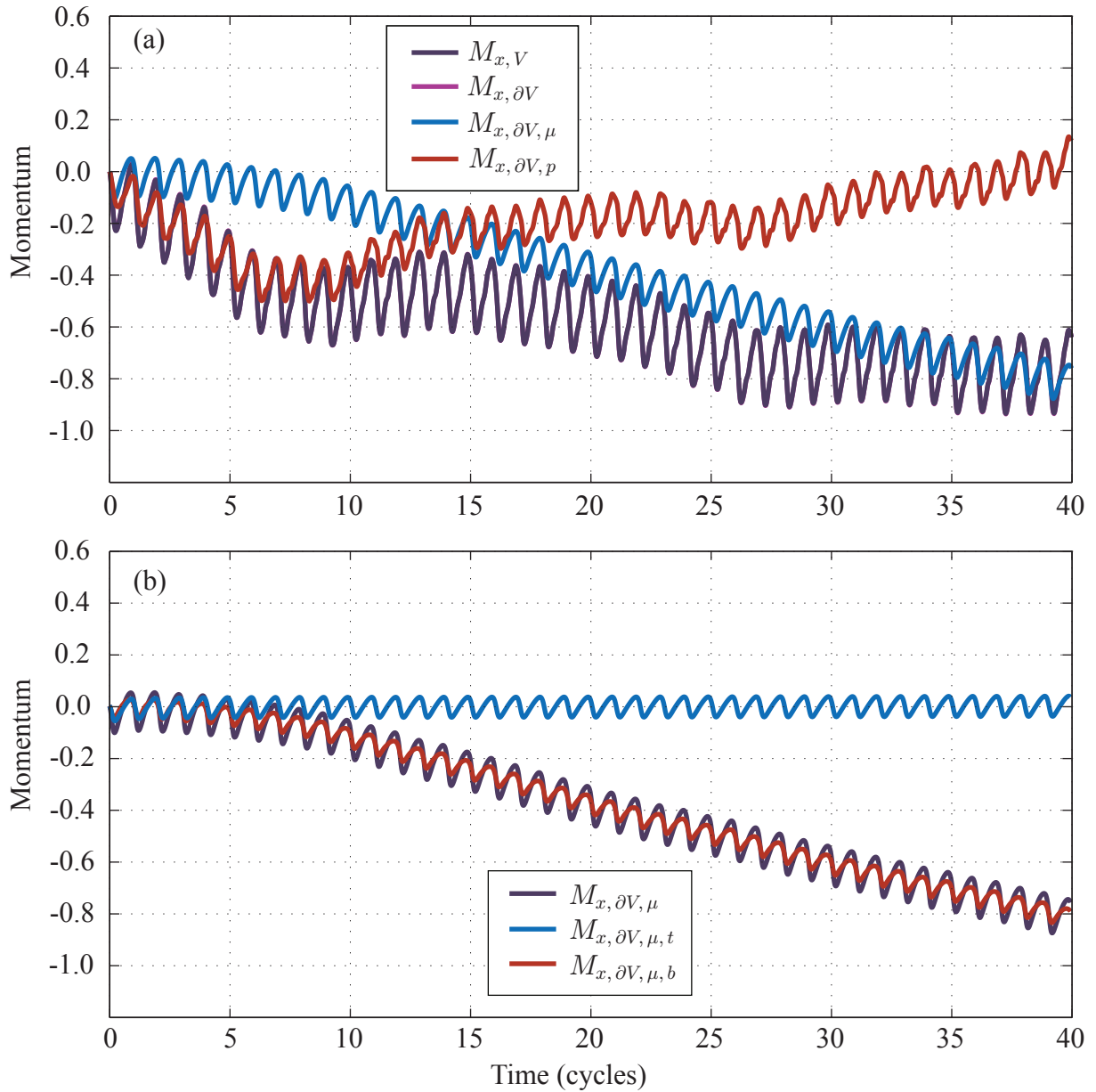
Figure 4.18: For the R0-C4 case, (a) the x-momentum ($M_{x,V}$, purple; $M_{x,\partial V}$, magenta) and its constituent viscous stress ($M_{x,\partial V,\mu}$, blue) and pressure ($M_{x,\partial V,p}$, red) contributions, and (b) the viscous stress ($M_{x,\partial V,\mu}$, purple) and its contributions from the top (blue) and bottom (red) boundaries. In (a), the curves for $M_{x,V}$(purple) and $M_{x,\partial V}$ (magenta) overlap each other.
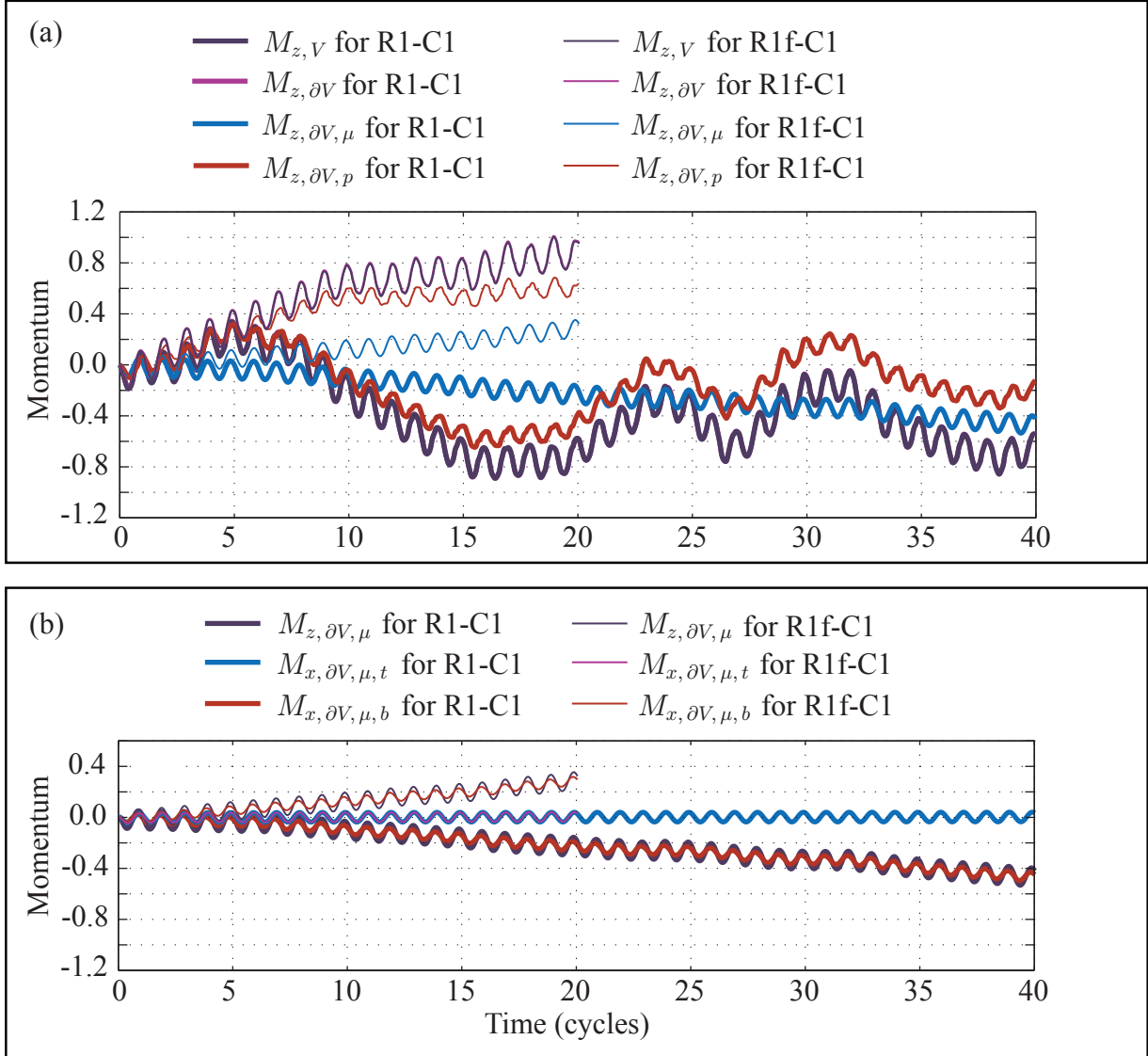
Figure 4.19: For the R1-C1 (thick) and R1f-C1 (thin) cases, (a) the x-momentum ($M_{x,V}$, purple; $M_{x,\partial V}$, magenta) and its constituent viscous stress ($M_{x,\partial V,\mu}$, blue) and pressure ($M_{x,\partial V,p}$, red) contributions, and (b) the viscous stress ($M_{x,\partial V,\mu}$, purple) and its contributions from the top (blue) and bottom (red) boundaries. In (a), the curves for $M_{x,V}$ (purple) and $M_{x,\partial V}$ (magenta) overlap each other.

90

EFFECT ON THE FLOW FIELD DUE TO THE COMBINED FLOW AND RIPPLE ASYMMETRIES.

Figure 4.20 shows the variations in the momentum for the R1-C2 and R1f-C2 cases. Figure 4.20(a) reveals a trend similar to that for R0-C2: the overall momentum decreases, and $M_{x, \partial V, \mu}$ decreases consistently. The momentum remains nearly steady from about 17 to 25 cycles, before again decreasing to some extent. $M_{x, \partial V, p}$ also increases consistently after about 15 cycles, which helps to balance $M_{x, \partial V, \mu}$, so that a steady state is reached. For the R1f-C2 case, $M_{x, \partial V, \mu}$ at first increases slightly before beginning to decrease. Figure 4.20(b) indicates that all of the net momentum changes originate from the bottom boundary.

Figure 4.21 depicts the variations in the momentum for the R1-C4 and R1f-C4 cases. For the R1-C4 case, Figure 4.21(a) reveals that the momentum initially decrease, remains nearly steady from 20 to 35 cycles, before again decreasing. $M_{x, \partial V, \mu}$ decreases consistently from the beginning while $M_{x, \partial V, p}$ increases after about 20 cycles, again helping to balance the decrease in $M_{x, \partial V, \mu}$ and hence steadying the momentum. For the R1f-C4 case, $M_{x, \partial V, \mu}$ decreases, but at a slower pace. Figure 4.21(b) shows that, as before, all of the net momentum contributions emanate from the bottom boundary.

Figure 4.22 provides a comparison of $M_{x, \partial V, \mu}$and $M_{x, \partial V, p}$ for all six base cases. From Figure 4.22(a), it can be observed that $M_{x, \partial V, \mu}$ is greater for the asymmetric ripple and increases with current asymmetry. Figure 4.22(b) shows a similar comparison for $M_{x, \partial V, p}$. For all except the R0-C1 and R1-C1 cases, a consistent increase in $M_{x, \partial V, p}$ is evident after about 25 cycles.

Figure 4.23 indicates the momentum for all six base cases and reveals that all cases with an asymmetric current attain a similar long-term momentum. R0-C1 in particular is quite different. The R1-C4p case, whose flow started at the beginning of the weak leftward flow, shows that the long-term momentum is insensitive to these two different initial conditions. Although each case exhibits different behaviour with respect to $M_{x, \partial V, \mu}$ and $M_{x, \partial V, p}$, these components seem to balance out eventually in order to produce a similar long-term momentum.

4.3.3.2 Mean momentum fluxes

As this section reveals, the momentum flux contributed by the upper boundary is relatively small. At the bottom boundary, it can be seen that the total rate of change in momentum contributed by the pressure term ($M'_{x, \partial V, p}$) is of the same order as that due to viscous
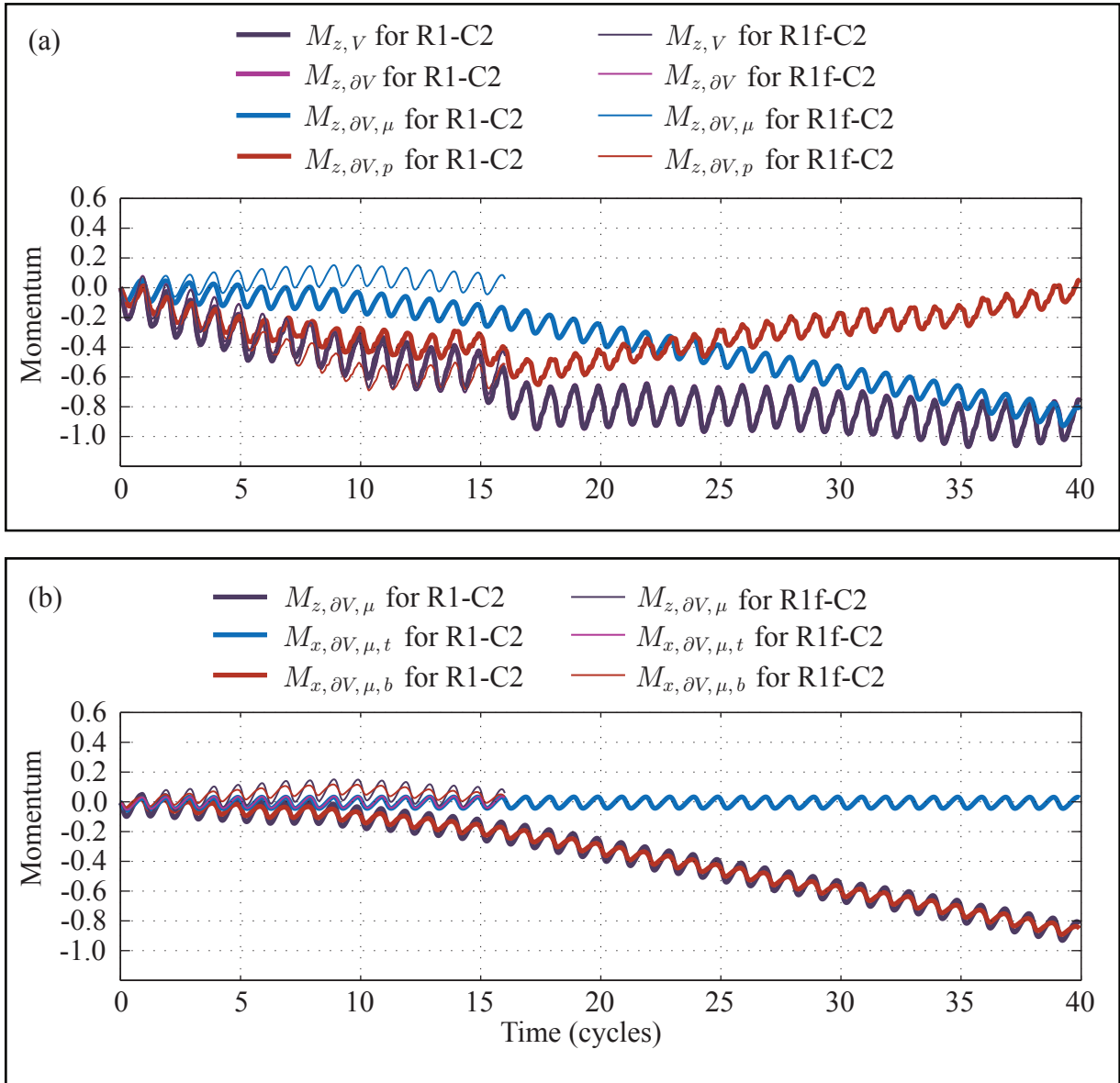
Figure 4.20: For the R1-C2 (thick) and R1f-C2 (thin) cases, (a) the x-momentum ($M_{x,V}$, purple; $M_{x,\partial V}$, magenta) and its constituent viscous stress ($M_{x,\partial V,\mu}$, blue) and pressure ($M_{x,\partial V,p}$, red) contributions, and (b) the viscous stress ($M_{x,\partial V,\mu}$, purple) and its contributions from the top (blue) and bottom (red) boundaries. In (a), the curves for $M_{x,V}$ (purple) and $M_{x,\partial V}$ (magenta) overlap each other.
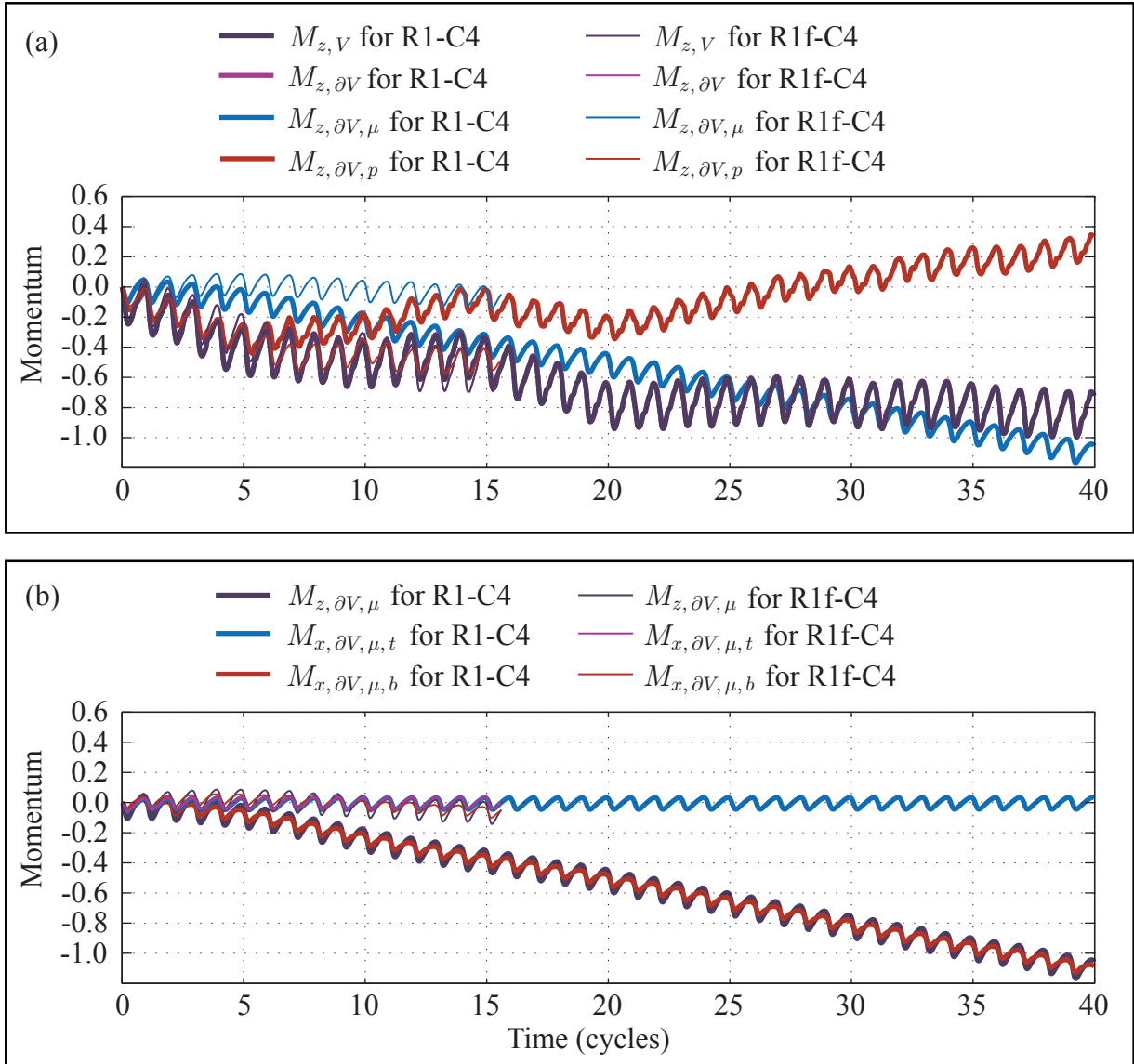
Figure 4.21: For the R1-C4 (thick) and R1f-C4 (thin) cases, (a) the x-momentum ($M_{x,V}$, purple; $M_{x,\partial V}$, magenta) and its constituent viscous stress ($M_{x,\partial V,\mu}$, blue) and pressure ($M_{x,\partial V,p}$, red) contributions, and (b) the viscous stress ($M_{x,\partial V,\mu}$, purple) and its contributions from the top (blue) and bottom (red) boundaries. In (a), the curves for $M_{x,V}$ (purple) and $M_{x,\partial V}$ (magenta) overlap each other.
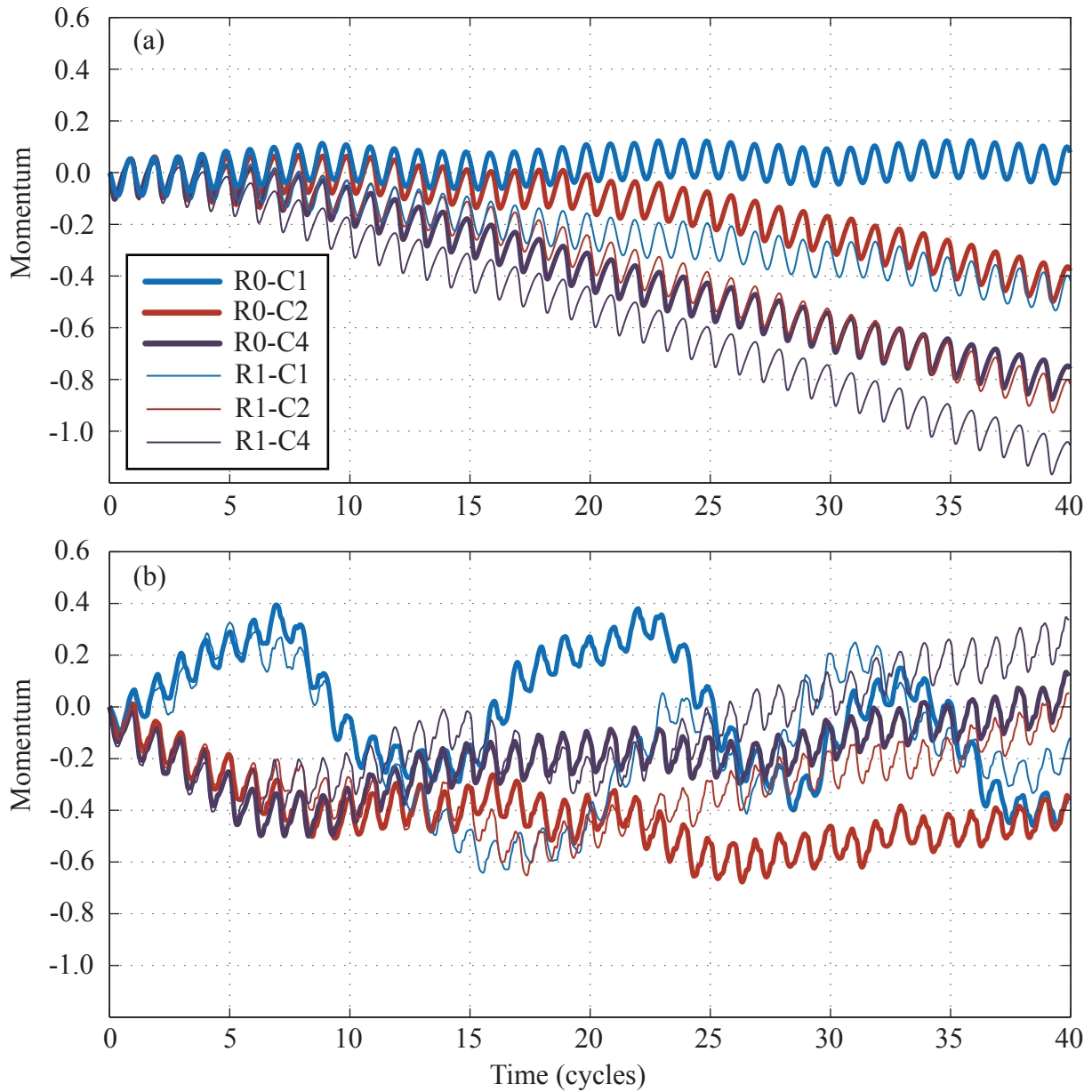
Figure 4.22: Momentum contributed during the first 40 cycles by (a) the viscous stress term ($M_{x,\partial V,\mu}$) and (b) the pressure term ($M_{x,\partial V,p}$) for the R0-C1 (blue, thick), R0-C2 (red, thick), R0-C4 (purple, thick), R1-C1 (blue, thin), R1-C2 (red, thin), and R1-C4 (purple, thin) cases.

94
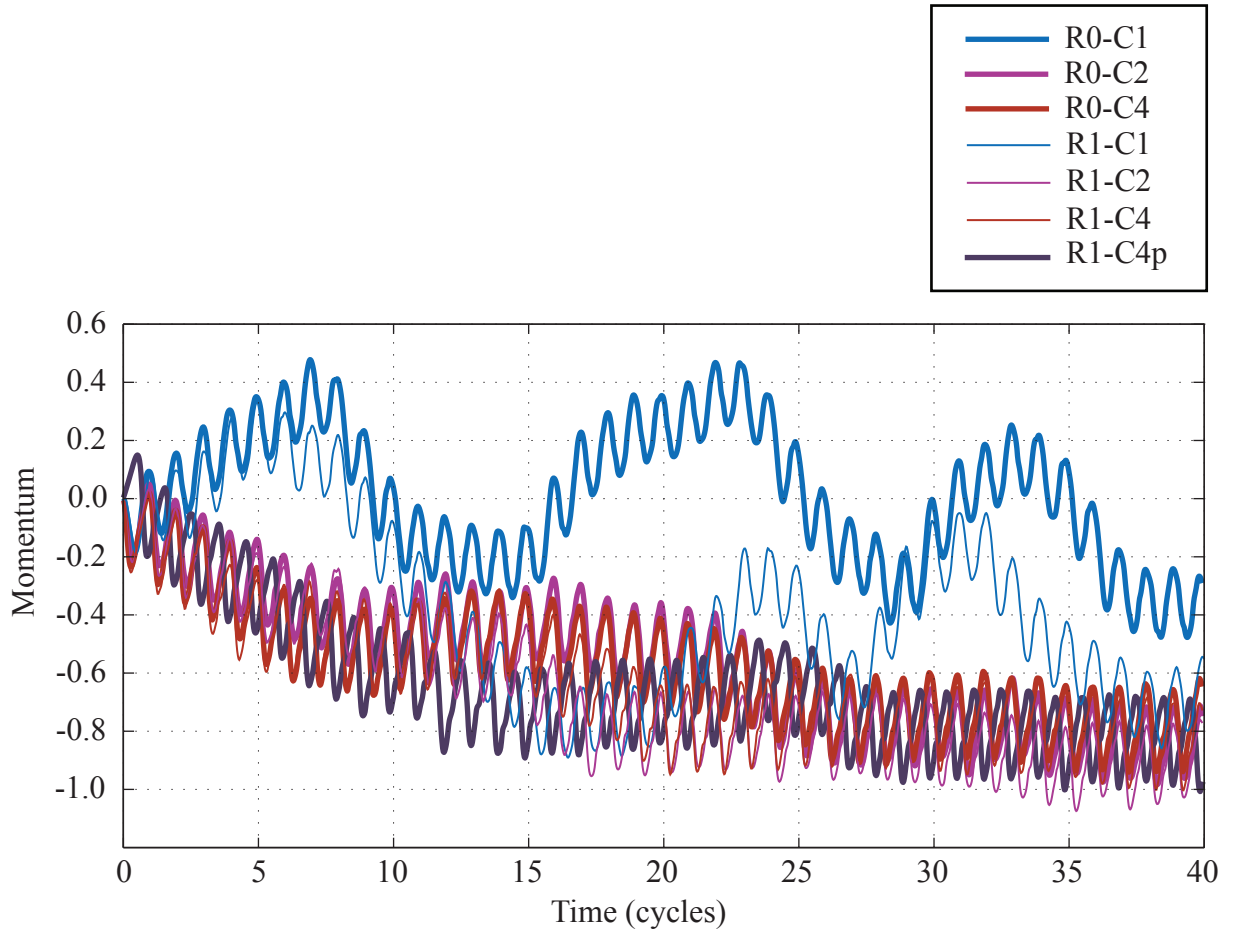
Figure 4.23: Momentum ($M_{x,\partial V}$) during the first 40 cycles.

stress ($M'_{x,\partial V,\mu}$), although the magnitudes of the pressure momentum flux at a point on the ripple ($F_{x,p}$) might be several orders of magnitude greater than that of viscous stress ($F_{x,\mu}$). With respect to the bottom boundary, the findings demonstrate a considerable momentum flux contribution due to (1) the interaction of the vortex with the ripple and (2) the strong shear layers formed on either side of the ripple crest.

This section examines observations regarding the nature of mean momentum fluxes during the last 20 cycles. For each of the momentum flux components, the average over the last 20 cycles is calculated using

$$\bar{F}(x,t) = \frac{1}{20} \sum_{i=20}^{40-1} F\left(x, iT + t\right), \, t \in [0,T], \; x \in \left[0, \frac{4}{3}\right]$$

Figure 4.24 displays the average variation in the total momentum flux ($F_{x,p} + F_{x,\mu}$) for all six base cases over a single cycle. The two cycles represented are periodic extensions of the same data. It can be observed that, as expected, the momentum fluxes are of opposite signs on the two sides of the ripple. Some peaks occur just off the crest at times immediately following each flow reversal. The net flux over a period is negative for all except the all-symmetric case. For for the symmetric ripple, this net negativity comes largely from the short period about $t = 0.2$, where the maximum in negative momentum flux occurs. In contrast, for the asymmetric ripple, the peak negative momentum flux is much larger than the peak positive value at all times. The next step is to separate the contributions to this from the top and bottom boundaries.

Figure 4.25 displays the momentum fluxes at the top boundary ($F_{x,p,t} + F_{x,\mu,t}$). It can be seen that they are oscillatory in nature, resembling the flow forcing, but with a slight phase-shift lag. This lag occurs because of the boundary layer experiences a phase shift relative to the outer flow, as discussed earlier in section 2.2. It should be noted that the magnitude of the flux field at the top boundary is several orders of magnitude smaller than that of the overall momentum flux field ($F_{x,p} + F_{x,\mu}$).

Figure 4.26 depicts the momentum flux fields associated with the bottom boundary ($F_{x,p,b} + F_{x,\mu,b}$). As is already known, this is the momentum flux field that contributes to the net changes in momentum in the interior of the domain. As expected, it is similar to the overall momentum flux field ($F_{x,p} + F_{x,\mu}$) but with a slightly decreased magnitude.

The next step is to separate the contribution to momentum at the bottom boundary into that arising from the pressure term ($F_{x,p,b}$) and that stemming from the viscous stress term ($F_{x,\mu,b}$). Figures 4.27 and 4.28 display, for the lower boundary, the distribution of the flux due to pressure and due to viscous stress, respectively. It should be noted that the
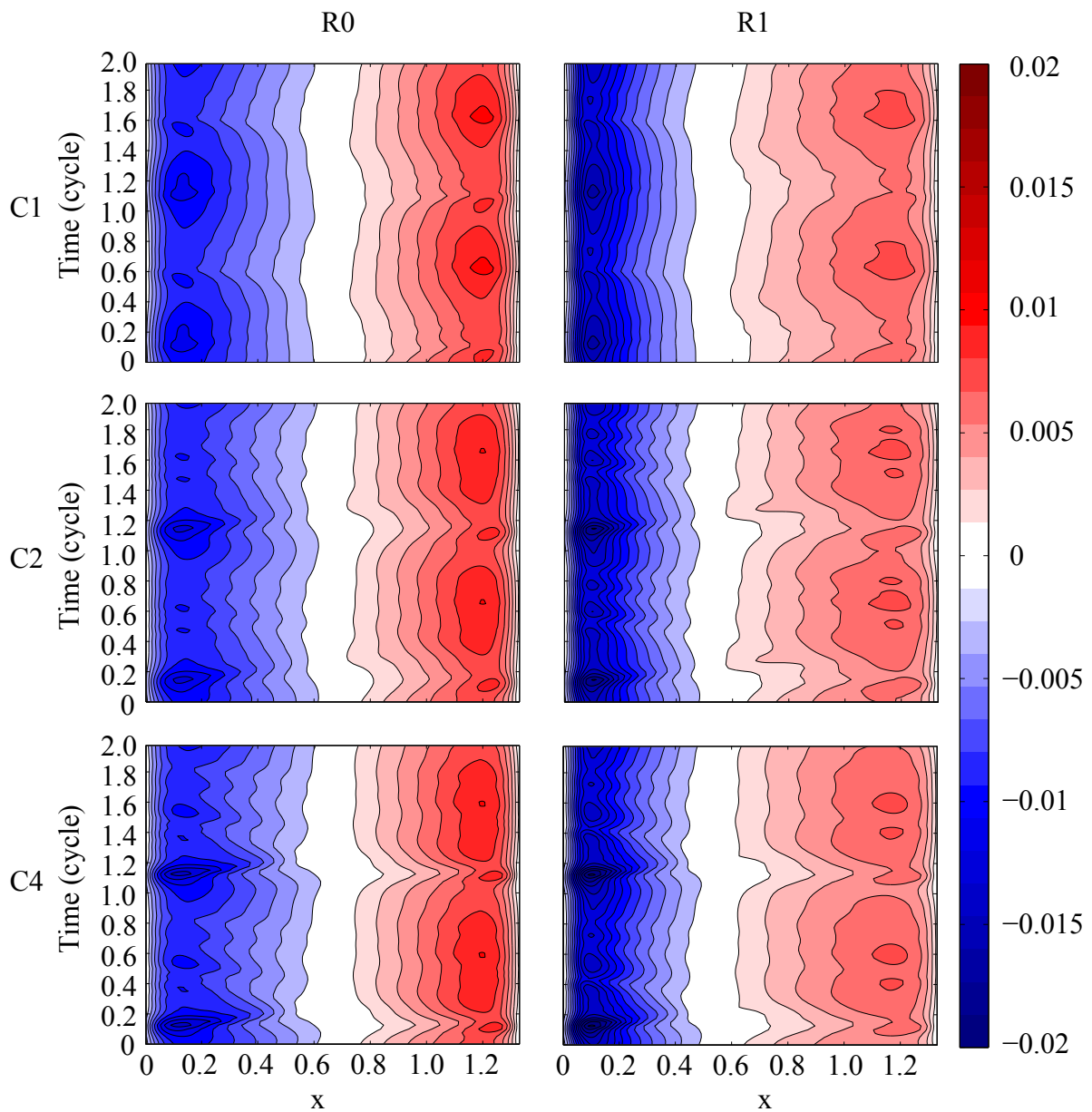
Figure 4.24: Average variation in the total momentum flux $(F_{x,p} + F_{x,\mu})$ for all six base cases over a single cycle. The two cycles shown are periodic extension of the same data. The average is taken over cycles 20 to 40.

Figure 4.25: Average variation in the momentum flux at the upper boundary $(F_{x,p,t} + F_{x,\mu,t})$ for all six base cases over a single cycle. The two cycles shown are periodic extensions of the same data. The average is taken over cycles 20 to 40.

Figure 4.26: Average variation in the momentum flux at the bottom boundary ($F_{x,p,b} + F_{x,\mu,b}$) for all six base cases over a single cycle. The two cycles shown are periodic extensions of the same data. The average is taken over cycles 20 to 40.

magnitudes of the pressure term contributions are about an order of magnitude larger than those from the viscous stress term. However, as indicated in Figure 4.14 for the R1-C4 case, the magnitudes of the integrated (time and space) values $(M'_{x,\,\partial V,\,p,\,b}, M'_{x,\,\partial V,\,\mu,\,b})$ of those plotted in Figures 4.27 and 4.28 are of the same order. A more detailed discussion of the viscous stress field follows.

In the momentum flux field due to viscous stress $(F_{x,\,\mu,\,b})$ for the R0-C1 case (Figure 4.28), it can be seen that, as expected, the positive and negative regions are nearly symmetric. The R1 cases have generally have larger and more intense negative areas, which is a good indication of the consistent decrease in $M_{x,\,\partial V,\,\mu}$, which is shown in Figure 4.22(a).

The features nearer the trough, inside the dotted-green curves, are the result of vortex interactions at the surface of the ripple, as illustrated in Figure 4.29, which shows the vortex structures at those times. Figures 4.29(a,b) depict the vorticity field taken at the 0.9 cycles for the C1 flow forcing. At that time, the vortex formed during the negative flow forcing interacts with the surface of the ripple, which creates a strong, thin, shear layer under the vortex, giving rise to its signature in the viscous stress field $(F_{x,\,\mu,\,b})$ indicated by the blue region enclosed by the dotted-green curve in Figure 4.28(a,b). A similar vortex interaction also occurs at 0.4 cycles, as displayed in Figures 4.29(c,d). As with the previous instance, this interaction creates a strong, thin, shear layer, which results in a positive peak in the viscous stress field around this point, as indicated by the area enclosed by the second dotted green curve in Figure 4.28(a-b). Figures 4.29(e,f) and 4.29(g,h) show similar vortex interactions that occur for the C2 and C4 flow forcings at the 0.3 and 0.2 cycles, respectively, and that creates the positive peaks in the viscous stress field, which are indicated by the dotted green curves in Figure 4.28(c-f). For the C2 and C4 cases, increasingly stronger vortices impinge on the surface of the ripple, thus creating increasingly larger positive peaks in the viscous stress fields at those times. Very little difference is evident between the viscous stress fields of the two ripples, R0 and R1.

In the viscous stress field, the areas inside the dashed-green curves in Figure 4.28 have a different origin. They are caused by intense, thin, shear layers generated on either side of the ripple crest, as confirmed by the Figures 4.30 and 4.31. The first consideration is the negative momentum flux fields encircled by the dashed green curves in the viscous stress field, as indicated in Figure 4.28. Figure 4.30 depicts the strong shear layers associated with these areas at those times. For example, for the C1 flow forcing, Figures 4.30(a,b) show the shear layers formed at 0.1 cycles during a strong rightward flow, which indicate a maximum just to the left of the crest, where the flow outside the boundary layer is strongest. This same reasoning holds for the other cases and is confirmed by Figures 4.30(c,d) for the C2 flow forcing and by Figures 4.30(e,f) for the C4 flow forcing. It should be noted that the contours used across the figures have different $\Delta\omega$ values, which were assigned in order to
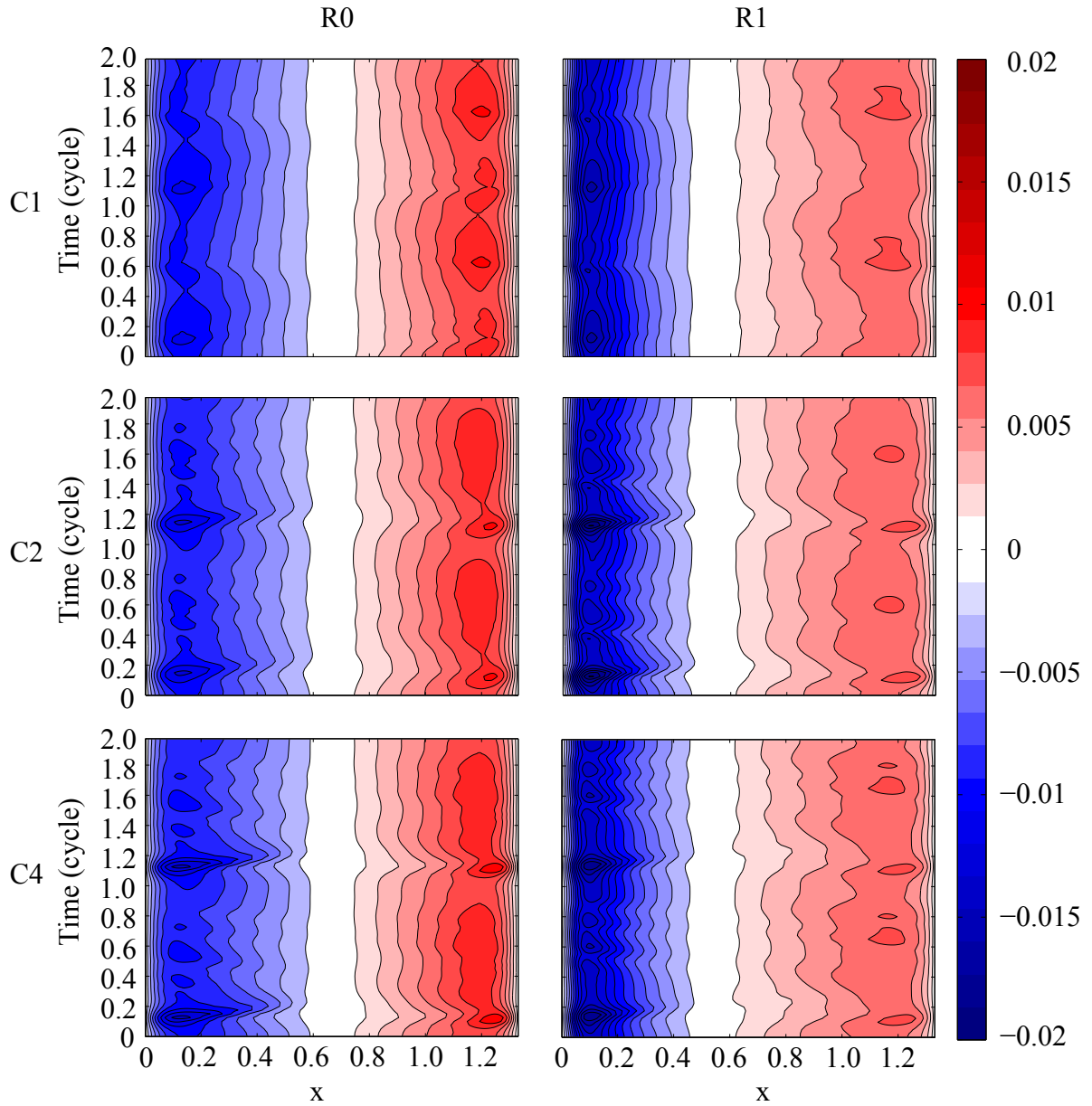
Figure 4.27: Average variation in the momentum flux due to the pressure term at the bottom boundary ($F_{x,p,b}$) for all six base cases over a single cycle. The two cycles shown are periodic extensions of the same data. The average is taken over cycles 20 to 40.
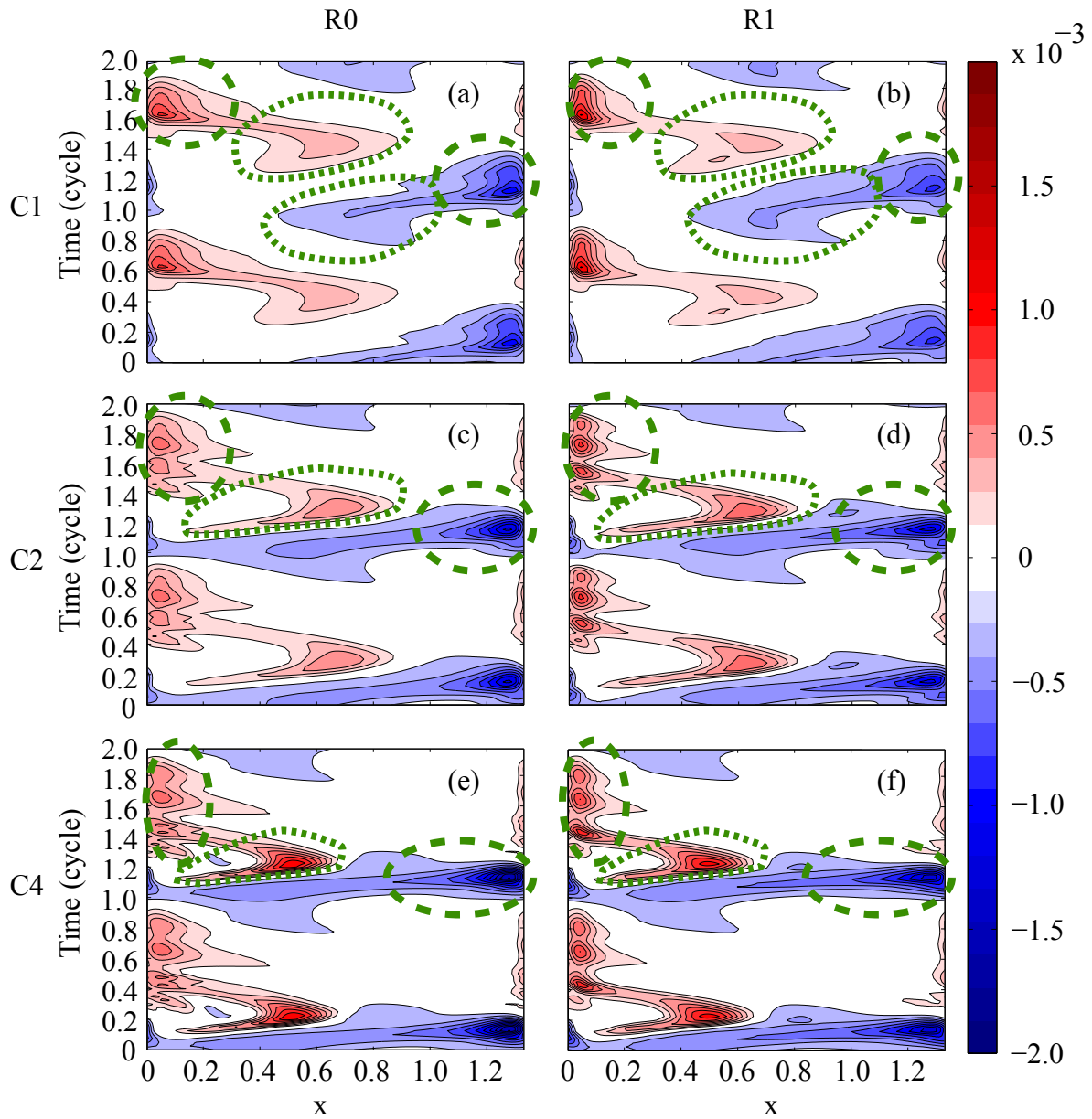
Figure 4.28: Average variation in the momentum flux due to the viscous stress term at the bottom boundary ($F_{x,\mu,b}$) for all six base cases over a single cycle. The two cycles shown are periodic extensions of the same data. The average is taken over cycles 20 to 40. Green-dashed and green-dotted lines indicate viscous stresses attributed to thin shear layers and vortex-ripple interactions, respectively.
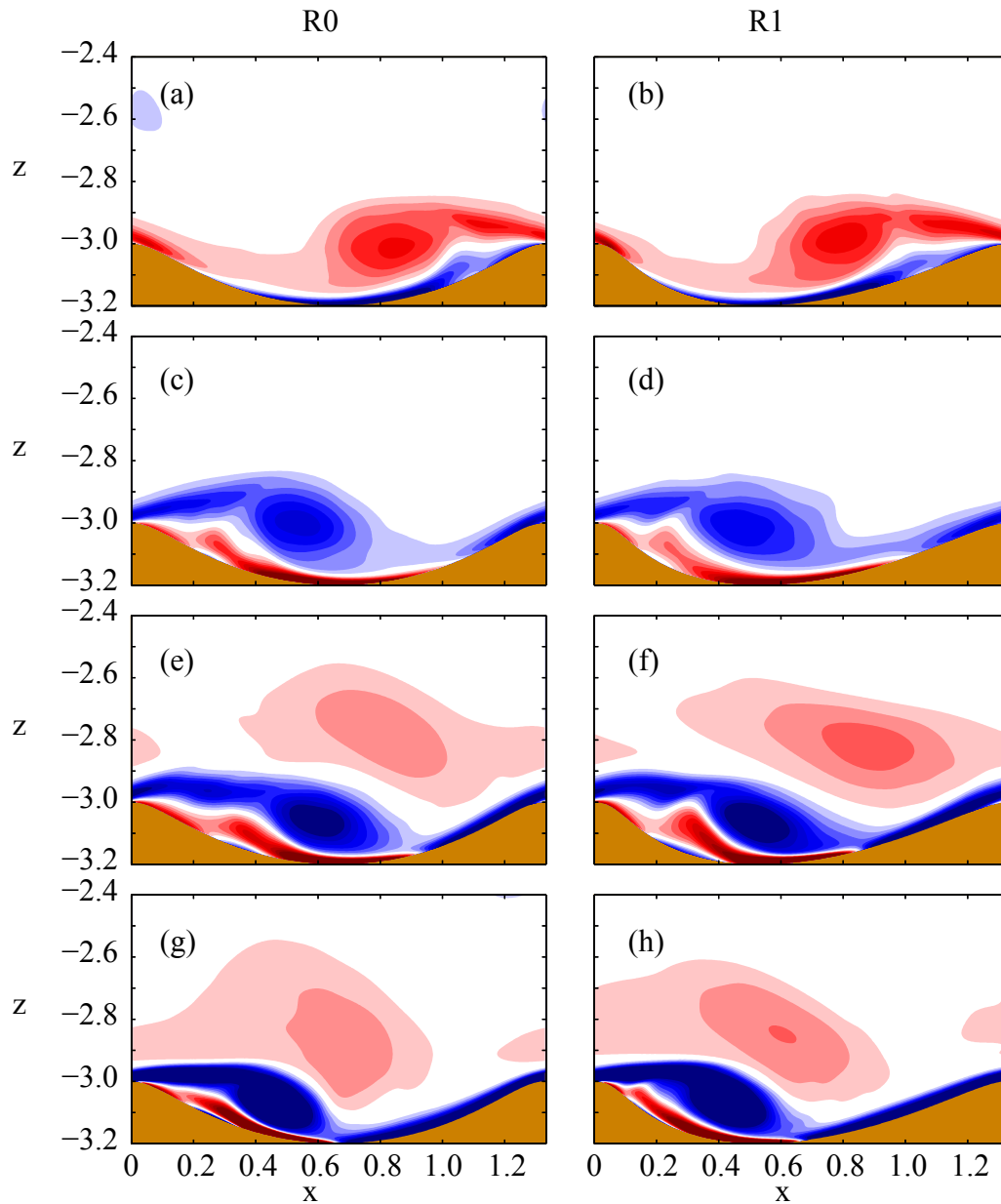
Figure 4.29: Vorticity fields of (a) R0-C1 at time 0.9 cycles, (b) R1-C1 at 0.9 cycles, (c) R0-C1 at 0.4 cycles, (d) R1-C1 at 0.4 cycles, (e) R0-C2 at 0.3 cycles, (f) R1-C2 at 0.3 cycles, (g) R0-C4 at 0.2 cycles, and (h) R1-C4 at 0.2 cycles. $\Delta\omega = 2.25$.

help clearly isolate the neighborhood of maximum vorticity.

The positive momentum flux peaks, again indicated by the green dashed curves in Figure 4.28, are also due to thin, shear layers that occur at these points in time and space, as confirmed by Figure 4.31. For example, in cases with a C2 flow forcing, a strong shear layer with a maximum just to the right of the crest is evident at 0.725 cycles, which corresponds to the location indicated in Figure 4.28. The other such peaks can be similarly confirmed from an examination of Figures 4.31(a)-(f).

As expected, these viscous stress fields also provide quantitative confirmation of the net negative momentum flux that generates a negative mean current. Table 4.1 lists the mean momentum flux due to viscous stress over the last 20 cycles for both the top and bottom boundaries. For all cases except R0-C1, it can be seen that the bottom boundary contributes a relatively large amount of momentum that is greater for the asymmetric ripple and increasingly asymmetric flow forcings.

	R0-C1	R0-C2	R0-C4	R1-C1	R1-C2	R1-C4
Top ($\times 10^{-3}$)	1.3	-0.7	1.7	1.9	1.4	1.2
Bottom ($\times 10^{-3}$)	1.8	-18.8	-40.5	-29.0	-49.1	-61.1

Table 4.1: Momentum contributed by the viscous stress term at the top and bottom boundaries during one cycle, as calculated by averaging the momentum contribution over cycles 20 to 40.

Flux contributions that are the result of vortex interactions with the ripple bed can also be estimated based on the consideration of the positive momentum flux regions inside the dotted green curves in Figure 4.28. Calculating the amount of positive flux within the green dotted curves enables a determination of the positive momentum flux that can be attributed to these vortex interactions with the surface of the ripple, as presented in Table 4.2, whose numbers indicate that these vortices play a major role in the eventual momentum of the system: they help reduce the negative momentum fluxes due to viscous stress that seem to be naturally associated with these ripple shapes and flow forcings.

	R0-C1	R0-C2	R0-C4	R1-C1	R1-C2	R1-C4
Bottom positive peak ($\times 10^{-3}$)	16.0	36.6	37.9	33.4	38.7	38.3

Table 4.2: Momentum due to viscous stress contributed by the interaction of vortices with the surface of the ripple during the last 20 cycles.
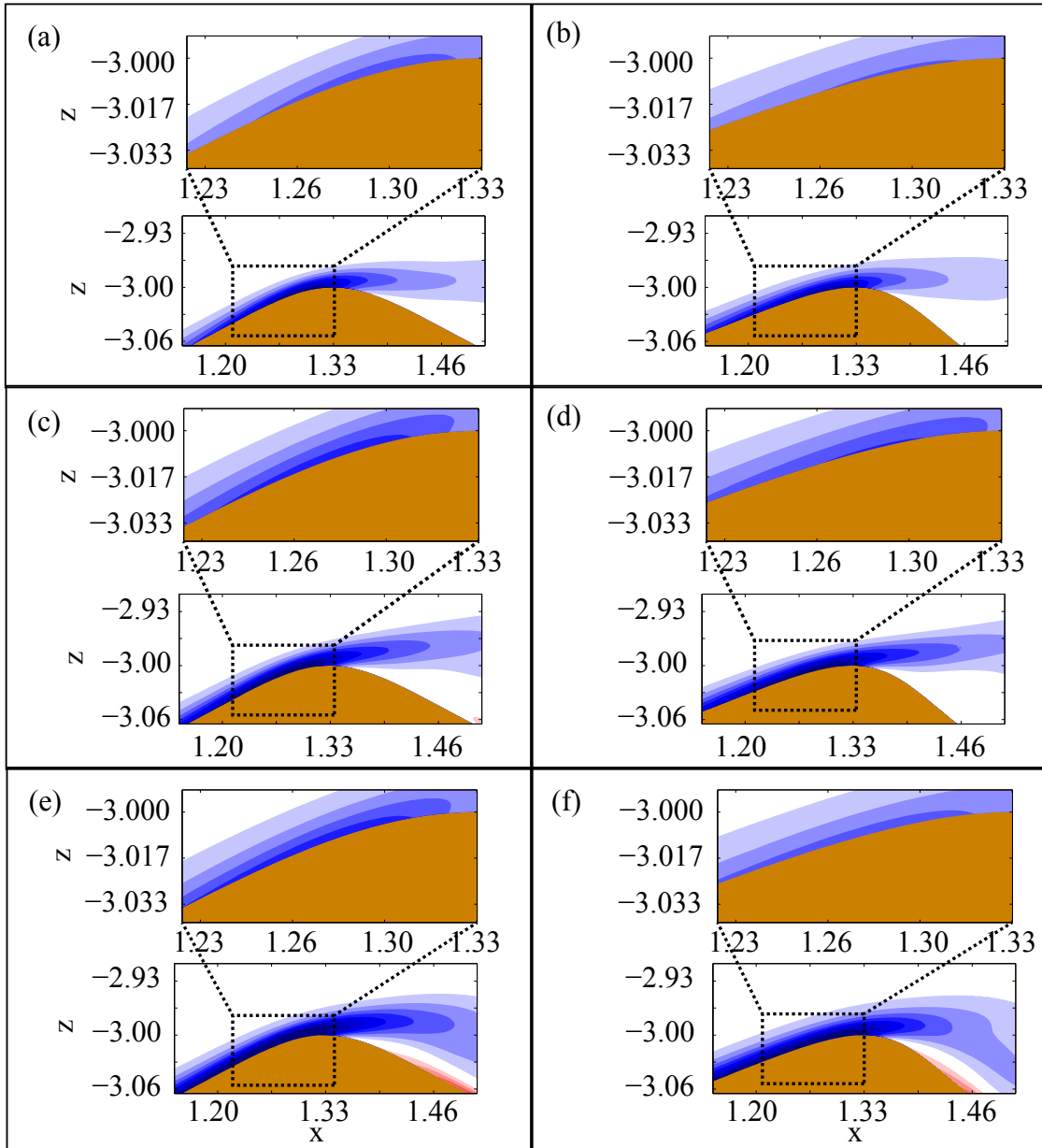
Figure 4.30: Vorticity fields for (a) R0-C1 and (b) R1-C1 taken at 0.1 cycles, for (c) R0-C2 and (d) R1-C2 taken at 0.175 cycles, and for (e) R0-C4 and (f) R1-C4 taken at 0.125 cycles. For the smaller images, $\Delta\omega = 15.0$. For the magnified images, $\Delta\omega = 41.25$, except for the C4 case, where $\Delta\omega = 56.25$.
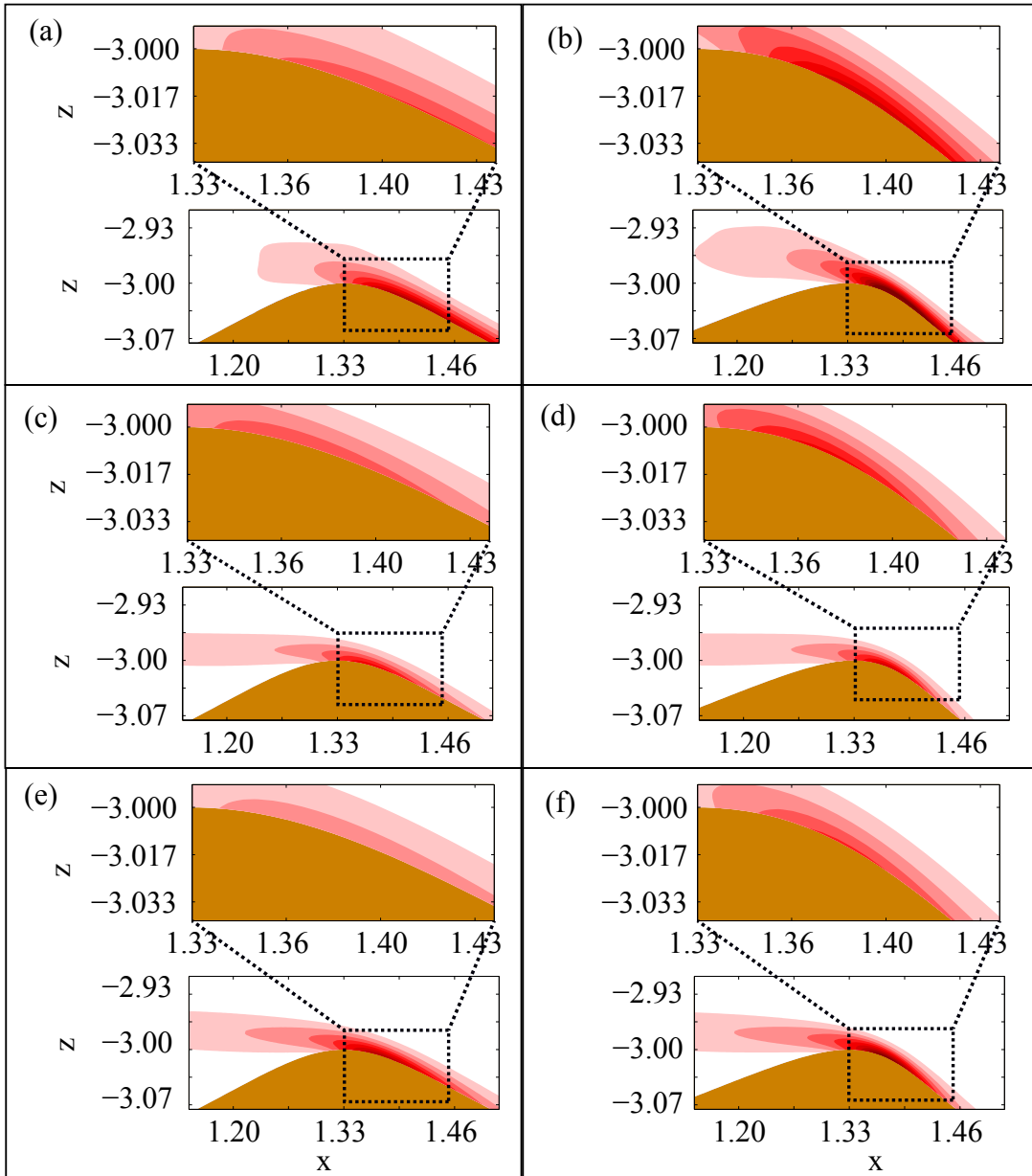
Figure 4.31: Vorticity fields for (a) R0-C1 and (b) R1-C1 taken at 0.6 cycles, for (c) R0-C2 and (d) R1-C2 taken at 0.725 cycles, and for (e) R0-C4 and (f) R1-C4 taken at 0.675 cycles. For the smaller images, $\Delta\omega = 15.0$. For the magnified images, $\Delta\omega = 30.0$.

Figure 4.32 shows the average distribution of the z-momentum at the bottom boundary during the last 20 cycles. It can be seen that the peaks enclosed by the dashed green curves in this figure coincide with the strong peaks observed for the x-momentum flux, as indicated by the areas inside the dashed green curves in Figure 4.28, which were caused by the strong, thin, shear layers that formed on the two sides of the crest. It should be noted that a large difference is apparent between the z-momentum fluxes of the two ripple shapes.

4.3.4 Transfer of momentum from the bottom boundary to the mean flow region

This section explains how the negative mean momentum induced by the asymmetric ripple and currents is related to vertical momentum fluxes and the direction of ejection of vortex pairs. For the R0-C1 case, the results indicate that the subharmonic oscillations in the x-momentum correlates with slow variations in the formation and direction of the ejection of the vortex pairs.

4.3.4.1 Momentum and its fluxes in the region just containing the mean flow

Here we quantify the vorticity and x-momentum in the subdomain $-2.9 < z < -1$ for the case R1-C2 (see Figure 4.12). This domain approximately contains the region where the mean current is established. As noted earlier, all other cases with asymmetric forcings have similar momentum curves and the mechanisms of momentum transfer to the mean-flow region is likely to be similar to this case. Figure 4.33 shows the x-momentum within $-2.9 < z < -1$ (mulberry) and momentum fluxes crossing the lines $z = -1$ (red) and $z = -2.9$ (blue), together with their viscous (dashed) and advective (solid) contributions. Observe that vorticity is transferred to the mean-flow region mostly by advection from the bottom boundary. Observe that the trend in momentum and its fluxes during the first five cycles continues until about 20 cycles, after which the momentum associated with the mean-flow region becomes somewhat steady. This is similar to the observation made earlier in Section 4.3.3.2 for the case of the entire domain. The viscous stress flux increases slowly during the first 20 cycles and then increases at a faster rate, balancing that transferred by advection. To take a closer look, we now consider the periods 0 to 5 and 30 to 35.

Figures 4.34(a-f) show the evolution of vorticity in the subdomains $-2.3 < z < -1$ (top), $-2.9 < z < -1$ (middle), and the evolution of x-momentum in the subdomain $-2.9 < z < -1$ (bottom) during the first five cycles (left) and during the cycles 30 to 35 (right). Fluxes crossing the upper line ($z = -1$) and the lower line ($z = -2.3$ or $z = -2.9$)
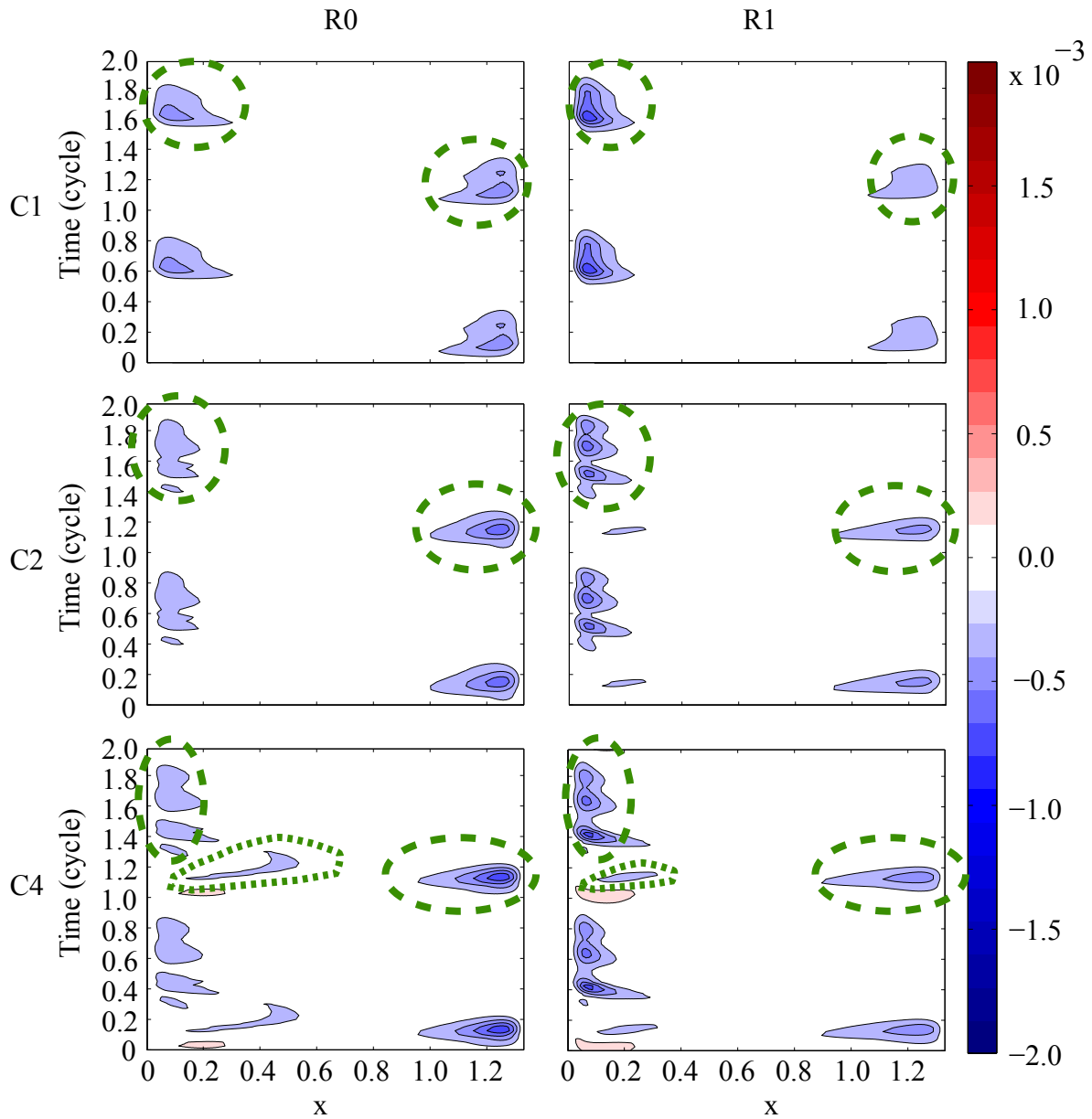
Figure 4.32: Average variation in the momentum flux due to the viscous stress term at the bottom boundary $(F_{z,\mu,b})$ for all six base cases over a single cycle. The two cycles shown are periodic extensions of t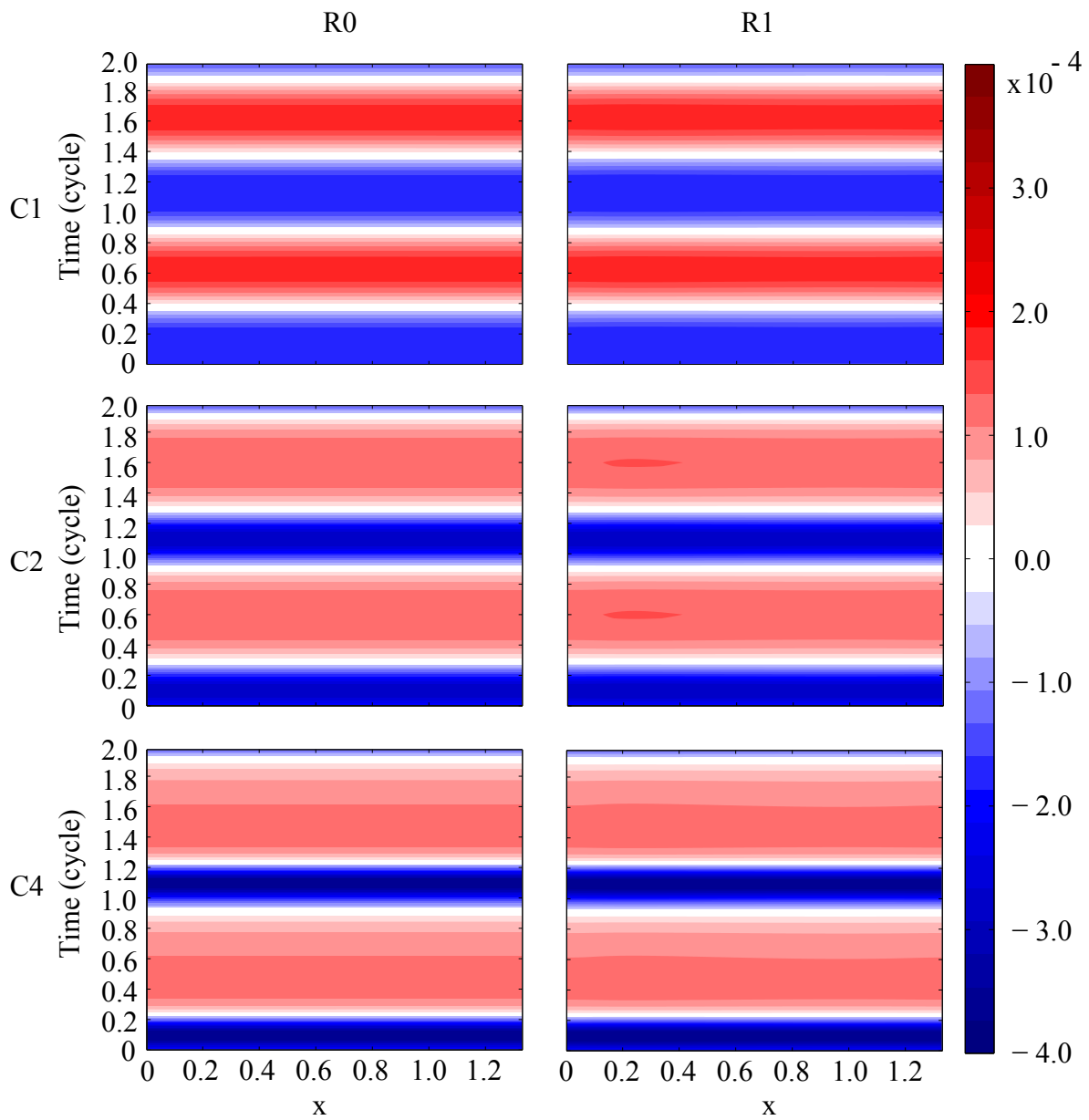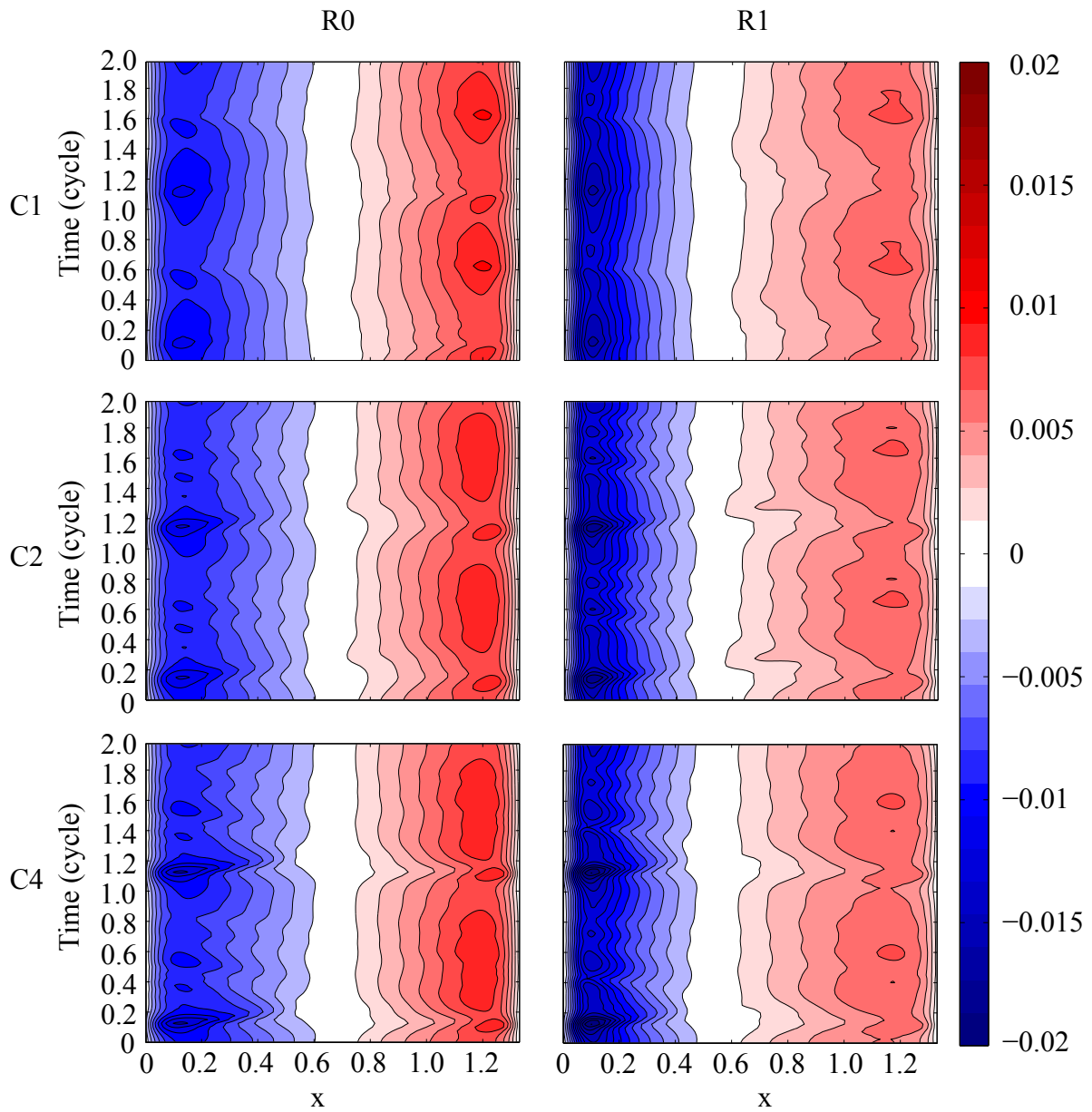he same data. The average is taken over cycles 20 to 40. Green-dashed and green-dotted curves indicate viscous stresses attributed to thin shear layers and vortex-ripple interactions, respectively.
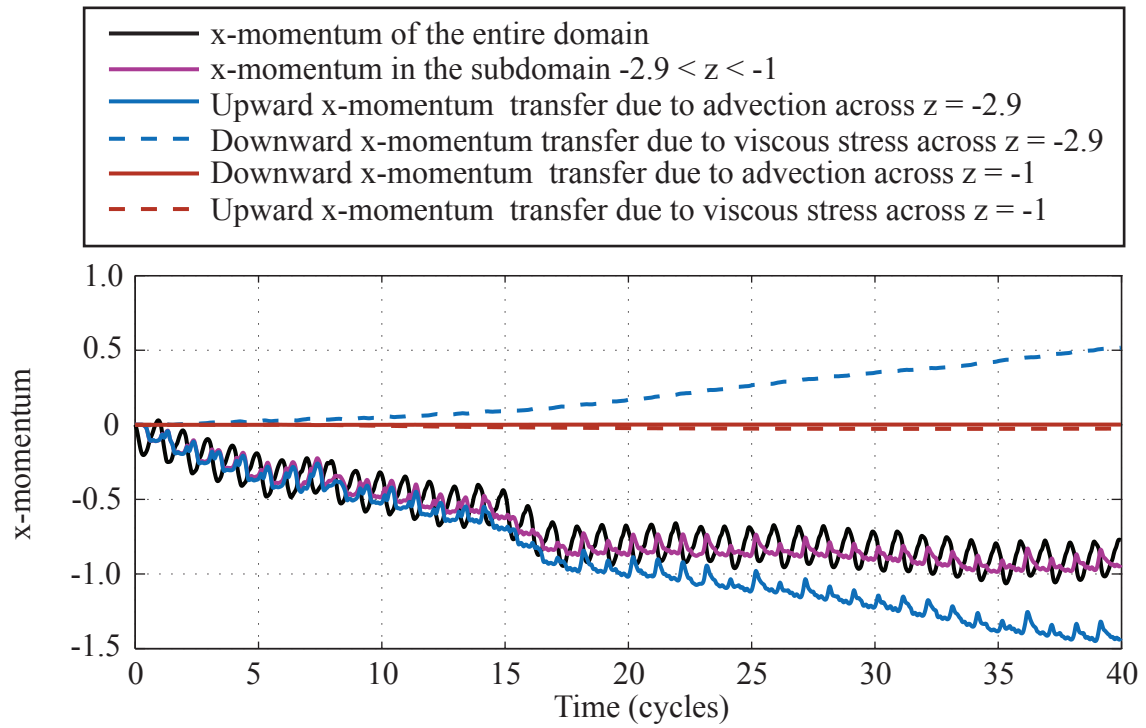
Figure 4.33: The evolution of x-momentum in the subdomain $-2.9 < z < -1$ (mulberry) and its advective (solid) and viscous stress (dashed) contributions across the lines $z = -2.9$ (blue) and $z = -1$ (red) for the case R1-C2. The black curve indicates the x-momentum of the entire domain.

are shown in red and blue, respectively. Solid and dashed curves show fluxes due to advection and viscous stress, respectively. Vorticity (panels (a)-(d)) of the subdomain is shown in solid mulberry. Momentum (panels (e)-(f)) of the entire domain and the subdomains are shown in solid black and mulberry, respectively. The vorticity of the entire domain is theoretically zero and bounded by about 10^{-4} in the simulations. By the Stokes' theorem, the vorticity of the subdomain equals its circulation, which becomes the circulation across the top and bottom boundaries since circulation over the lateral boundaries cancels by periodicity. So, the total mean vorticity equals $l(\bar{u}_t - \bar{u}_b)$, where $\bar{u}_t$ and $\bar{u}_b$ are the mean horizontal velocities across the top and bottom boundaries. l is length of the domain in the x-direction. In our simulations, the difference between the total vorticity and $l(\bar{u}_t - \bar{u}_b)$ is bounded by about 10^{-4}.

As shown in Figure 4.34(e), during the first five periods, the momentum of the system gradually decreases and the transfer of momentum to the subdomain is dominated by advection originating from the bottom boundary. Figure 4.34(c) shows that the vorticity transferred is also dominated by advection, again originating from the bottom boundary. Vorticity transfer, either positive or negative, peaks just after flow reversals, which corresponds to the times of vortex pair ejections. In addition, a larger quantity of positive (clockwise) vorticity is transferred to the interior near each positive-to-negative flow reversals, which corresponds to the stronger clockwise vortex constituting each vortex pair at these vortex pair ejections. Figure 4.34(a) shows that there is a transfer of vorticity across $z = -2.3$, this time dominated by the advection of positive vorticity. The momentum in the mean-flow region is observed to decrease nearer times when the positive vorticity attains a maximum and increase nearer times when the magnitude of negative vorticity reaches a maximum. This can be explained in terms of vortex movements. During the first flow reversal (positive to negative), a vortex pair is formed with a stronger positive (clockwise) vortex, located above the weaker negative vortex, and ejected left-upward, giving the net positive vorticity flux across $z = -2.9$. Since vortex lines move with the fluid, this left-upward movement of the vortex pair indicates that the fluid in its neighborhood has a leftward velocity or negative momentum, hence decreasing the momentum. During the second flow reversal, a vortex pair is formed with a stronger positive vortex but located below the weaker negative vortex, ejecting right-downward. This causes only part of the negative vortex to cross the line $z = -2.9$, giving the negative vorticity flux across $z = -2.9$ and increasing the momentum of the system. The positive vortex moves downwards and does not cross $z = -2.9$ and is short-lived due to its interaction with the ripple.

During the quasi-steady state, Figure 4.34(b) shows that the vorticity in the region $-2.3 < z < -1$ remains relatively steady with a considerable amount of flux due to viscous stress across $z = -2.3$, although advection still dominates. The lack of large spikes

Time range (cycle)
3 to 4
8 to 9
15 to 16
24 to 25
29 to 30

Table 4.3: Time periods considered for tracing the initial trajectory of newly formed vortex pairs that moves away from the boundary after their creation for the case R0-C1.

indicates that strong vortices do not play a large role in the transfer of momentum to this region at this stage. In contrast, Figure 4.34(d) shows that strong vortices still cross $z = -2.9$, much like during the first five cycles.

Note that these give no indication of the direction of ejection of vortex pairs, which we will show in the next section to be correlated with the increase or decrease of momentum in the system.

4.3.4.2 Momentum of the system and its correlation with the direction of ejection of vortices

This section looks at the R0-C1 case with respect to observations of the initial trajectory of newly generated vortices. The paths of the vortex pairs at time periods on either side of the turning points of the period-averaged momentum curve were examined. Table 4.3 shows the periods chosen for the analysis of the vortex paths. For example, the first case involved evaluating the mean vortex field during the third and fourth periods and tracing the paths of the vortex pairs. Since consideration is directed at the mean vortex field, there will be vortex paths that branch out after starting from a single point. Only trace vortices that will eventually move away from the boundary are traced. Other vortices are generated as well, but they interact with the boundary soon after their creation, resulting in their fast dissipation near the boundary itself.

Figures 4.35(a,c,e,g,i) display the paths traced for the R0-C1 case. To identify differences between the R0-C1 vortex paths and those for other cases, vortex paths for the same times are also provided for the R0-C4 case in Figures 4.35(b,d,f,h,j). For the R0-C1 case, during periods 3 to 4, as shown in Figure 4.35(a), it can be observed that the vortex pairs are ejected in a right-upward direction. During this time, the momentum of the system is increasing. On the other hand, for the R0-C4 case, as depicted in Figure 4.35(b), newly
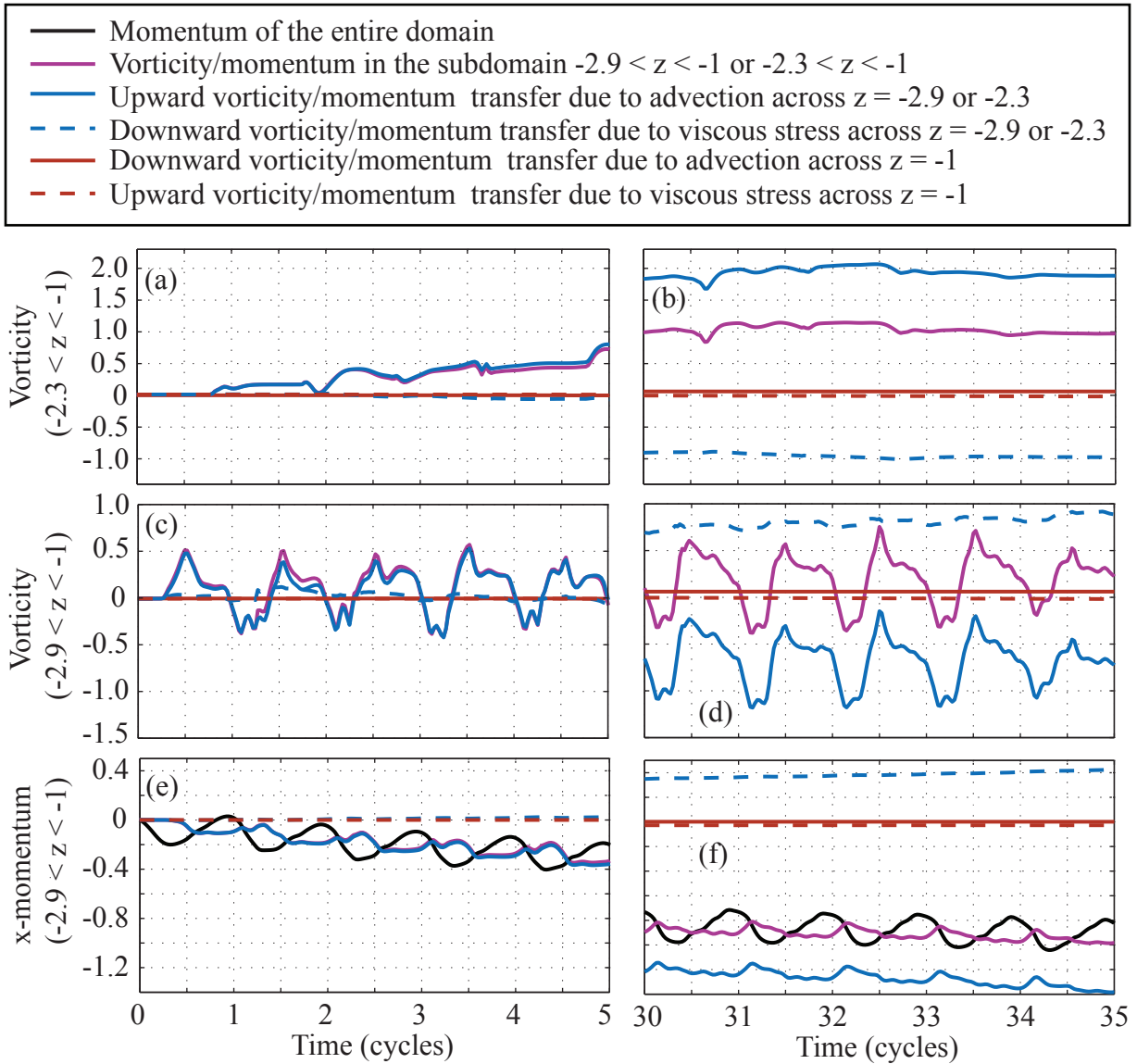
Figure 4.34: Evolution of vorticity in the subdomains $-2.3 < z < -1$ (top), $-2.9 < z < -1$ (middle), and the evolution of x-momentum in the subdomain $-2.9 < z < -1$ (bottom) during the first five cycles (left) and 30 to 35 cycles (right). The same set of line colors and styles (solid and dashed) are used to show (a-d) vorticity and (e-f) momentum. In (a-d), the red solid and dashed curves either overlap or nearly overlap each other. In (a) and (c), the mulberry and the blue curves nearly overlap each other.

generated vortices are ejected in a left-upward direction, and the momentum of this system is decreasing during these times. During periods 8 to 9, as shown in Figure 4.35(c), newly generated vortices are ejected in a left-upward direction, while the momentum of the system is decreasing. During these times, as indicated in Figure 4.35(d), vortices are ejected in a left-upward direction for the R0-C4 case, and the momentum of the system is decreasing. This same trend can be observed during other periods: 15 to 16, 24 to 25, and 29 to 30. The direction in which the newly generated vortices are ejected, either left-upward or right-upward, corresponds to the direction in which the momentum is increasing or decreasing.

The next step is to consider the R0-C1 case and to investigate the formation of these vortex pairs that tend to exhibit periodic changes in their direction of ejection. During each half cycle, two vortices are formed on either side of the ripple crest. A vortex with a clockwise (counterclockwise) vorticity is formed during the forward (backward) flow. Solid (dashed) line are used for tracing the paths taken by the vortex pairs formed during the forward (backward) flows. Vortex pairs that are successfully ejected and enter the free space above the ripple are marked by dotted green curves at some point on their pathway. Vortex pairs that fail to eject and instead dissipate by interacting with the ripple are denoted by dashed green curves near their point of eventual dissipation. The discussion will focus on two instances of the vorticity field during each of cycles 9, 12, 14, and 17. The two instances are the times at which the clockwise and counterclockwise vortices attain maximum strength, which was determined visually by counting the number of contours.

For the ninth cycle, Figure 4.36(a) identify the vorticity field at which the counterclockwise vortex attains a maximum strength and also indicate the subsequent paths taken by these vortices. Likewise, Figure 4.36(b) identify the vorticity field at which the clockwise vortex attains a maximum strength and also indicate the subsequent paths taken by these vortices. These two vortices do not pair up to form a vortex pair since they are formed at widely separated times. Instead, each of these vortices, while crossing the crest, causes the free shear layer of opposite vorticity near the ripple to roll up to form a weaker vortex with which it forms a vortex pair. During this period, the counterclockwise vortex is weak and does not generate a vortex pair, simply dissipating after traveling for a distance near the ripple. However, the clockwise vortex is strong, pairs up with a counterclockwise vortex that it generates by sourcing vorticity from the shear layer, and is then ejected in a left-upward direction into the free space above the ripple. It should be noted that also during this period, the mean current to the right is strong. Similar vortex pairs are generated and ejected in a left-upward direction during the next few periods, while the momentum of the system also decreases rapidly.
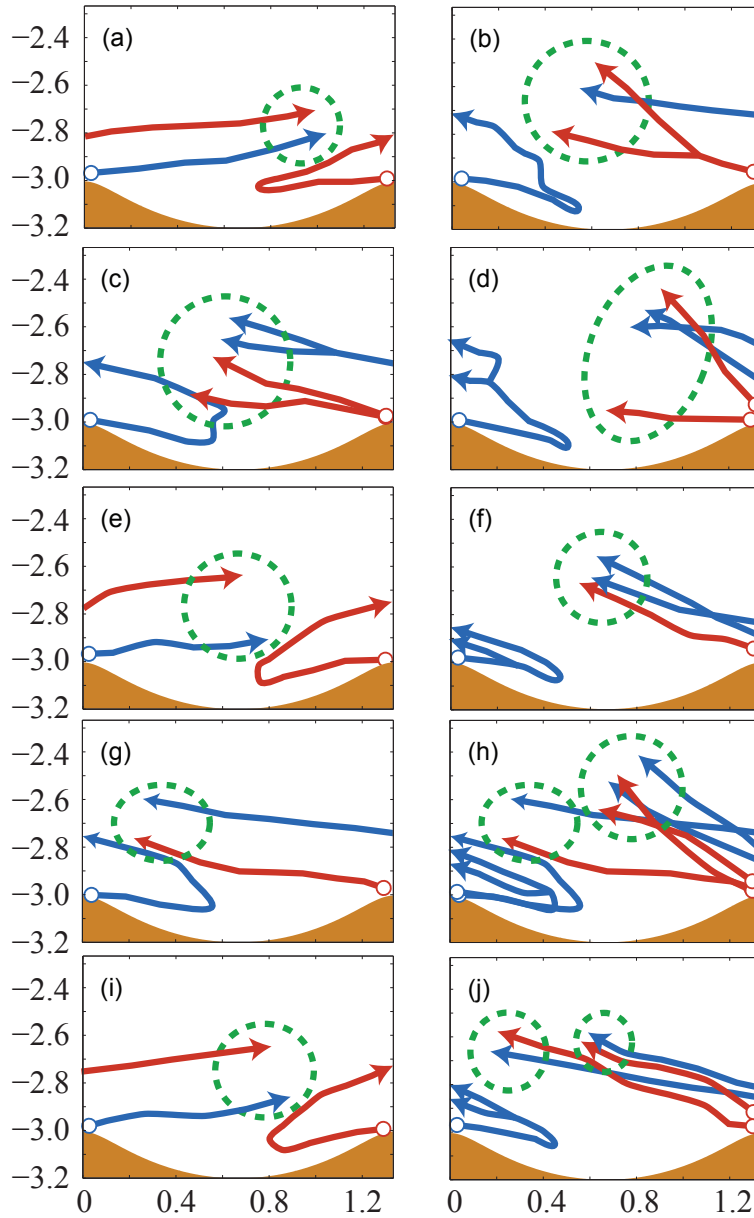
Figure 4.35: Initial trajectory of newly generated vortices during the periods listed in Table 4.3 for the R0-C1 (a,c,e,g,i) and R0-C4 (b,d,f,h,j) cases during cycles (a,b) 3 to 4, (c,d) 8 to 9, (e,f) 15 to 16, (g,h) 24 to 25, and (i,j) 29 to 30. The paths are traced using the mean vorticity field over the two periods listed. Vortex paths associated with clockwise (counterclockwise) vortices are indicated in blue (red). Curves in green indicate vortex pairs and their direction of ejection.

114

As shown in Figures 4.36(c), during the 12th cycle, the counterclockwise vortex is stronger than its corresponding counterclockwise vortex in the 9th cycle. Similarly, during the 12th cycle, Figure 4.36(d) shows that the clockwise vortex is weaker than its corresponding clockwise vortex in the 9th cycle. The vortex pair is still ejected in a left-upward direction. The momentum of the system also continues to decrease during this time, as shown in Figure 4.16(a), although at a slower pace. Figures 4.36(e,f) illustrates the same process, but at the 14th cycle. Here, the counterclockwise (clockwise) vortex has become stronger (weaker) to the extent that both the clockwise and the counterclockwise vortices are now of similar strength. At this point, no vortices are ejected into the free space. It is around this time that period-averaged momentum curve has a turning point and that mean current is strong and negative (Figure 4.16(a)). Figures 4.36(g,h) depicts the same process during the 17th periods, which occurs after the turning point of the period-averaged momentum curve. It can be observed that the counterclockwise (clockwise) vortex is now strong (weak) and that the direction of the ejection of the vortex pair changes direction to a right-upward direction. During these times, the momentum of the system increases rapidly (Figure 4.16(a)).

This process of alternate strengthening and weakening of the clockwise and the counterclockwise vortices, and the corresponding change in the direction of the vortex pair generated, takes place in step with the subharmonic oscillations observed in the period-averaged momentum curve associated with the R0-C1 case (Figure 4.16(a)). For stronger asymmetric currents, the clockwise vortex is always stronger and the vortex pairs are ejected in a left-upward direction. These observations indicate that the direction of the ejection of the vortex pair plays a major role in the creation of the mean current. During periods when the vortex pair is ejected in a left-upwards (right-upwards) direction, the momentum of the system decreases (increases).

The next consideration was to look at the momentum transferred by some of these ejected vortex pairs ejected into the free space above the ripple by measuring the momentum within the domain bounded by $z = -2.67$ and $z = -0.32$, which is a region above the ripple crest located at $z = -3.0$. For a 40-cycle duration, Figure 4.37(a) shows the momentum of the entire domain (blue) as well as that of the area bounded by $z = -2.67$ and $z = -0.32$ (red). As always, the momentum of the background forcing flow is not included. Two time periods were chosen, one in which the momentum is decreasing, 7 to 10 cycles, and the other when the momentum is increasing, 28 to 33 cycles. During these periods, the time at which the vortex pair ejected crosses the line $z = -2.67$ from below and enters the space above it was also examined. These times are given in Table 4.4 together with the direction of ejection for the vortex pairs arising from near the ripple crest. In Figures 4.37(b,c), these times are highlighted in yellow on the momentum-time curve. It
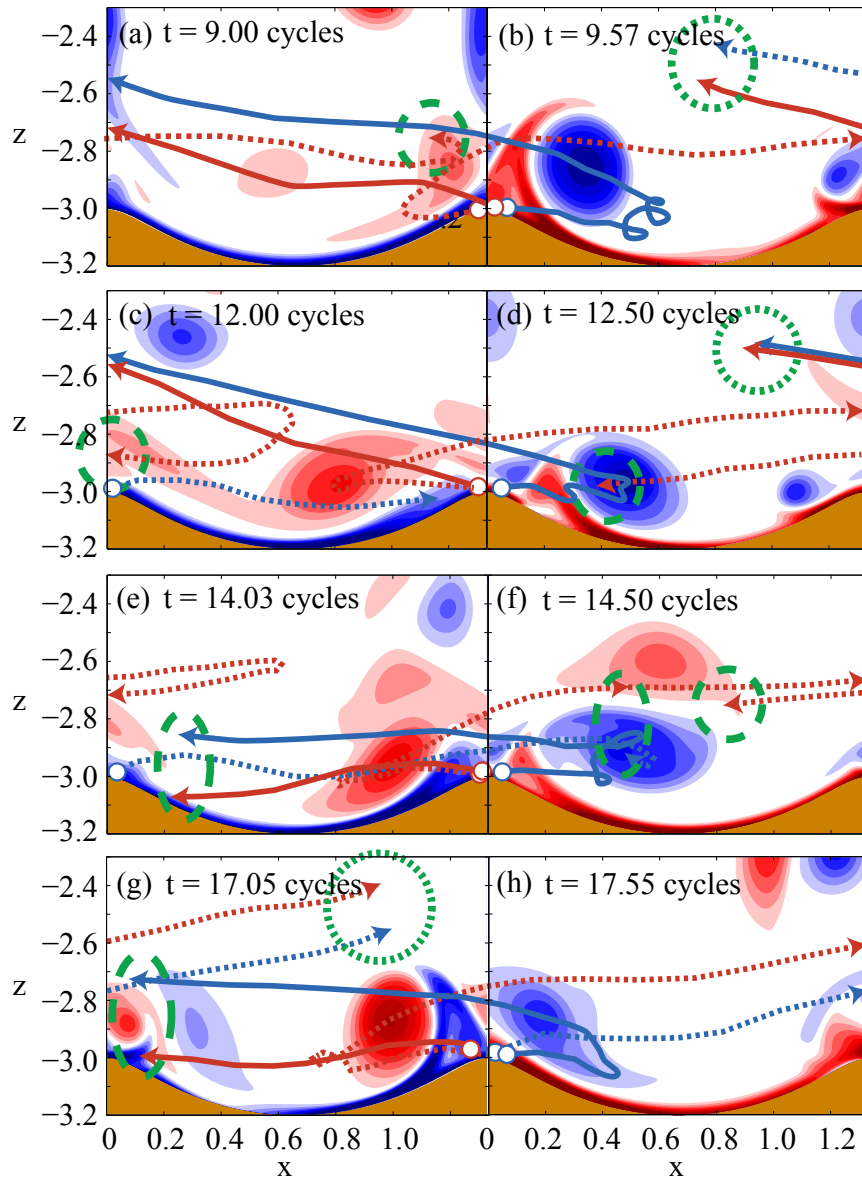
Figure 4.36: Instantaneous vorticity fields for the R0-C1 case at times (a) 9.00, (b) 9.57, (c) 12.00, (d) 12.50, (e) 14.03, (f) 14.50, (g) 17.05, (h) 17.55 cycles, along with the paths taken by the vortex pairs that are ejected into the free space during periods 9, 12, 14, and 17. Solid (dashed) paths indicate the paths associated with the vortices of the vortex pair generated at the first (second) flow reversal in each of the associated periods. Blue (red) paths indicated paths of clockwise (counterclockwise) vortices. Dotted (dashed) green curves indicate vortex pairs release (ripple-interaction).

116

Cycle	Time range (cycle)	Direction of ejection
7	7.53 to 7.97	left-upward
8	8.50 to 8.80	left-upward
9	9.47 to 9.88	left-upward
28	28.98 to 29.57	right-upward
29	29.95 to 30.35	right-upward
30	30.98 to 31.30	right-upward
32	32.00 to 32.27	right-upward

Table 4.4: Time ranges during which each newly generated vortex pair crosses the line $z = -2.67$ from below and enters the space above it together with its direction of ejection from near the ripple crest for the R0-C1 case.

can be observed that the momentum of the system above $z = -2.67$ increases (decreases) when the vortex pairs with a right-upward (left-upward) direction of ejection cross this line and that the momentum of the entire system increases (decreases) by a similar amount during those times. These findings constitute strong evidence that these vortex pairs are responsible momentum transfer and for the generation of the mean currents observed.

4.3.5   Shear stress distribution

In this section, the differences with respect to the bottom shear stress were examined. Figures 4.38 illustrates the average shear stress distribution at the quasi-steady state over the last 20 cycles. It can be observed that the bottom shear stress is almost identical to that of the x-momentum flux distribution shown in Figure 4.28. This result is to be expected since the ripples considered are not steep, and the z-momentum flux distribution indicated in Figure 4.32 is weak at most times. The R1 ripple shape tends to weaken (strengthen) the shear stress during rightward (leftward) flow, as depicted in Figure 4.38. As expected, of the three flow forcings, the most asymmetric forcing produces the strongest shear stress during the rightward flow and the weakest one during the leftward flow.
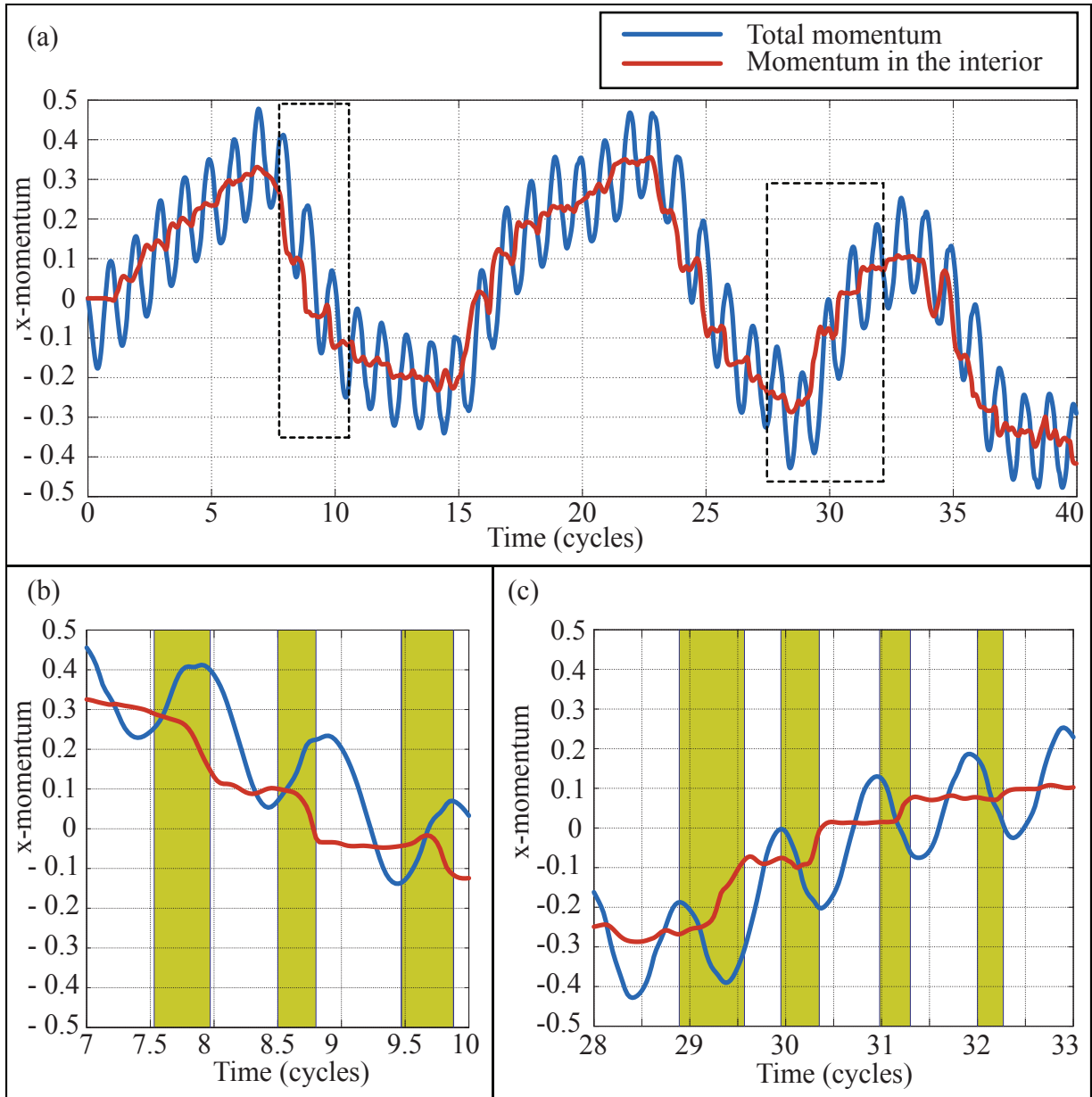
Figure 4.37: Momentum of the entire domain (blue) and within the domain bounded by $z = -2.67$ and $z = -0.32$ (red) for the R0-C1 case. Momentum is shown for the (a) first 40 cycles, (b) 7 to 10 cycles, and (c) 28 to 33 cycles.
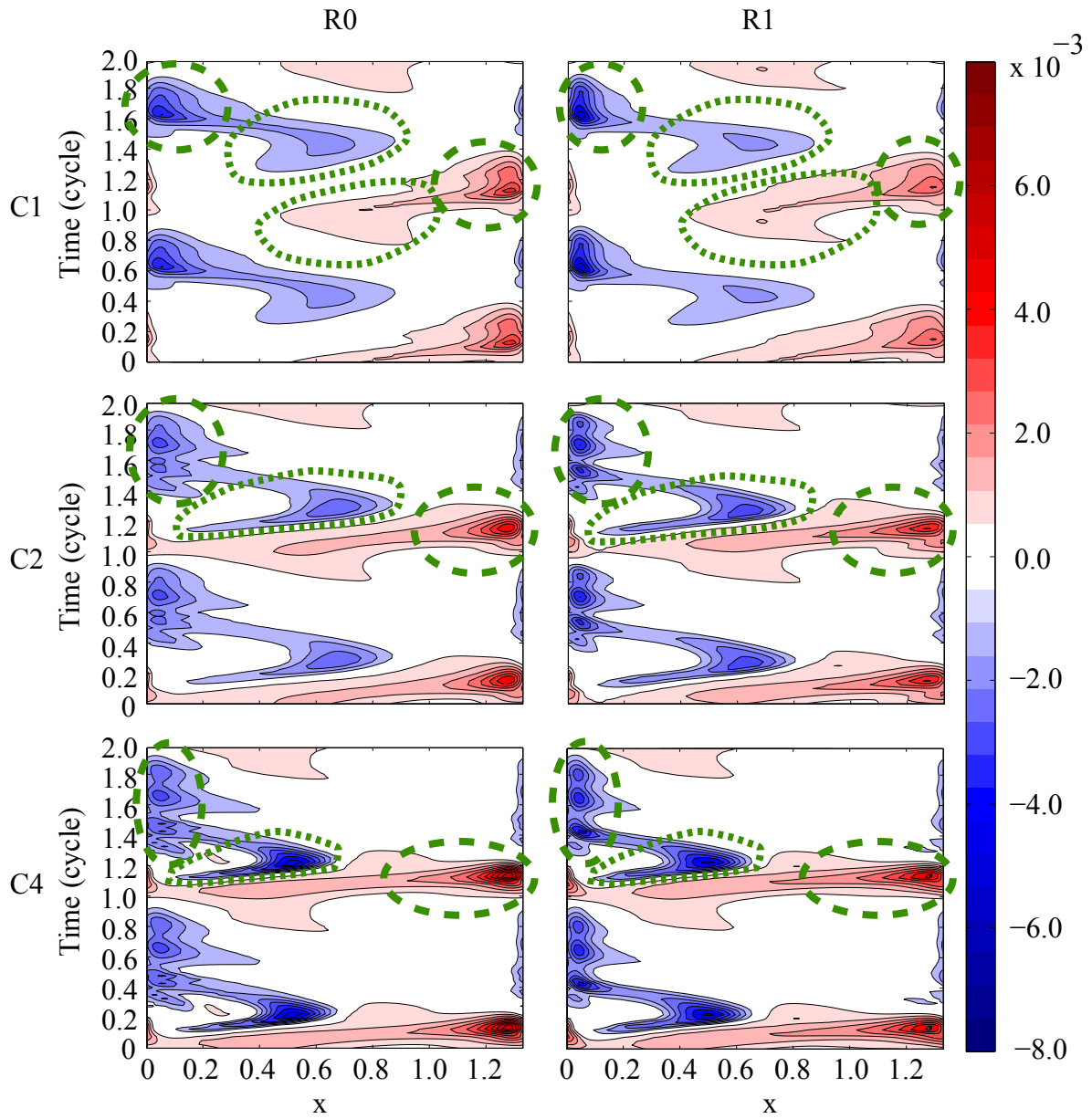
Figure 4.38: Bottom shear stress distribution for all six base cases during the first period. The two cycles shown are periodic extension of the same data.

4.4 Conclusion

This chapter has presented an examination of the vorticity and velocity fields at a quasi-steady state for the two different ripple shapes and the three flow forcings. At the quasi-steady state, it could be seen that the vortices generated at each half period of the oscillatory forcing remain close to the ripple surface, in contrast to the observations during the first three periods after initiation, as discussed in Chapter 1. For the two stronger flow forcings, the vortices exhibited greater interaction with the surface of the ripple, possibly due to the presence of a negative mean flow just above the ripple surface. The vortices formed by the two ripple shapes were largely similar.

Observations also revealed the generation of a mean current that is stronger for the asymmetric ripple and for the increasingly asymmetric flow forcing. However, long-term mean currents were similar for all cases attaining about 80% of the peak current in the oscillating flow, with the exception of the all-symmetric case. For asymmetric oscillatory flows over a flat bed, previous studies show that turbulent streaming give rise to a net current in the off-shore direction (Kranenburg *et al.* , 2012). Two separate features of the asymmetric flow, velocity and acceleration skewness, are both known to contribute to off-shore net flows. In our simulations, the mean leftward current is associated with a net negative momentum flux associated with asymmetries in the vortex shedding. The generation of a mean current due to the asymmetries in the boundaries has previously been reported for the cases involving ratchet-like oscillating boundaries (Thiria & Zhang, 2015; Yu, 2014). However, no such previous studies have been reported for non-oscillating boundaries.

The evolution of the viscous stress and pressure momentum fluxes was also examined, along with the eventual balancing of their trends with each other. The momentum contributed by the viscous stress term was interesting: larger for the asymmetric ripple and the more asymmetric the flow forcing and reversed when the ripple shape was flipped.

The final area of investigation discussed in this chapter was a detailed look at the distribution of the viscous stress field after a quasi-steady flow had been attained and how the vortex interactions at the surface of the ripple and the strong, thin, shear layers affect that distribution. Vortices impinging on the ripple surface and the strong shear layers formed on either side of the crest was found to contribute a considerable amount of momentum to the system. Vortices that do not interact with the ripple surface was found to trace the transfer of momentum from near the ripple to the region of mean flow, with the direction of ejection of vortex pairs correlating with the direction of increase or decrease of the momentum of the system.

Chapter 5

Conclusion

In this thesis, a brief overview of ripple-like structures found in nature and their formation due to fluid flows was first discussed.

Focusing on ripples formed by water flows, a description of velocity profiles under asymmetric free surface waves was given for the case of a wave-tank experiment in which ripples were formed at the bottom. For the purpose of investigating flow dynamics due to such asymmetric oscillatory flows over asymmetric ripples, velocity profiles similar to those under asymmetric free surface waves were chosen, but at a much lower Reynolds numbers, 1250 and 5000, due to computational constraints. A symmetric ripples profile was chosen resembling, in shape, those found in nature, and another slightly asymmetric ripple profile was defined.

A numerical model called SPINS was used to conduct the simulations, after verifying the validity of its outputs by comparing vortex dynamics and shear stresses with previous studies involving symmetric ripples and flows at the same Reynolds numbers. Simulations were limited to 2-dimensions.

Using these flows and ripples, simulations were conducted to investigate flow dynamics both at early stages and during the steady quasi-steady state reached after approximately 20 cycles. During the first three, it was determined that asymmetries lead to vortex pairs generated at each transition from rightward-to-leftward flow moving higher up into the water column.

During the quasi-steady state, it was determined that asymmetries lead to negative mean flows which strengthen as asymmetries increase in both the ripple and the oscillating flow. The mean flow for the symmetric current and asymmetric ripple is toward the steep

face. For the asymmetric flows, it is in the opposite direction to that of the strongest flow. Further, there was a correlation between the direction of this mean current and the direction of the ejection of vortex pairs from the ripple, and the generation of mean currents was attributed to damping of vortices.

5.1 Future work

There are many geometric properties used to characterize a ripple profile: ripple length, height, and asymmetry (Wiberg & Harris, 1994). For orbital ripples (ratio of wave orbital diameter to mean grain diameter < 2000), the ripple length is determined by the excursion length of the flow and $0.59 \leq s/l \leq 0.75$, approximately (O'Donoghue & Clubb, 2001; Traykovski *et al.* , 1999). In this thesis, parameters were chosen in the orbital ripple range ($s/l = 0.75$) and all except the ripple asymmetry was kept constant. It would be interesting to know the effect of slight changes in ripple height (hence, changes to h/l) on flow dynamics, both in the early stages and at the quasi-steady state. Results by Kim *et al.* (1994) indicate that changes to flow dynamics will be relatively large due to changes in ripple steepness than to changes in ripple asymmetry in the first cycle. This may result in considerable changes to the flow during the quasi-steady state.

During the quasi-steady state, a mean current was observed which strengthened as asymmetries increased. Although it was shown that organized damping of vortices played a major role in creating this mean current, the theoretical reasons that lead to this phenomenon was not determined. Previous studies have shown that progressive waves over rough bottoms induce currents as a result of organized vortex shedding (Davies & Villaret, 1999). Furthermore, considering our results and previous theoretical (Kranenburg *et al.* , 2012) and numerical (Scandura *et al.* , 2016) work , velocity and acceleration skewness (asymmetries) of the flow and asymmetries in the ripple profile results in these mean currents. However, further investigations are needed to quantify how the mean currents depend on the velocity and acceleration skewness of the flow.

Due to computational constraints, simulations in this thesis were limited to the low Reynolds numbers 1250 and 5000. Real world flows have much larger Reynolds numbers. Although current computational constraints prevents the investigation of much higher Reynolds number flows using DNS, useful flow statistics can be obtained by conducting simulations using less computationally expensive methods like those using turbulence closure models. Conducting such higher Reynolds number flows will give important information regarding mean currents at the quasi-steady state that are applicable to real-world flows.

Finally, simulations in this thesis were limited to 2-dimensional flows. Investigation of 3-dimensional flows in similar settings will be limited to a few oscillatory cycles due to computational constraints. Flow dynamics in 2-dimensions can be considerably different to those in 3-dimensions. This will again give insight into flow behaviours applicable to real-world flows.

References

Admiraal, D., Musalem-Jara, R., Garca, M., & Nio, Y. 2006. Vortex trajectory hysteresis above self-formed vortex ripples. *Journal of Hydraulic Research*, **44**(4), 437–450.

Angelis, V. De, Lombardi, P., & Banerjee, S. 1997. Direct numerical simulation of turbulent flow over a wavy wall. *Physics of Fluids*, **9**(2429).

Barr, B.C., Slinn, D.N., Thomas, P., & Winters, K.B. 2004. Numerical simulation of turbulent, oscillatory flow over sand ripples. *Journal of Geophysical Research*, **109**(C9).

Blondeaux, P., & Vittori, G. 1991. Vorticity dynamics in an oscillatory flow over a rippled bed. *Journal of Fluid Mechanics*, **226**, 257–289.

Blondeaux, P., Scandura, P., & Vittori, G. 2004. Coherent structures in an oscillatory separated flow: numerical experiments. *Journal of Fluid Mechanics*, **518**, 215–229.

Chang, K., & Constantinescu, G. 2013. Coherent structures in flow over two-dimensional dunes. *Water Resources Research*, **49**, 2446–2460.

Cherukat, P., Na, Y., Hanratty, T.J., & McLaughlin, J.B. 1998. Direct Numerical Simulation of a Fully Developed Turbulent Flow over a Wavy Wall. *Theoretical and Computational Fluid Dynamics*, **11**(2), 109–134.

Davies, A. G., & Villaret, C. 1999. Eulerian drift induced by progressive waves above rippled and very rough beds. *Journal of Geophysical Research*, **104**, 1465–1488.

Doucette, J. S., & O'Donoghue, T. 2006. Response of sand ripples to change in oscillatory flow. *Sedimentology*, **53**, 581–596.

Dumas, S., Arnott, R.W.C., & Southard, J.B. 2005. Experiments on oscillatory-flow and combined-flow bed forms: implications for interpreting parts of the shallow-marine sedimentary record. *Journal of Sedimentary Research*, **75**(3), 501–513.

Grigoriadis, D. G. E., Dimas, A. A., & Balaras, E. 2012. Large-eddy simulation of wave turbulent boundary layer over rippled bed. *Coastal Engineering*, **60**, 174–189.

Hay, A. E., Zedel, L., Cheel, R., & Dillon, J. 2012. Observations of the vertical structure of turbulent oscillatory boundary layers above fixed roughness beds using a prototype wideband coherent Doppler profiler: 1. The oscillatory component of the flow. *Journal of Geophysical Research*, **117**(C03005).

Kim, H., O'Connor, B.A., & Shim, Y. 1994. Numerical Modelling of flow over ripples using SOLA method. *Pages 2140–2154 of: Coastal Enginnering Proceedings.*

Kranenburg, W.M., Ribberink, J.S., Uttenbogaard, R.E., & Hulscher, S.J.M.H. 2012. Net currents in the wave bottom boundary layer: On waveshape streaming and progressive wave streaming. *Journal of Geophysical Research*, **117**(F03005).

Longuet-Higgins, S. 1981. Oscillating flow over steep sand ripples. *Journal of Fluid Mechanics*, **107**, 1–35.

Malarkey, J., & Davies, A. G. 2012. Free-stream velocity descriptions under waves with skewness and asymmetry. *Coastal Engineering*, **68**, 79–95.

Nielsen, P. 1981. Dynamics and Geometry of Wave-Generated Ripples. *Journal of Geophysical Research*, **86**(C7), 6467–6472.

O'Donoghue, T., & Clubb, G. S. 2001. Sand ripples generated by regular oscillatory flow. *Coastal Engineering*, **44**(December).

Scandura, P., Vittori, G., & Blondeaux, P. 2000. Three-dimensional oscillatory flow over steep ripples. *Journal of Fluid Mechanics*, **412**, 355–378.

Scandura, P., Faraci, C., & Foti, E. 2016. A numerical investigation of acceleration-skewed oscillatory flows. *Journal of Fluid Mechanics*, **808**, 576–613.

Sekiguchi, T., & Yokokawa, M. 2008. Effect of wave period on combined-flow beforms: a flume experiment. *Pages 281–284 of: Marine and River Dune Dynamics.*

Subich, C. J., Lamb, K. G., & Stastna, M. 2003. Simulation of the Navier-Stokes equations in three dimensions with a spectral collocation method. *International Journal for Numerical Methods in Fluids*, **73**, 103–129.

Svendsen, I. A. 1990. *Introduction to nearshore hydrodynamics. Advanced series on ocean engineering.* Vol. 24. World Scientific.

Testik, F. Y., Voropayev, S. I., Balasubramanian, S., & Fernando, J. S. 2006. Self-similarity of asymmetric sand-ripple profiles formed under nonlinear shoaling waves. *Physics of Fluids*, **18**(108101).

Thais, L., & Magnaudet, J. 1995. A triple decomposition of the fluctuating motion below laboratory wind water waves. *Journal of Geophysical Research*, **100**(C1), 741–755.

Thiria, B., & Zhang, J. 2015. Ratcheting fluid with geometric anisotropy. *Applied Physics Letters*, **106**(054106).

Traykovski, P., Hay, A. E., Irish, J. D., & Lynch, J. F. 1999. Geometry, migration, and evolution of wave orbital ripples at LEO-15. *Journal of Geophysical Research*, **104**(January).

Wiberg, P. L., & Harris, C. K. 1994. Ripple geometry in wave-dominated environments. *Journal of Geophysical Research*, **99**(C1), 775–789.

Yu, J. 2014. Fluid ratcheting by oscillating channel walls with sawteeth. *Journal of Fluid Mechanics*, **761**, 305–328.

APPENDICES

Appendix A

Obtaining a uniform x-grid for SPINS

The ripple shapes are parametrically defined using (A.1)-(A.2)

$$x\left(\xi\right) = \xi - \frac{h}{2}\sin\left(k\xi\right) - \frac{\epsilon}{2}\left[1 - \cos\left(k\xi\right)\right], \tag{A.1}$$

$$z\left(\xi\right) = \frac{h}{2}\left[1 + \cos\left(k\xi\right)\right] - H, \tag{A.2}$$

where $k = \frac{2\pi}{l}$ $\xi \in [0, l]$ is a dummy parameter and ϵ is the parameter used to control the asymmetry of the ripple shape. The ripple shapes R0 and R1 are defined using the choices $\epsilon = 0.0$ and 0.1, respectively. R0 is the symmetric ripple matching the shape used by Blondeaux et al. (1991, 2004). For the ripple shapes defined by (3.6)-(3.7), the quantity of the fluid (area) above the ripple is independent of the ripple shape:

$$\int_0^1 z\left(\xi\right) x'\left(\xi\right) d\xi = -Hl - \frac{\pi h^2}{4} + \frac{hl}{2}$$

Expressions (A.1)-(A.2) can be used directly in SPINS but that results in a non-uniform grid distribution in the x-direction. For ripple shapes with $\frac{h}{l}$ and ϵ sufficiently small, we can use a simple iterative scheme to generate a uniform grid. To obtain a uniform x-grid distribution, say $x_0, x_1, x_2, \ldots, x_{N-1}$, set

$$x_i = \xi_i - \frac{h}{2}\sin\left(k\xi_i\right) - \frac{\epsilon}{2}\left(1 - \cos(k\xi_i)\right) \tag{A.3}$$

128

and determine ξ_i using an iterative scheme. Rearranging (A.3),

$$\xi_i \;=\; \underbrace{x_i + \frac{h}{2}\sin(k\xi_i) + \frac{\epsilon}{2}(1 - \cos(k\xi_i))}_{f(\xi_i,x_i)} \;\Rightarrow\; \xi_i = f(\xi_i, x_i)$$

For a given x_i, we iterate $\xi_i^{n+1} = f(\xi_i^n, x_i)$ with some suitable starting point ξ_i^0 until $\left|\xi_i^{n+1} - \xi_i^n\right| < \epsilon_i$ for some sufficiently small threshold $\epsilon_i > 0$, which is set to 10^{-15} for double precision. For the ripples sizes we consider, this iteration is found to be convergent.

$$
\begin{aligned}
\left|f\left(\xi_i^{n+1}, x_i\right) - f\left(\xi_i^n, x_i\right)\right| &\leq \frac{h}{2}\left|\sin(k\xi_i^{n+1}) - \sin(k\xi_i^n)\right| + \frac{\epsilon}{2}\left|\cos(k\xi_i^{n+1}) - \cos(k\xi_i^n)\right| \\
&\leq \frac{\pi h}{l}\left|\xi_i^{n+1} - \xi_i^n\right| + \pi\epsilon\left|\xi_i^{n+1} - \xi_i^n\right| \\
&= \pi\left(\frac{h}{l} + \frac{\epsilon}{l}\right)\left|\xi_i^{n+1} - \xi_i^n\right| \\
&< \left|\xi_i^{n+1} - \xi_i^n\right| \text{ if } \pi\left(\frac{h}{l} + \frac{\epsilon}{l}\right) < 1
\end{aligned}
$$

In our simulations, we have $\pi\left(\frac{h}{l} + \frac{\epsilon}{l}\right) = \pi\left(0.15 + 0.1/1.33\right) < 1$.

Appendix B

Bottom shear stress (uniform x-grids)

The bottom ripple is defined by $z = F(x)$, where x and z are defined parametrically by (2.15)-(2.16). By the use of an iterative scheme, as described in Appendix A, we find

$$\left\{ (\eta, \xi) \,\middle|\, \eta = \xi - \frac{h}{2} \sin(k\xi), \eta \in (0, l) \right\}. \tag{B.1}$$

Now $(\eta, z(\xi))$ defines the ripple surface. If the relation (B.1) is a 1-1 function on $(0, l)$, then we can choose an alternative representation

$$(\eta, z(\xi)) \equiv (\eta, z(\xi(\eta))) \equiv (\eta, z(\eta)), \quad \eta \in (0, l) \tag{B.2}$$

The tangential vector to the ripple surface

$$\boldsymbol{t} = \left(1, \frac{dz}{d\xi}\frac{d\xi}{d\eta}\right) = \left(1, \frac{-\frac{hk}{2}\sin(k\xi)}{1-\frac{hk}{2}\cos(k\xi)}\right),$$

since $\frac{dz}{d\eta} = -\frac{hk}{2}\sin(k\xi)$, $\frac{d\eta}{d\eta} = \frac{d\xi}{d\eta} - \frac{kh}{2}\cos(k\xi)\frac{d\xi}{d\eta}$, and $\frac{d\xi}{d\eta} = \frac{1}{1-\frac{hk}{2}\cos(k\xi)}$. In discrete form, we set $\xi = \xi_i = \frac{l}{N_x}\left(i + \frac{1}{2}\right)$, where $i \in \{0, 1, 2, ..., N_x - 1\}$. As before, $\boldsymbol{u} \cdot \boldsymbol{t}$ is calculated, and $\boldsymbol{\nabla}(\boldsymbol{u} \cdot \boldsymbol{t})$ is found using the grad2c.m routine provided with SPINS.